# AN INVESTIGATION OF Sb–Se–Ge AND Sb–Se–Ge–In GLASSY ALLOYS FOR PHYSICAL, STRUCTURAL, THERMAL AND OPTICAL PROPERTIES

THESIS SUBMITTED IN FULFILLMENT OF THE REQUIREMENTS
FOR THE DEGREE OF

**DOCTOR OF PHILOSOPHY**

IN

**PHYSICS**

BY

**SUNANDA**

[ENROLLMENT NUMBER 096903]

DEPARTMENT OF PHYSICS AND MATERIALS SCIENCE
JAYPEE UNIVERSITY OF INFORMATION TECHNOLOGY
WAKNAGHAT, SOLAN (H.P) – 173234
INDIA

JULY 2013

# CERTIFICATE

This is to certify that the thesis entitled, "**An Investigation of Sb-Se-Ge and Sb-Se-Ge-In Glassy Alloys for Physical, Structural, Thermal and Optical Properties**" which is being submitted by ***Miss Sunanda*** for the award of degree of **Doctor of Philosophy** in **Physics** by the **Jaypee University of Information Technology** at Waknaghat, is the record of candidate's own work carried out by her under our supervision. This work has not been submitted partially or wholly to any other University or Institute for the award of this or any other degree or diploma.

Date: July 18, 2013

**Dr. Vineet Sharma**
Supervisor–I
**Email:** vineet.sharma@juit.ac.in
**Phone**: +91 94182 33083

**Dr. Pankaj Sharma**
Supervisor–II
**Email:** pankaj.sharma@juit.ac.in
**Phone**: +91 94189 52533

# Acknowledgements

During the course of my research work a lot of people helped and supported me. Therefore, I would like to take the opportunity to acknowledge them.

First and foremost, I am grateful to my supervisors **Dr. Vineet Sharma** and **Dr. Pankaj Sharma** for their guidance and support during my Ph. D. Without their continuous motivation and encouragement it would have been harder to complete my research work.

I express my deepest gratitude to **Prof. (Dr.) Yajulu Medury (COO, JES)**, **Brig. (Retd.) Balbir Singh (Director, JUIT)** and **Prof. T.S. Lamba (Dean A&R)** for providing me financial support and assistance in all forms during the research work.

My sincere thanks to **Prof. (Dr.) P.B. Barman**, Head, Department of Physics & Materials Science, Jaypee University of Information Technology, Waknaghat, Prof. (Dr.) Sunil K. Khah, Dr. Dheeraj Sharma, Dr. Rajesh Kumar, Dr. Surajit Hazra, Dr. Ragini Raj Singh and Dr. Sanjeev Tiwari for their advice and assistance at all levels of my research.

My thanks are also due to my friends Abhishek Kandwal, Neha Sharma, Mr. Suresh Kumar, Pawan Kumar, Hitanshu Kumar and Dikshita Gupta for their valuable contribution. Special thanks to **Neha Sharma** for discussing doubtful topics with me by sparing her own research time.

My deepest thanks to my family: **my mother**, **father** and **younger sister**, for their understanding, patience and uninterrupted love during the course of work. I would also acknowledge Dr. Swati Aerry for extending her help and good wishes in every phase of my work.

Finally, I thank almighty **GOD** for giving me strength and ability to perform this work. Without HIS grace and blessings I would not have been able to complete this work.

**Date:** **(*Sunanda*)**

# Contents

# List of Tables

# List of Figures

# CHAPTER 1

# Introduction

Materials science is an applied science concerned with the relationship between structure and properties of the materials. It involves examining how the microstructure of a material whether crystalline or amorphous, can be varied to influence the properties of a material. This helps in changing or enhancing inherent properties to create and improve the end products suited for use to society. Properties are divided into different categories including mechanical, electrical, thermal, magnetic, optical etc. Materials fall into one of the following classifications established by their composition and structure: metals, ceramics, polymers, composites, semiconductors, biomaterials, and nanomaterials, etc.

Matter exists in three common states of matter *i.e.* solid, liquid and gas. There is a fourth state known as plasma, ionized gas, found mostly inside stars. Solids are a particular state of condensed matter characterized by strong interactions between the constituent particles (atoms, molecules). Solids exist in either ordered (crystalline) or disordered (non–crystalline, amorphous or vitreous) state.

In the crystalline state constituent atoms or molecules are dispersed in a lattice structure having translational symmetry and can be arranged in definite structural forms. Crystalline solids can be classified into six types *viz.* metallic, ionic, network covalent, molecular non–polar, polar and hydrogen bonded. The real crystal differs from the ideal crystalline structure in terms of imperfections and defects in it. On the other hand, in non–crystalline state the constituents are not dispersed periodically *i.e.* their structural arrangement is not well defined. So, it is difficult to define a parameter that characterizes the degree of crystallinity or non–crystallinity of a solid because the possible order–disorder transitions are not unique. A typical feature of these substances is that upon heating, their viscosity drops. They gradually become soft and begin to behave like ordinary viscous liquids. Amorphous materials present a challenge and opportunity to researchers to cultivate their technological applications, since there are immense physical processes unique to these systems. These can be achieved through materials optimization and basic understanding.

## 1.1 Glasses

Liquid when cooled down either discontinuously solidifies to a crystalline *i.e.*, topologically ordered phase or goes through a continuous phase transition and solidifies to a metastable disordered solid generally called amorphous phase. The liquid–crystal transition can be identified as the discontinuous drop in the volume of the system at a critical temperature with sufficiently slow quench rate. Fast quenching of the liquid mostly results in a continuous decrease in the volume when the temperature passes a threshold known as the glass transition temperature ($T_g$). The disordered solids obtained through a glass transition are generally categorized as glasses. Glasses can be categorized in two groups: tetrahedraly coordinated silicon like materials and chalcogenide glasses.

### 1.1.1 Tetrahedral glasses

Tetrahedraly bonded glasses constitute fourth group amorphous semiconductors, silicon ($Si$) and germanium ($Ge$). In pure form, amorphous (a–) $Si$ and a–$Ge$ are formed by sputtering or thermal evaporation. Amorphous $Si$ and $Ge$ are formed by tetrahedral units, where most of the atoms have four bonds and the average bond angle is 109.5$^o$. Similar is the case with hydrogenated $Si$ (a–$Si$:$H$) where hydrogen forms one bond. The a–$Si$:$H$ and its alloys have applications in large area electronic devices such as solar cells and displays.

### 1.1.2 Chalcogenide glasses

The word *chalcogen* refers to the group 16 elements $S$, $Se$ and $Te$. *Chalcogenide glasses* are based upon these elements in binary or multicomponent systems. The four fold coordination of $Si$ leads to the formation of highly symmetrical and rigid structures. On the other hand, two fold chalcogen leads to the formation of asymmetrical and flexible structures. Thus, the structure of chalcogenides is more complex than that of tetrahedraly bonded a–$Si$ or a–$Ge$. Chalcogenides consist of chain or layer like structures leading to the absence of long range order. In general, chalcogenides are good glass formers and can be prepared by both cooling from liquid and vapor deposition. The most studied chalcogenides are a–$Se$, $As_2Se_3$, $GeSe_2$.

Chalcogenides are well known to form non–oxide glasses which have predominantly covalent bonding structures with maximum ionic conductivity of 9 %. Their properties vary significantly from that of oxide glasses. The thermal expansion coefficient, the temperature coefficient of the refractive index and relative photoelastic coefficient are much higher than oxide glasses [1]. Earlier most of the studies were carried out on silicate and quartz glasses which can transmit radiation in visible region of spectrum. But, interest aroused in chalcogenide glasses as these find use in various technological applications due to their higher transparency, higher linear and non linear refractive indices, lower phonon energies etc.

Chalcogenides have lone pair and show semiconducting properties. Therefore, chalcogenides are also called lone–pair–semiconductors. The presence of lone pairs increase the flexibility of the bond angles which decreases the strain energy in the system. This causes the atoms to readily form amorphous structures either alone or with other constituent elements. These may be elemental like $S$, $Se$; binary $As_2S_3$, $As_2Se_3$ or in multicomponent forms as $Ga_5Sb_5Ge_{25}Se_{65}$, $Sr_3GeSb_2Se_8$. Elemental or binary chalcogenides have chain like or layered structures extending in one or two dimensions. The extent of short order is large in these glasses. On the other hand, multicomponent systems attain rigidity and a three dimensional structure and thus, have lower extent of short range order.

## 1.2 History of chalcogenide glasses

The amorphous materials are known since the Egyptian age for their use as glass beads. Man has been using glass in the form of silicates from thousands of years. But, the earliest experimental data on oxygen free glass have been published by Schulz – Sellack in 1870 [2]. Later on, Wood in 1902 [3], as well as Meir in 1910 [4] carried out the first researches on the optical properties of vitreous selenium. Zachariasen [5] considered the principles on how bonding requirements were met and nearest neighbor coordination maintained without imposing an exact long range order common for crystalline materials. These glasses were investigated as optoelectronic materials in infrared systems by R. Frerichs with the rediscovery of arsenic trisulfide glass in his work [6]. The earliest reference to “vitreous semiconductors” was made by Goriunova and Kolomeits in 1955 [7]. They discovered that amorphous chalcogenides are semiconductors and that the alloy $TlAsSe_2$ instead of having a crystalline structure had many properties of a typical glass. Glaze and co–workers [8] developed in 1957, the first method for the preparation of the glass at industrial scale. In 1960, Ioffe and Regel [9] realized that the bandgap depends on the existence of short range order rather than on the long range order of the lattice and suggested that the first coordination number of corresponding crystal is preserved in amorphous structure. The glass forming region for the *Si–As–Te* system was planned by Hilton and Brau [10]. This development led to an exploratory DARPA–ONR program from 1962 to 1965. The ultimate goal of the program was to find infrared transmitting chalcogenide glasses with physical properties comparable to those of oxide optical glasses and a softening point of 500 $^{o}$C. In 1967, Harold Hafner [11] made many important contributions including a glass casting process and a glass tempering process in Semiconductor Production Division under the direction of Charlie Jones. There work was concentrated on *Ge–As–Se* system [11].

In 1968, Ovshinsky [12] reported reversible phase transformation in chalcogenides, responsible for electrical switching. He produced a switching device made from an amorphous thin film of tantalum oxide, deposited on a tantalum substrate, forming one electrode while a liquid electrolyte formed a second electrode. This switch required maintaining a voltage to keep it in the high conductance state. This discovery led to the fabrication of memory devices. In early 1970's, sensitivity of chalcogenides to light was recognized and was applied to xerography [13].

Applications of solar cells were developed by Ciureanu and Middehoek [14] and Robert and his coworkers [15]. Infrared optics applications were studied by Quiroga and Leng and their coworkers [16]. The switching device applications were introduced by Ovshinsky [12] and Bicerono and Ovshinsky [17]. P. Boolchand and his coworkers [18] discovered intermediate phase in chalcogenide glasses. Several investigators have also reported useful optoelectronics applications in infrared transmission [19, 20] and detection [21, 22] threshold and memory switching [23, 24], optical fibers [25, 26], functional elements in integrated–optic circuits [27], non–linear optics [28, 29], holographic & memory storage media [30], chemical and bio–sensors [31, 32], infrared photovoltaics [33], microsphere laser [34], active plasmonics [35], microlenses in inkjet printing [36] and other photonics [37, 38] applications.

Subsequently, several review books were published on chalcogenide glasses e.g. "The Chemistry of Glasses" by A Paul in 1982, "The Physics of Amorphous Solids" by R. Zallen in 1983 and "Physics of Amorphous Materials" by S.R. Elliott in

1983. However, first book entirely dedicated to chalcogenide glassy materials entitled “Chalcogenide Semiconducting Glasses” was published in 1983 by Z.U. Borisova. In this order, G.Z. Vinogradova published her monograph “Glass formation and Phase Equilibrium in Chalcogenide Systems” in 1984. M.A. Andriesh dedicated a book to some specific applications of chalcogenide glasses entitled “Glassy Semiconductors in Photo–electric Systems for Optical Recording of Information”. M.A. Popescu gave large and detailed account on physical and technological aspect of chalcogenide systems in his book “Non–Crystalline Chalcogenides”. The compendium of monographs on the subject of photo–induced processes in chalcogenide glasses entitled “Photo–induced Metastability in Amorphous Semiconductors” was compiled by A.V. Kolobov–2003. In 2003 Jai Singh and Koichi Shimakawa presented recent advances made in the field of amorphous semiconductors in their book “Advances in Amorphous Semiconductors”. Robert Fairman and Boris Ushkov–2004 described physical properties in “Semiconducting Chalcogenide Glass I: Glass formation, structure, and simulated transformations in Chalcogenide Glass”. A. Zakery and S.R. Elliott described optical characteristics in the book “Optical Nonlinearities in Chalcogenide Glasses and their Applications” in 2007. K. Tanaka and K. Shimakawa have described developments in the science and technology of this class of materials in their book “Amorphous chalcogenide semiconductors and related materials”.

## 1.3 Band models for amorphous materials

In crystalline (c–) solids, sharp edges in density of states produce well defined forbidden band gap. This is due to perfect short range and long range order in c–solids. The a–solids have short range order. This short range order resembles with the crystalline one which implies that the concept of density of states is also applicable to a–solids. Weaire and Thorpe [39] proposed that the existence of band gap holds for a–solids, without considering the periodicity of the network. Mott first generalized the concepts of crystalline semiconductors to amorphous ones based on Anderson’s theory [40]. According to Mott, the spatial fluctuations in the potential caused by the configurational disorder in amorphous materials may lead to the formation of localized states, which do not occupy all the different energies in the band, but form a tail above and below the normal band. He further postulated that there should be sharp boundary between the energy ranges of extended and localized states. These states are said to be localized in the sense that an electron placed in a region will not diffuse at zero temperature to other regions with corresponding potential fluctuation. There exist critical energies in each band where a sharp jump in mobility from negligible values to finite ones takes place at particular density of electronic states above which the states in amorphous solid become extended. These critical energies are called the mobility edges. The energy difference between the mobility edges of the valence band ($E_v$) and that of conduction band ($E_c$) is called the mobility gap. Many models have been proposed for the band structure of a–semiconductors. The main features of these models have been discussed below.

### 1.3.1 Cohen Fritzsche Ovshinsky model

The Cohen Fritzsche Ovshinsky (CFO) model [41] assumed that the tail states extend across the gap in a structureless distribution. The distribution of density of states ($N(E)$) for CFO model has been shown in Figure 1.1.

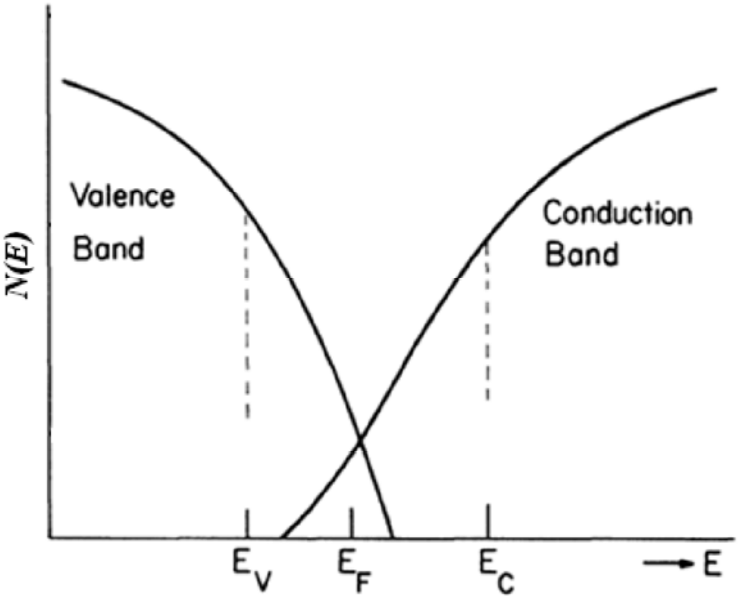

**Figure 1.1** Density of states for Cohen–Fritzsche–Ovshinsky model.

They suggested that apart from the mobility edges, there are tails of the localized stated pulled out of the conduction and valence bands by disorder and there is some overlap between these tails. Equal numbers of positive and negative charge states are produced where the tail states overlap. The overlapping bands that give rise to a finite value of $N(E)$ are due to defects of acceptor and donor type. A consequence of the band overlapping is that there are normally filled valence band states that have energies higher than empty conduction band states resulting in redistribution to restore equilibrium. In the redistribution of electrons, filled states are formed in the conduction band tails which are negatively charged and empty states are formed in the valence bands which are positively charged. This pins the Fermi level ($E_F$) close to the middle of the gap, a feature required for electrical properties of these materials. The CFO model was specially proposed for multicomponent chalcogenide glasses used in switching devices. One of the major objections against CFO model is the transparency of a–chalcogenides below a well defined absorption edge leading to the conclusion that the extent of tailing is only few tenths of an electron volt in the gap [42]. Another objection to this model is that the elemental semiconductors like a–*Si*, a–*Ge*, a–*As* etc. should not have the extensive band tailing as they are free from compositional disorder [43].

### 1.3.2 Davis–Mott model

According to Davis–Mott model [44] the tails of the localized states are narrow and extend to a few tenths of an electron volt into the forbidden energy gap. The Davis–Mott band model has been shown in Figure 1.2. They proposed a band of compensated levels, originating from defects in the random network e.g. dangling bonds, vacancies etc., near the gap centre which pins the Fermi level and account for the behavior of a.c. conductivity. The band may be split into donor ($E_B$) and acceptor bands ($E_A$). Mott suggested that in making a transition from extended to localized states the mobility decreases by several orders of magnitude and a mobility edge is produced. Indeed, the concept of localized states implies that the mobility is zero at temperature ($T$) = 0K. The interval between $E_c$ and $E_v$ is defined as the mobility gap. On the other hand Cohen [42] suggested that there should be a continuous drop in the mobility, instead of an abrupt drop, occurring in the extended states just inside the mobility edge. He described the transport as Brownian motion in which carriers are under the influence of a continuous scattering. The interpretation of electrical transport is closely related to the energy distribution of the density of states.

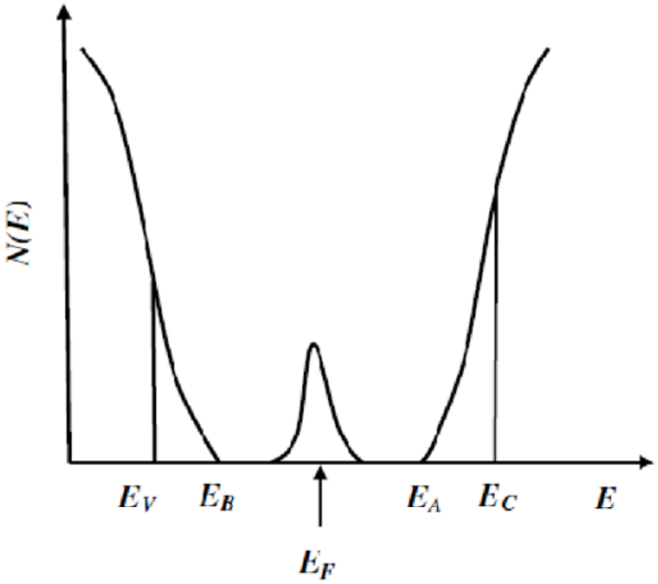

**Figure 1.2** Density of states for Davis–Mott model.

According to Davis–Mott model there are three processes responsible for conduction in amorphous semiconductors and their contribution to the total conductivity will predominate in different temperature regimes. At very low temperatures, conduction occurs by thermally assisted tunneling between states at the Fermi level. At higher temperatures, charge carriers are excited into the localized states of band tails where they can take part in the electric charge transport only by hopping. At still higher temperatures, carriers get excited across the mobility edge into the extended states. Therefore, the electrical conductivity measurements over a wide range of temperature give an idea of the electronic structure of the amorphous semiconductors.

### 1.3.3 Marshall–Owen model

A first proposal of a model showing gap was introduced by Marshall and Owen in 1971, and therefore called the Marshall–Owen model [45]. Marshall–Owen model (shown in Figure 1.3) suggested that the position of Fermi level is determined by the well separated bands of donors and acceptors in the upper and lower halves of the mobility gap respectively. Self compensation of concentration of donors ($E_B$) and acceptors ($E_A$) takes place in such a way that the Fermi level remains near the gap centre. At low temperature, Fermi level moves to one of the impurity bands as self compensation is not likely to be complete. This model is mainly based on the observation that the high field drift mobility of $As_2Se_3$ is of Poole Frenkel type probably because of the field–simulated emission of carriers from the charged trapping centers (acceptors).

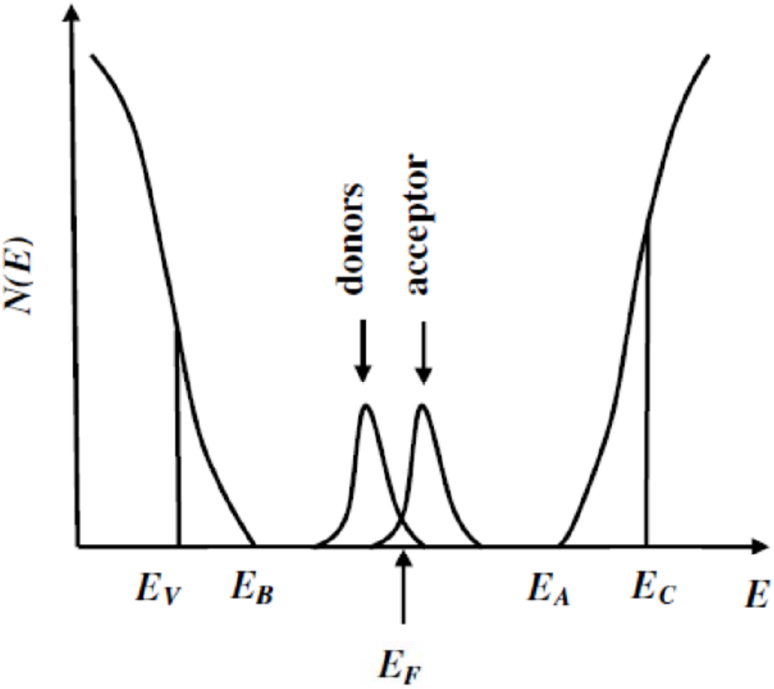

**Figure 1.3** Density of states for Marshall–Owen model.

### 1.3.4 Small polaron model

The role of distortion in the presence of an extra charge carrier in an amorphous solid has been discussed in detail by Emin [46]. He suggested that if an atom is held fixed in the solid then it acts as a perturbation to its immediate environment causing a displacement of atoms in its vicinity thereby decreasing the total energy of the system. The equilibrium positions assumed by these atoms produce a potential well for the carrier. If the potential well associated with the local lattice distortion is sufficiently deep then the carrier will occupy a bound state, being unable to move without an alteration of the positions of the neighboring atoms. This is referred to as "self–trapping." The unit comprises of the localized charge carrier and its atomic deformation is termed as small polaron when the carrier is essentially confined to a single atomic site. Since, small polaron is localized in nature so the absence of long range order in non–crystalline solids does not affect its motion.

## 1.4 Defect models

Defects determine the electronic and transport properties of materials which are relevant to its applications. Different models have been proposed for the defect formation in the amorphous materials which have been discussed below.

### 1.4.1 Mott, Davis and Street

Street and Mott [47], and Mott, Davis and Street [48], proposed a model for states in the gap of amorphous semiconductors. They considered $As_2Se_3$ having $10^{18}$–$10^{19}$ $cm^{-3}$ dangling bonds acting as point defects at which normal coordination cannot be satisfied. There are three dangling bond states; $D^+$, containing zero electrons, $D^0$, containing one electron and $D^-$, containing two electrons. Following Anderson [40], they assumed that a lattice distortion takes place when there is a change in the occupation of electron at dangling bonds. This distortion is sufficiently strong for reaction $2D^0 \rightarrow D^+ + D^-$ which is exothermic. The main objections to this model were the assumption of high density of dangling bonds and large negative effective correlation energy for chalcogenide glasses which is otherwise absent for tetrahedraly bonded amorphous materials.

### 1.4.2 Valence alternation pair

Kastner, Adler and Fritzsche [49] postulated the formation of valence alternation pair (VAP) which requires such a small energy of formation that their density in most of the glasses is relatively high. They proposed that each chalcogen atom in its ground state will form one positively charged three fold coordinated atom, and one negatively charged, one fold coordinated atom, *i.e.*, $2C_3^0 \rightarrow C_3^+ + C_1^-$. In addition to the atomic rearrangements accompanying the configuration changes, there are relaxation effects associated with a change in charge state of a given configuration [47]. VAP formation is also possible for group V atoms, but, cannot occur in group IV atoms because they cannot be fivefold coordinated.

## 1.5 Properties of chalcogenide glasses

By studying various properties the different aspects of the material can be studied. Physical properties are used to observe and describe materials while structural properties confirm the nature and bonding arrangement in the system. Thermal properties are characteristic of a material that determine how a material behaves when subjected to heat. Optical properties describe the response of a material when light passes through it. The aim of this section is to discuss the physical, structural, thermal and optical properties of chalcogenide glass systems.

### 1.5.1 Physical and structural properties

An earlier attempt to describe the structure of glasses as a disordered network of polyhedral units was made by Zachariasen [5]. The polyhedra themselves define the short–range order of the atomic arrangement in glass, whereas the random connectivity of the polyhedra gives rise to long–range disorder. Zachariasen postulated following rules for a glass forming oxide of the formula $A_mO_n$:

i. Oxygen atom may be linked to no more than two A atoms.
ii. The number of oxygen atoms surrounding A atoms must be small.
iii. The oxygen polyhedra share only corners with each other, neither edges nor faces.
iv. At least three corners in each polyhedron must be shared.

The crystalline and glassy structure of an oxide $A_2O_3$ has been shown in Figure 1.4. Therefore, Zachariasen defined glass as an extended network of corner sharing polyhedra which lacks periodicity and whose energy is comparable to that of corresponding crystalline network.

In order to extend the glass forming range of oxides by the addition of alkali oxides, a modified version of Zachariasen rules were formulated as [5]:

i. A sufficient percentage of cations are surrounded by oxygen tetrahedra or triangles.
ii. The oxygen polyhedra have only corners in common.
iii. Some of the oxygen atoms are linked to only two cations and do not form any additional bonds.

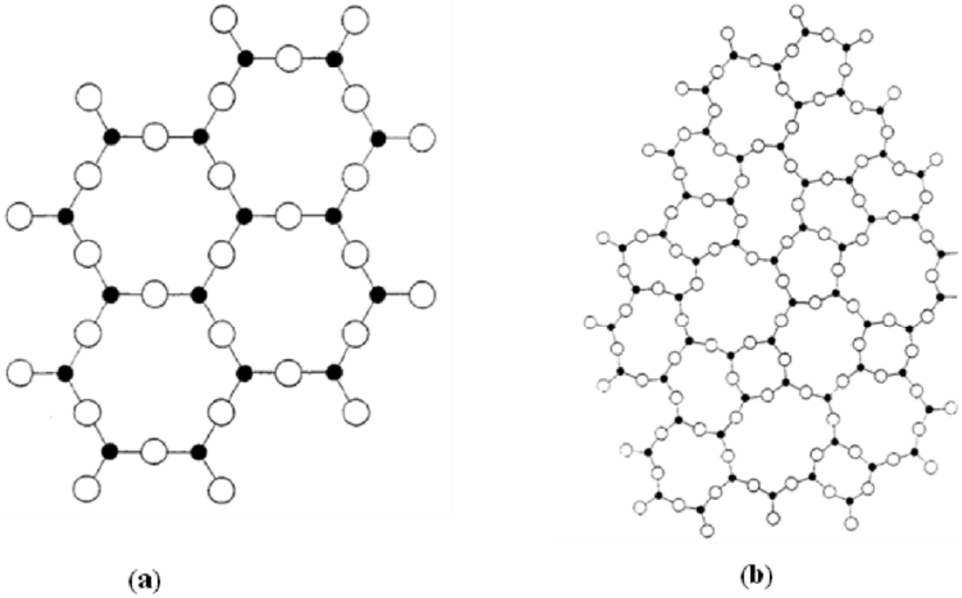

**Figure 1.4** Schematic representation of (a) $A_2O_3$ crystal (b) $A_2O_3$ glass.

When a non–glass forming oxide like $Na_2O$ enters into the $SiO_2$ structure, additional oxygen atoms participate in the network and cause rupturing of bonds. A *Si–O–Si* bond breaks and additional oxygen atoms saturate the *Si–* and *Si–O–* bonds. The oxygen which is connected to two Si atoms is called bridging oxygen and the one bonded to *Si* is called non–bridging oxygen. Later Warren *et al.* studied the structure of glass using x–ray diffraction technique and proved Zachariasen's idea [50].

But, Zachariasen's rules are largely inapplicable to non–oxide glasses, yet they provide a visualization of topological disorder in network forming glasses. There are two structural models based on the nearest neighbor covalent bonding, chemically ordered covalent network (COCN) [51] and random covalent network model (RCN)

[51], which describe the structure of chalcogenide glasses more appreciably. They only differ in their approach for the formation of bonds. In COCN, for a binary species $A_xB_{1-x}$, the formation of heteropolar *A–B* bonds is preferred over homopolar *A–A* and *B–B* bonds. The chemically ordered phase occurs, when only *A–B* bonds are formed at a composition $X_c = Z_A/(Z_A + Z_B)$, where $Z_A$ and $Z_B$ are coordination numbers of *A* and *B* atoms respectively. If the composition is rich in element *A* then *A–A* bonds are also formed in addition to *A–B* bonds and vice–versa. On the other hand in random covalent network model the bond energies do not influence the formation of bonds. All the three bonds *A–A*, *B–B* and *A–B* are equally probable except at $x = 0$ and $x = 1$.

Infrared (IR) spectroscopy is one of the most common spectroscopic techniques used by organic and inorganic chemists. It involves the absorption measurement of different IR frequencies by a sample positioned in the path of IR beam. An IR spectrum represents fingerprint of a sample with absorption peaks which correspond to the frequencies of vibrations between the bonds of the atoms constituting the material. No two compounds produce same IR spectrum as each different material is a unique combination of atoms. The size of the peaks in the spectrum is a direct indication of the concentration of material present. Therefore, IR spectroscopy results in an identification of different kind of constituting materials.

Far–IR studies have been carried out on many chalcogenide systems. Kumar *et al.* [52] characterized the vibrational bands for $Sb_2Se_3{:}Sn$. Vibrational band for $Sb(Se_{1/2})_3$ at 78 cm$^{-1}$ was observed while no *Sn* related peaks/bands were observed in the spectra. While studying the bonding arrangement of *Sn* addition to *SeTe* alloys, a band at 222–225 cm$^{-1}$ confirmed the presence of *Sn–Se* bond in $Sn(Se_{1/2})_4$ mode [53]. Wang *et al.* [54] reported that *Ge–Te–In* glasses present an excellent transmitting property in the Fourier Transform infrared spectra. There was no absorption in the 15–20 μm which is beneficial for far–IR transmitting applications.

Nikolic *et al.* [55] studied the far infrared reflectivity spectra of single crystal *PbTe* doped with *Bi*. For strong plasma–longitudinal–optical phonon interaction, two impurity local modes at 140 and 219 cm$^{-1}$, corresponding to the impurity atom in different valence states, were reported. The lower frequency modes were assumed to be a local bismuth mode representing the population of a metastable state Bi$^{2+}$. The other local mode at about 219 cm$^{-1}$ was proposed to be the result of electron transfer from the stable two electron state to the conduction band. Sharma *et al.* [56] studied the far–infrared spectra of $Ge_{10}Se_{90-x}Te_x$ glassy alloys measured in the wavenumber region 50–650 cm$^{-1}$ at room temperature. The addition of $Te$ in $Ge_{10}Se_{90}$ showed the appearance of $GeTe_2$ and $GeTe_4$ molecular units and vibrations of $Se$–$Te$ bond in $Se_{8-x}Te_x$ mixed rings. Some of the $Ge$–$Se$ and $Se$–$Se$ bonds disappeared leading to the formation of $Se$–$Te$ and $Ge$–$Te$ bonds. For higher $Te$ content the absorption peaks at 150 cm$^{-1}$ were reported. The results were supported by the decrease in optical band gap with the addition of $Te$ to $Ge_{10}Se_{90}$ alloys.

Singh *et al.* [57] made IR measurements of $Se_{98-x}Zn_2In_x$ ($x = 0, 2, 4, 6, 10$) in the wavenumber range 4000–400 cm$^{-1}$. The transmittance percentage of FTIR recorded spectra in the wavenumber range 1800 to 400 cm$^{-1}$ was maximum for $Se_{92}Zn_2In_6$ glass. The IR spectra of $Ge_{10}In_xSe_{90-x}$ samples was investigated by Adel *et al.* [58] in the wavenumber region 150–400 cm$^{-1}$. The addition of $In$ shifted some of bands to higher wave numbers, and also strengthened the $Se$–$Ge$ bonds. The vibrations of $GeSe_4$ tetrahedral units were reported at 340, 270, and 220 cm$^{-1}$. They observed that the system of $Ge$–$Se$ strengthened on $In$ addition.

Singh *et al.* [59] have studied the FTIR spectra in the wave number range 4000–400 cm$^{-1}$ for $Se_{93-x}Zn_2Te_5In_x$ system. The transmission percentage for $Se_{87}Zn_2Te_5In_6$ was maximum and this composition was reported as most suitable glass of the series for prospective uses. Pamukchieva *et al.* [60] have studied vibrational properties of the impurities in $Ge_xSb_{40-x}S_{50}Te_{10}$ bulk samples and thin films. The FTIR transmittance spectra of powdered glasses revealed that the water related impurities were dominant over the impurities of $O$– and $C$– containing complexes. The evaporated films were free from water impurities but absorption bands related to $Ge$–$O$ and $Te$–$O$ chemical bonds were detected, most probably due to oxidation of the surface region.

Petkov *et al.* [61] used the FTIR spectroscopy for studying changes in the structure of thin chalcogenide films $GeSe_2$–$Sb_2Se_3$–$AgI$. Two regions of absorption were observed in the IR spectra of bulk samples and thin films: the first one was situated between 225 and 325 cm$^{-1}$ and characterized the structure of $GeSe_2$. The second one between 125 and 225 cm$^{-1}$ gave information about the $Sb_2Se_3$ structure. It was observed that the addition of iodine (*I*) in the $GeSe_2$ layer did not change the position of the main peak at 256 cm$^{-1}$. The intensity of the peaks at 182 and 254 cm$^{-1}$ (corresponding to the $SbSe_{3/2}$ pyramidal and the $GeSe_{4/2}$ tetrahedral units) decreased with decreasing the *Ge* and *Sb* contents in the layers, respectively. For the layer with composition of 40 at.% *AgI* (24 at.% I), the intensity of the peak at 205 cm$^{-1}$ increased. Dai *et al.* [62] studied the IR transmission spectra of *Ge–Te–CuI*. Although *Ge–Te–CuI* glasses are normally black and do not exhibit any transmission in the visible spectral region, but these glasses have a wide transmission window from the NIR (1.8 µm) to the far IR (25 µm). The strongest absorption peak was located at 13 µm, which was ascribed to *Ge–O* covalent bonds vibrations. An absorption peak was observed between 9 and 10 µm whose origin was not elucidated. These new glasses exhibited a broad optical window, lying between 1.8 and 25 µm.

Philips proposed the idea of constraint counting in network forming glasses [63]. According to Phillips, the glass forming condition for a covalent network are constrained by bond stretching ($N_a$) and bond bending ($N_b$) forces. He proposed that a mechanical threshold exists, where total number of constraints ($N_t$) equals the degrees of freedom ($N_d$) *i.e.,* $N_t = N_d$. The composite material can be considered of as two phase materials, floppy and rigid. In the floppy regime, $N_t < N_d$ and the system is underconstrained. Conversely, in the rigid regime, $N_t > N_d$ and the system is overconstrained. Later, Philips and Thorpe [64] proposed that the rigidity threshold, describing the constraint free network with optimal glass forming ability, occurs at an average coordination number of 2.4. So, the above statement could also be postulated as, that the covalent network undergoes a qualitative change from being easily deformable at an average coordination number, $m < 2.4$ to being rigid at $m > 2.4$.

An intermediate phase in addition to floppy and rigid mode was discovered by Boolchand *et al.* [18]. Their results provided evidence for three distinct phases of network glasses: floppy, intermediate and rigid, as a function of progressive cross–linking or mean coordination number. The intermediate phase was characterized by a vanishing non reversing heat–flow, suggesting that glass compositions in this phase were configurationally close to their liquid counterparts, *i.e.* self–organized. The compositional width of the intermediate phase was reported to be determined by glass structure. In random networks, the width of the intermediate phase almost vanished, and a solitary floppy to rigid phase transition was observed, in excellent accord with extended constraint theory. According to Boolchand [18], in chalcogenides, some degree of self–organization invariably occurred. There existed an intermediate phase between the floppy and rigid phases, signaling the breakdown of mean–field constraint theory. This was in agreement with the numerical results on self–organized networks.

Lone pair electrons (*L*) play an important role in the formation of chalcogenide glasses which can be understood in terms of valence shell electron pair repulsion theory. Zhenhua *et al.* [65] proposed that chemical bonds with lone–pair electrons are more flexible and thus, easier to deform. An increase in number of lone pair electrons decreases the strain energy and a structure with large number of lone pair electrons favor glass formation. However, if the number of lone pair electrons in the structure exceeds a certain limit, the vitreous state is not achieved [65]. This is because the interaction among the lone pair electrons at shorter distances is repulsive which causes steric hindrance.

Glass transition temperature ($T_g$) is a measure of rigidity of the structure which in turn depends upon the mean coordination number (*m*) or mean bond energy ($<E>$). Tichy–Ticha [66] examined the correlation between the glass–transition temperature of 186 chalcogenide glasses and used the overall bond energy of the covalent glassy network by taking into account chemical bond approach as the first approximation. The bonding arrangement in the covalent network mainly determines the value of glass transition which does not mean that intermolecular interactions have no influence on glass transition. In fact these interactions play a vital role in the relaxation phenomenon in glasses.

Singh *et al.* [67] theoretically predicted the physical parameters of $(Se_{80}Te_{20})_{100-x}Ag_x$ ($0 < x < 4$) glassy alloys. The mean coordination number (*m*) increased while *L* decreased with an increase in *Ag* content. The decrease in value of $T_g$ showed that the rigidity of the system decreased with increase in *Ag* content. The effect of *Ge* addition on the physical properties of $(Se_{80}Te_{20})_{100-x}Ge_x$ ($x = 0, 2, 4, 6$) was studied by Mainika *et al.* [68]. An increase in *m* with increasing *Ge* content was correlated to an increase in the compactness of the structure. The number of lone–pairs decreased with increasing *Ge* due to interaction between the *Ge* ion and the lone–pair electrons of bridging *Se* atoms. Sharma *et al.* [69] calculated the physical parameters of $Ge_{17}Se_{83-x}Sb_x$. A mechanical percolation threshold was reported at $x = 6$. With an increase in *Sb* content, number of lone pair electrons decreased. The value of $T_g$ increased with *Ge* at.% which was attributed to the formation of three dimensional structural units $SbSe_{3/2}$ and $GeSe_{4/2}$, and to the decrease of content of chain like formation of excess *Se*.

### 1.5.2 Thermal properties

Material selections for components that are exposed to excessive heat or heat fluctuations require understanding of the thermal properties and responses of materials. For example, if a material is to be used in a storage device then it should have a lower crystallization time in order to facilitate a rapid phase change. The material selection can be made by studying its thermal characteristics with time. Thus, it is important to have an insight into the thermal properties of the materials.

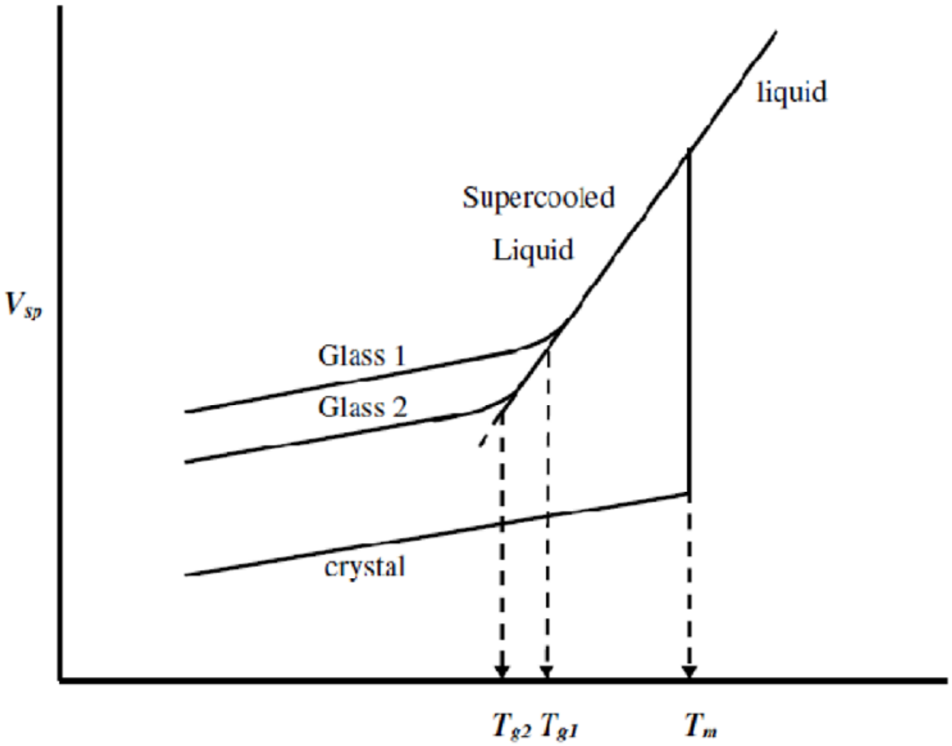

**Figure 1.5** Schematic representation of specific volume as a function of temperature of liquid which can crystallize as well as form glass.

Glasses are formed in the process of glass transition or vitrification which is very particular in its physics, kinetics and thermodynamics. The reverse process is called devitrification which is generally, but not always, accompanied by crystallization.

Figure 1.5 shows the vitrification process for a typical liquid. The specific volume ($V_{sp}$) *vs.T* graph shows that a liquid may crystallize at melting temperature ($T_m$) upon cooling. This first order transition usually results in a decrease of $V_{sp}$. On the other hand, the liquid which manages to surpass $T_m$ without crystallization is called a supercooled liquid. As the temperature of supercooled liquid is decreased, the viscosity increases and the molecules comprising it move slowly. These arrangements are necessary to achieve equilibrium $V_{sp}$ at that temperature. At temperatures not much lower than this, the material is practically frozen and is termed as glass [70]. The range of temperature over which this transition takes place is called the transformation range. $V_{\mathrm{sp}}$ continues to decrease as the temperature decreases, but the thermal expansion coefficient is significantly smaller in the glassy state as compared to liquid and supercooled liquid states. The glass transition temperature ($T_{\mathrm{g}}$) is different for different cooling rates (Figure 1.6). A smaller cooling rate allows the sample to stay in the supercooled liquid state until lower temperatures. Generally, the dependence of $T_{\mathrm{g}}$ upon cooling rate is relatively weak. An order of magnitude change in cooling rate may change $T_{\mathrm{g}}$ by only 3–5 K. The supercooled liquid and the glass are considered to be metastable and unstable respectively. In contrast to a supercooled liquid, a glass relaxes continually, possibly too slowly to measure, toward a more stable state. This implies that a glass is mechanically stable for practical purposes, even though it is thermodynamically unstable [70]. A supercooled liquid may also be classified as strong or fragile [71]. Strong liquids show Arrhenius relaxation processes and have three dimensional network structures of covalent bonds. Fragile liquids follow non–Arrhenius relaxation processes and in these liquids molecules interact through non–directional and non–covalent interactions.

The crystallization of a liquid or an amorphous solid involves simultaneous nucleation and growth of crystallites [72]. The nucleation of crystals either occurs without the involvement of a foreign substance called homogeneous nucleation or with the involvement of a foreign substance acting as a preferred nucleation site called the heterogeneous nucleation. In order to form these nuclei two distinct barriers are to be overcome. First is the kinetic barrier and second is thermodynamic barrier [73]. The kinetic energy is the activation energy required by an atom to cross the liquid–nucleus interface. The second, thermodynamic barrier is the net free energy change in the system when a nucleus is formed. This phenomenon has been shown in Figure 1.6. It shows two different energetic contributions to the nucleation. First, a free energy decrease which is associated with the transformation of glass to a crystal (volume energy gain) and second the increase in surface energy (surface energy barrier) that inhibits the formation of the crystal. The crystal, having lower energy, is thermodynamically more stable than that in a metastable state. Hence, when the surface energy barrier is overcome, a crystal is formed.

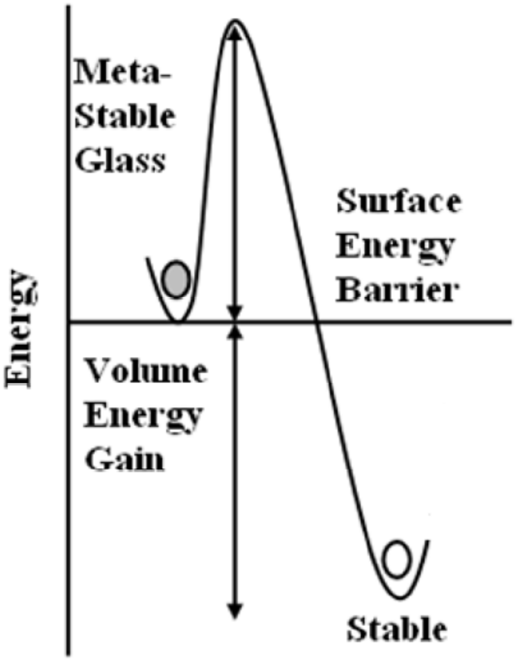

**Figure 1.6** Energetic contributions to nucleation.

The crystal growth is the successive process of nucleation in which the critical nuclei grow to form a crystal. Crystal growth takes place by fusion and re–solidification of the material *i.e.*, molecules get arranged within a solid material in an orderly repeating pattern extending in all three spatial dimensions. In the crystal growth process stoichiometry of the glass compositions does not undergo any compositional changes [74]. Thus, interfacial rearrangements are likely to control the crystal growth process.

The crystallization kinetics of amorphous materials is the study of crystallization with respect to time or temperature. The crystallization kinetics can be studied via isothermal or non–isothermal modes of differential scanning calorimetry (DSC)/differential thermal analysis (DTA). The kinematical studies are always associated with the activation energies generally interpreted at glass transition and crystallization. In the glass transition phenomenon, it is related to the activation energy of relaxation. The glass crystallization phenomenon is related to nucleation and growth processes which dominate the devitrification of most of the glassy systems. Although separate activation energies must be identified with individual nucleation and growth steps in a transformation, but they are usually combined into activation energy representative of the overall crystallization process. The rate of crystallization and thermal stability are the important factors to decide whether the system can be used for threshold or memory type switching.

DSC was used by Abu–Sehly [75] to probe the dynamics of the glass transition in $As_{22}S_{78}$ chalcogenide glass. Non–isothermal measurements were performed at different heating rates (5–35 $Kmin^{-1}$). Glass transition temperature shifted to higher values with increasing heating rate. The activation energy of glass transition was calculated from the heating rate dependence of $T_g$. The observed temperature dependence of the activation energy was consistent with the free volume model of the glass transition. Crystallization studies for $Se_{0.95}In_{0.05}$ and $Se_{0.90}In_{0.10}$ were carried out by Kotkata *et al.* [76] under non–isothermal conditions at different heating rates. It was realized that a rate controlling process occurred where random nucleation of one– to two–dimensional growth was accompanied with the introduction of up to 10 at.% *In* into glassy *Se* matrix. The activation energy for crystallization ($E_c$) was determined using four models where a satisfactory concurrence was achieved. The value of $E_c$ showed a decrease with an increase in the *In*–content indicating higher extent of crystallization.

The crystallization kinetics study of $Ga_{15}Se_{85-x}Ag_x$ was carried out by Ghamdi *et al.* [77] using differential scanning calorimetry. The value of activation energy of crystallization increased with an increase in *Ag* concentration indicating faster rate of crystallization. The glass with 8% of *Ag* was found to be most stable. Abu–Sehly [78] investigated the kinetics of crystallization using DSC for $Se_{81.5}Te_{16}Sb_{2.5}$. The activation energy calculated from three isoconversional methods was found to vary with the extent of conversion and hence with temperature. The activation energy decreased with temperature. They showed that the transformation from amorphous to crystalline phase is a complex process involving different mechanisms of nucleation and growth.

Deepika *et al.* [79] employed DSC at five heating rates to investigate the glass–crystal transformation in $Ge_{1-x}Sn_xSe_{2.5}$ ($0 \leq x \leq 0.5$) under non–isothermal conditions. The glassy alloys (except 0.3) showed single glass transition and crystallization region. $T_c - T_g$ was found to be lowest for $Ge_{0.7}Sn_{0.3}Se_{2.5}$ showing stability in comparison to other samples. Fayek *et al.* [80] studied the crystallization kinetics of $As_{30}Se_{70-x}Sn_x$ ($x = 0, 1, 2, 3$) using differential thermal analysis. The average value of activation energy for glass transition ($E_g$) varied from 51.08 to 136.74 kJ/mol. Glassy alloy with $x = 2$ was found to be the most stable alloy. The glass transition behaviour and crystallization kinetics of $Se_{58}Ge_{42-x}Pb_x$ ($x = 9, 12$) was investigated using DSC [81]. The glassy systems $Se_{58}Ge_{33}Pb_9$ and $Se_{58}Ge_{30}Pb_{12}$ exhibited single $T_g$ and double crystallization on heating. From the values of $E_g$ and $E_c$, it was found that the modified phase obtained after annealing the sample, was less stable than the two phases obtained before annealing in both the samples.

Singh *et al.* [82] reported the non–isothermal crystallization kinetics of $Se_{98-x}Zn_2In_x$ ($0 \leq x \leq 10$) chalcogenide glasses. The activation energy showed a minimum at a composition corresponding to $x = 6$ due to a slower crystallization rate for this composition. The thermal properties of semiconducting chalcogenide $Sb_xSe_{55-x}Te_{45}$ ($2 \leq x \leq 9$) were studied by Prashanth *et al.* [83]. The addition of *Sb* was found to enhance the glass forming tendency and stability, and an increase in the glass transition width $\Delta T_g$. Glass transition temperature exhibited a subtle increase, suggesting a meager network growth with the addition of *Sb*. The values of $T_c$ were also observed to increase with *Sb* content.

Dahshan *et al.* [84] investigated the influence of copper addition on the thermal stability, $E_g$ and $E_c$ for $Ge_{26}Te_{74-x}Cu_x$ ($x = 2.5, 5, 7.5, 10, 12.5$) glasses. The values of $T_g$ decreased with increasing *Cu* content. The composition dependence of various parameters showed an increase in thermal stability of the glasses with increasing *Cu* content. Shaaban *et al.* [85] presented the results of kinematical studies of glass transition and crystallization in glassy $Se_{85-x}Te_{15}Sb_x$ ($x$ = 2, 4, 6 and 8) using DSC. The activation energies, $E_g$ and $E_c$, were reported to increase with increasing *Sb* content. An increase in $E_c$ was interpreted in terms of increasing cohesive energy. Addition of *Sb* turned the glasses more stable due to an increase in $Sb_2TeSe_2$ phase. Two mechanisms were reported to work simultaneously during the amorphous–crystalline transformation of the $Se_{83}Te_{15}Sb_2$ alloy while only one (three–dimensional growth) mechanism was responsible for the crystallization process of the chalcogenides $Se_{85-x}Te_{15}Sb_x$ ($x$ = 4, 6 and 8) glass.

Differential scanning calorimetry results for non–isothermal conditions of chalcogenide $(Sb_{15}As_{30}Se_{55})_{100-x}Te_x$ ($0 \leq x \leq 10$) glasses were reported and discussed by Aly *et al.* [86]. Addition of *Te* resulted in decrease of $T_g$, $T_c$ *and* $T_m$, $E_g$ and $E_c$. The crystallization kinetics of bulk $Se_{75}Te_{15-x}Cd_{10}In_x$ ($x$ = 0, 5, 10, 15) multicomponent chalcogenide glasses was studied using DSC at different heating rates (5, 10, 15 and 20 K/min) under non–isothermal conditions by Kumar *et al.* [87]. The onset crystallization temperature, peak crystallization temperature, $E_c$ and Hruby's parameter showed a reversal in their trend with *In* content at an average coordination number of 2.25. The results also showed that glassy $Se_{75}Te_{10}Cd_{10}In_5$ alloy has a maximum glass forming ability and is the most stable glass.

### 1.5.3 Optical properties

The optical behavior and mechanisms are very important *w.r.t.* the use of a material for various optical applications. Optical properties describe how light interacts with the material when passes through it. Refractive index ($n$) and absorption coefficient ($\alpha$) are two important optical parameters. Refractive index is defined as the ratio of velocity of light in vacuum to velocity of light in medium. In the complex refractive index, $n^*=n - ik$, $k$ is the extinction coefficient which is related to $\alpha$. Extinction coefficient indicates the amount of absorption loss when the electromagnetic wave propagates through the material. It is a useful parameter in the engineering of optical waveguides.

Optical absorption in amorphous semiconductors can be categorized into three main regions [88], high absorption region (i) with $\alpha \geq 10^4$ cm$^{-1}$ which is referred to as the fundamental absorption edge, exponential region (ii) with 1 cm$^{-1}$ < $\alpha$ < $10^4$ cm$^{-1}$ referred to as Urbach edge and weak absorption tail (iii) with $\alpha \leq 1$ cm$^{-1}$ referred to as Urbach tail (Figure 1.7).

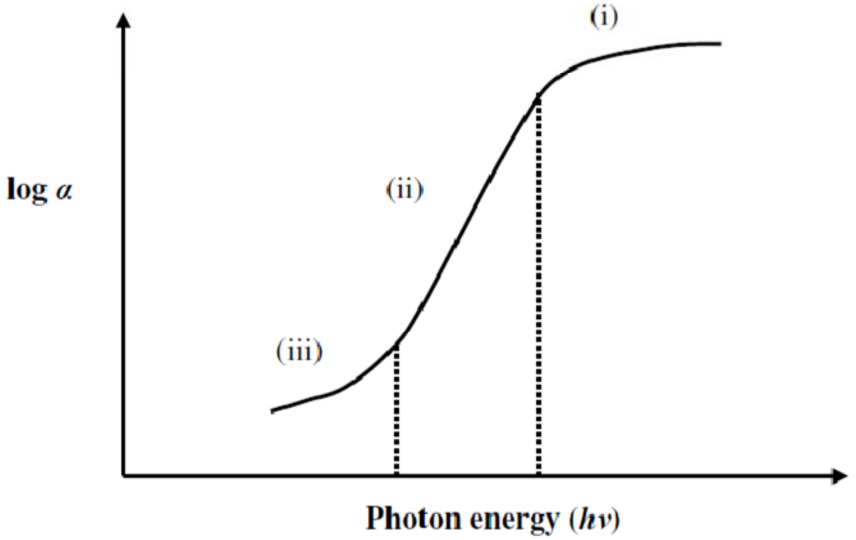

**Figure 1.7** Absorption spectrum of amorphous semiconductors.

Band gap is the energy needed to move a valence electron into the conduction band. When an electron undergoes transition from upper part of the valence band to the lower part of the conduction band, it causes dispersion near the fundamental absorption edge and gives rise to absorption spectrum. If this happens without the phonon participation and without a change in the crystal momentum then it is called direct transition (Figure 1.8). But, when there is interaction with phonon and a change in the crystal momentum, then it is called indirect transition (Figure 1.8). Both direct and indirect transitions give rise to frequency dependence of $\alpha$ near the fundamental absorption edge.

In high absorption region the frequency dependence of $\alpha$ is given by the power law [88],

$$\alpha h\nu = B\left(h\nu - E_g^{opt}\right)^p \tag{1.1}$$

where $p = 2$ for amorphous semiconductors, $B$ is a constant which depends upon the electronic transition probability and $E_g^{opt}$ is the optical band gap. In the exponential region, associated with the presence of localized states, $\alpha$ is described by [88],

$$\alpha h\nu = Const.\exp\left(\frac{h\nu}{E_s}\right) \tag{1.2}$$

where $E_s$ is the energy characterizing the slope and $\nu$ the frequency of electromagnetic radiation. In the weak absorption tail region below the exponential part, the shape depends on the preparation technique, constituent purity and thermal history of the material.

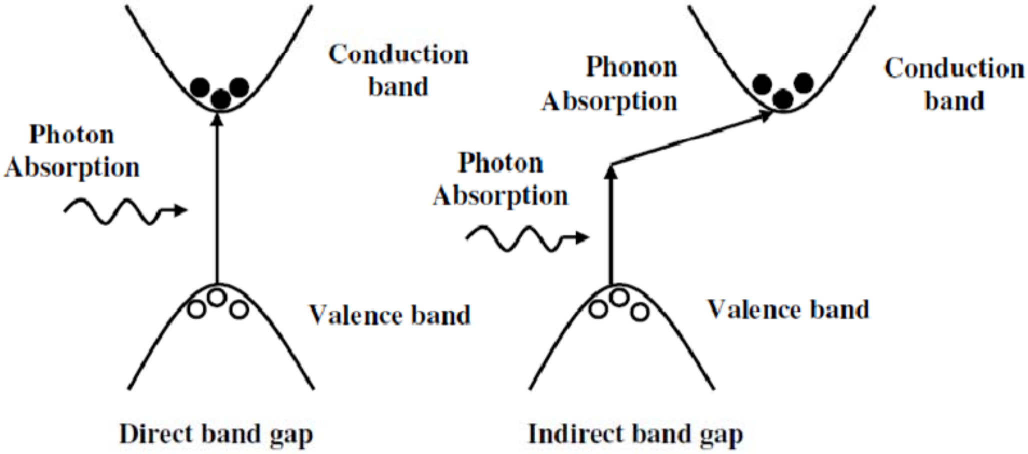

**Figure 1.8** Schematic representation of direct and indirect band gap.

Optical transmission of glasses is characterized by its optical window. At shorter wavelengths, the band gap limits the optical window, while at longer wavelengths the optical window is limited by the multi–phonon absorption. The multi–phonon absorption at longer wavelengths gives the interaction of light with vibrational modes of the chemical bonds inside the glass. The phonon energy is inversely proportional to the atomic mass of atoms. The larger atomic mass of chalcogenide elements is responsible for lower energies of phonon vibrations [89]. Chalcogenide glasses typically have optical windows that extend into the far infrared [90] making them a better candidate to be used for IR optical devices.

The optical transmission spectra of amorphous a–$Se_{1-x}In_x$ films prepared by thermal evaporation technique were recorded over the spectral region of 500–2500 nm by Kotkata *et al.* [91]. Optical band gap decreased and refractive index increased with increasing *In* content. The effect of *In* content on the optical constants of a–$Se_{100-x}In_x$ thin films prepared by flash evaporation technique was investigated by Ammar *et al.* [92]. The value of $\alpha$ increased while $E_g^{opt}$ decreased with increase in *In* concentration. This behaviour was attributed to the formation of *In–Se* bonds and subsequent decrease in the concentration of other bonds present in the glass.

Aly [93] studied the $E_g^{opt}$ and refractive index dispersion parameters of $As_xSe_{70}Te_{30-x}$ ($0 \leq x \leq 30$) amorphous thin films deposited by thermal evaporation technique. Refractive index and dispersion energy ($E_d$) decreased while $E_g^{opt}$ and single oscillator energy ($E_0$) increased with *As* content. Sharma *et al.* [94] reported the effect of *Bi* addition on the optical behaviour of $Ge_{20}Te_{80-x}Bi_x$ glassy alloys. Refractive index increased with increase in *Bi* content. The values of $E_d$ and static refractive index ($n_0$) increased while $E_0$ decreased with *Bi* content. Optical bad gap decreased from 0.86 to 0.74 eV with *Bi* addition.

El–Gendy [95] studied the refractive index and optical band gap of e–beam evaporated $Ga_{10}Ge_{10}Te_{80}$ films. Optical absorption coefficient revealed the presence of an indirect optical transition for as–deposited (amorphous) films, whereas it has a direct and indirect optical transition for the annealed (crystalline) films. Sharma *et al.* [96] studied $Ge_{10}Se_{90-x}Te_x$ ($x = 0, 10, 20, 30, 40, 50$) thin films for optical properties. Optical bad gap was found to decrease with increase of *Te* content. The value of $n$ decreased upto $x = 30$ and thereafter increased with *Te* content.

Fouad *et al.* [97] studied the optical properties of $As_{30}Se_{70-x}Sn_x$ thermally evaporated thin films. The value of $E_g^{opt}$ decreased with increase in *Sn* content. The stoichiometric composition with $x = 3$ exhibited quite different behaviors as a result of the *Sn* alloying effect. The optical constants of $Se_{96-x}Te_4Ag_x$ ($x = 0, 4, 8, 12$) thin films were studied by Ghamdi [98] as a function of photon energy in the wavelength range 500–1000 nm. The value of $n$ decreased while $k$ increased with photon energy. The value of $E_g^{opt}$ increased with increase in *Ag* concentration. It was suggested that due to the large absorption coefficient and compositional dependence of reflection, these materials may be suitable for optical data storage.

The compositional dependence of the optical properties of vacuum evaporated amorphous $Ge_xSe_{80-x}Pb_{20}$ films was reported by Kumar *et al.* [99]. Refractive index and extinction coefficient decreased at first with increasing *Ge* up to 20 at.% and then increased at 25 at.% *Ge*. Optical band gap increased with the substitution of *Se* for *Ge* up to 20 at.% and then decreased at 25 at.% *Ge*. Dahshan *et al.* [100] reported the effect of replacement of *Se* by *Ge* on the optical constants of chalcogenide $Ge_xAs_{20}Se_{80-x}$ ($x = 0, 5, 10, 15$ and 20) thin films. The transmission spectra of the films at normal incidence were obtained in the spectral region from 400 to 2500 nm. The value of $n$ and $k$ decreased while $E_g^{opt}$ increased with *Ge* addition. The increase in the optical band gap with increasing *Ge* content was interpreted in terms of chemical–bond approach.

Marquez *et al.* [101] analyzed the effect of *Ag* content on the optical properties of *Ag*–photodoped a–$(As_{0.33}S_{0.67})_{100-x}Te_x$ thin films. The value of $E_g^{opt}$ decreased with increase in the concentration of photodoped *Ag*. The maximum change in the index of refraction, between the *Ag* photodoped and undoped material, was found around 15 at.%. The optical properties of thin $As_2S_3$–$In_2S_3$ films, deposited by thermal coevaporation of $As_2S_3$ and $In_2S_3$, were reported by Todorov *et al.* [102]. The refractive index increased from 2.45 to 2.59, while $E_g^{opt}$ decreased from 2.40 eV to 2.18 eV for thin films with composition $As_{40}S_{60}$ and $As_{26.8}S_{60.1}In_{13.1}$, respectively. The addition of *In* leads to a decrease in the photoinduced changes in the refractive index in the visible and near–infrared region.

## 1.6 Motivation of thesis

There is vast spectrum of potential applications of chalcogenide glasses. But, recently an entirely different and interesting domain of applications has been proposed in the field of electronics and optoelectronics. A little attention had been paid to chalcogenide glasses because of the cheap and wide availability of silica based alternatives. However, silica based devices have certain limitations because of which chalcogenide glasses are receiving greater deal of response worldwide. Various applications of chalcogenide glasses have been realized and already been demonstrated in the fabrication of devices.

Most recently Samsung has presented a 20nm 1.8V 8Gb PRAM with 40 MB/s Program Bandwidth and Micron has announced the availability of 45 nm PCM featuring 1–gigabit (Gb) PCM plus 512–megabit (Mb) LPDDR2 in a multichip package for mobile devices – the first PRAM solution in volume production [103]. A single crystal chalcogenide semiconductor $Cu_3SbSe_3$ with anomalously low thermal conductivity, 0.7–1.0 W/mK, was observed which led to its announcement as a new possible thermoelectric material by the researchers [104]. A new class of materials known as topological insulators has been introduced that are insulators in the bulk but have protected conducting surface states arising from a combination of spin–orbit interactions and time–reversal symmetry which limits possible candidates to heavy elements and rather narrow bandgap materials [105]. Some of the known chalcogenide topological insulators are $Bi_xSb_{1-x}$, $HgTe$, $Bi_2Se_3$, $Bi_2Te_3$ and $Sb_2Te_3$ [106–108]. It has been speculated that topological insulators may be promising materials for quantum computing [109].

*CdTe* based solar cells were the first chalcogenide based cells basically developed to be used in space applications for communications satellites. $Cu(In,Ga)Se$ based chalcogenides have a reasonable efficiency of about11.5% with film thickness 1–2.5 μm [110] and high efficiencies approaching 19% have also been reported for laboratory scale devices by empirical optimization of process parameters [111]. Recently kesterite materials ($Cu_2ZnSn(S,Se)_4$) which are non–toxic, earth–abundant and low–cost have been proposed as alternatives [112]. Hsu *et al.* [113] reported superconductivity in the anti–*PbO* type *FeSe* at 8K. It was found that *Te* substituted *FeSe* and $FeSe_{1-x}Te_x$ have higher transition temperatures (~ 15 K) when $x = 0.5$. $FeSe_{0.5}Te_{0.5}$ coated superconducting tapes have been proposed for high field applications [114].

Metamaterials have the ability to focus and manipulate light on the nanoscale, far beyond the diffraction limit of conventional optics. Chalcogenide glasses have been used in rewritable optical disk technology for several decades as they provide fast and reproducible changes in optical properties in response to excitation [115]. This functionality can be brought to bear in the metamaterials domain to create switching devices. Samson *et al.* [116] have demonstrated a metamaterial electro–

optic switch of nanoscale thickness based on a chalcogenide glass hybridized with a nanostructured plasmonic metamaterial.

These advances are not possible without a good understanding of different properties of the chalcogenide material. The main motive of this thesis work is to examine how the composition dependent properties (physical, structural, thermal and optical) of multicomponent chalcogenide glasses vary and can be explored for different applications.

Among *S*, *Se* and *Te*, *S* is non metal while *Se* and *Te* are metalloids (both are semiconductors). In terms of glass formation, it is very difficult to vitrify a bulk *Te* melt even at high cooling rates. On the other hand, selenium vitrifies as an elemental glass which is fairly stable at room temperature. Sulphur (*S*) based compounds are very similar to *Se* based glasses, but, have received less attention due to their limited transmission in mid–IR region.

Amorphous *Se* is known to be composed of entangled chains and/or ring molecules, depending upon the preparation conditions Such structures are typical of organic polymers such as polyethylene because of which a–*Se* is generally referred to as an "inorganic polymer" [117]. Amorphous *Se* has a unique property of reversible phase transformation [118] making its glasses useful for memory devices. Commercially, a–*Se* and its alloys are used as photoconductor material in vidicon and x–ray imaging. In digital medical imaging, a–*Se* is used in direct conversion flat panel digital x–ray detectors. There are tremendous potential applications of a–*Se* based alloys [119, 120].

Amorphous *Se* tends to crystallize near room temperature. This temperature sensitivity limits its applications to be used as photoconductive material [121]. In order to overcome these problems, it is necessary to add more than one component like *Ge*, *Te*, *Sb*, *As* etc. into the *Se* matrix. Addition of *Te* to a–*Se* has shown a decrease in electrical resistivity and activation energy [122]. Sharp changes in the parameters for *Te* at.% > 50 have been ascribed to the phase transition from chain like structure to trigonal structure. Addition of *Te* decreases the $E_g^{opt}$ while increases refractive index [123]. Arsenic addition increases the glass transition temperature with increasing at.% [124]. The linear refractive index was found to be maximum and $E_g^{opt}$ minimum for *As* at.% 40 in a–*Se* [125]. The activation energy of crystallization decreases as *Ge* is added to a–*Se* [126]. The defect states are minimum for $x = 22$ in a–*Se* corresponding to which activation energy and photoconductivity show a maxima [127].

In the present study, antimony (*Sb*) has been selected as an additive to *Se* because *Sb* improves the thermal stability of a–*Se* drastically and decreases the ageing effects [128]. Antimony selenide chalcogenides have orthorhombic crystal structures. *SbSe* system, due to its higher photosensitivity has applications in photoconductive elements [129]. Some studies have shown that a–$Sb_2Se_3$ could also be a promising candidate for phase change memories [130]. Yoon *et al.* made direct comparison of antimony selenide with $Ge_2Sb_2Te_5$ (GST) and found that it might offer some advantages like shorter crystallization time and smaller amorphization current [131].

Shaaban *et al.* [132] have studied the optical properties of $Sb_xSe_{100-x}$ for $5 \leq x \leq 20$. Replacement of *Se* by *Sb* resulted in an increase in the density, *n* and *k* of these glasses while $E_g^{opt}$ decreased with increasing *Sb* concentration. Sharma *et. al.* [128] have also reported similar variation in *n*, *k* and $E_g^{opt}$ for $Se_{1-x}Sb_x$ for $x = 0, 0.025, 0.075, 0.10$. Kushwaha *et al.* [129] studied the temperature and intensity dependence of photoconductivity in $Sb_xSe_{100-x}$ thin films prepared by vacuum evaporation technique. Photosensitivity ($\sigma_{ph}/\sigma_d$), achieved a maximum value of 13.15 for $Sb_2Se_{98}$. Kostadinova *et. al.* [133] carried out structural study of the glassy binary system $Sb_xSe_{100-x}$ ($0 \leq x \leq 30$). Vibrational mode ~ 195 cm$^{-1}$ was a characteristic of *Sb–Se* bond in $SbSe_{3/2}$ pyramidal units. Holubova *et al.* [134] studied the thermal and structural properties of $Sb_xSe_{100-x}$ glass forming systems. The $T_g$ of $Sb_xSe_{100-x}$ changed slightly from 40 $^{o}$C to 48 $^{o}$C. Raman spectra confirmed that *Sb–Se* crystallizes from incongruent undercooled melt at lower temperature and trigonal *Se* crystallizes at higher temperature.

In the present study $Sb_{10}Se_{90}$ has been chosen as the base composition. Among the studied compositions $Sb_{10}Se_{90}$ is the best composition in terms of its ease of glass formation [135], low activation energy [129] and $E_g^{opt}$ [128]. However, it is difficult to substitute *Sb* in *Se* for $x > 10$ at.% to produce *Sb–Se* glassy alloys, by melt quenching technique [129]. Moreover, *Sb* has greater tendency to get crystallized and eutectic a–*SbSe* is less stable [136]. Therefore, it is necessary to add a network former (Group IV or V) such as *Ge*, *Sn*, *Ag* or *Bi* to establish cross linking between the tetrahedral and pyramidal units which facilitate stable glass formation. The addition of *Ag* to *Sb–Se* increases the dark conductivity and is found to be activated over the entire region [137]. Adding a third element like *Sn* to *SbSe* showed an amorphous phase up to 12.5 at% of *Sn* while crystal structures were obtained for $x = 15, 20, 30, 40$ [138].

Germanium has been chosen as an additive because it increases the glass forming domain of the system which for *Sb–Se–Ge* system from about 5 to 40 % *Sb*, 5 to 35 % *Ge* and the rest being *Se* [139]. It acts as a network modifier to establish cross linking between the tetrahedral and pyramidal units which facilitate stable glass formation. *Sb–Se–Ge* glasses have possible applications in IR optical devices because of their low material dispersion, low light scattering and long wavelength multiphonon edge. The addition of *Ge* to *Se–Pb* system has shown that $n$ and $k$ are minimum while $E_g^{opt}$ is maximum for $x = 20$ [140]. Similar results have been observed when *Ge* is added to *As–Se* [141] and *Se–Te* [142]. Increasing *Ge* content in *Pb–Se* increases the $T_g$ and $E_g$ of the alloys [143]. Therefore, *Ge* alloyed in varying concentrations $Sb_{10}Se_{90-x}Ge_x$ ($x = 0, 19, 21, 23, 25, 27$) has been studied for physical, structural, thermal and optical characteristics.

*Ge* is a good glass former with *Se* and has a good transparency in the two spectral regions 3–5 µm and 8–12 µm, but, has a disadvantage in wide energy gap which causes intrinsic optical losses, and imposes difficulties for applications in long distance fiber communication [144]. In order to overcome this limitation, the most stable of the ternary composition is taken for alloying with fourth element. Ma *et al.* [145] studied the *Ga–Ge–Sb–Se* system and found that *Ga* destabilizes the base system. For 5 at.% *Ga* samples were stable and did not crystallize. For *Ga* at.% > 15 the glass samples were difficult to obtain. No glass in *Ga–Ge–Sb–Se* was transparent in visible range while the glasses were transparent in 14–15 µm regions. Vassilev *et al.* [146] studied the addition of *Pb* as *Pb–Se* in $GeSe_2$–$Sb_2Se_3$. With the increase in *PbSe* the melting temperature increased. The increase in content of *PbSe* at low concentration of $Sb_2Se_3$ showed a favorable effect on glass forming ability.

Indium (*In*) has been observed to decrease the optical band gap of the material [147], suitable to explore the system for optoelectronic devices. Sharma *et al.* have reported that *In* addition to *Se–Te* system increases the dark conductivity due to an increase in the number of defects states [148]. Kumar *et al.* have reported that *In* addition to *Se–Te–Cd* shows a maximum for $T_c$ and $T_m$ at $x = 5$ at.% [87]. Moreover, the glass forming tendency has also been found to be maximum for same composition. Maan *et al.* [149] have studied the kinetics of glass transition in $Te_5(In_xSe_{100-x})_{95}$ glassy alloys. The value of $T_g$ increased with increasing *In* concentration while $\Delta E_g$ decreased and showed a minimum at $x = 20$. Currently, *In* has gained significant attention due to its potential applications in smart digital electronic devices [150]. These devices rely upon the non–volatile memory that uses reversible phase transition of chalcogenide resistor [150]. *In* based chalcogenides are also potentially used in non–linear optics in the infrared region [151]. So, in order to optimize the effect of increasing *Ge* concentration on different properties in ternary *SbSeGe* system, *In* has been added at the cost of *Ge* to the most stable of the ternary $Sb_{10}Se_{90-x}Ge_x$. The physical, structural, thermal and optical properties have been studied for varying *In* concentration in *SbSeGeIn* alloys. The thesis describes work on ternary $Sb_{10}Se_{90-x}Ge_x$ ($x$ = 0, 19, 21, 23, 25, 27) and quaternary $Sb_{10}Se_{65}Ge_{25-y}In_y$ ($y$ = 0, 3, 6, 9, 12, 15) glass alloys.

# CHAPTER 2

# Experimental techniques

The experimental research includes collecting and analyzing the data. The basic procedures involved like sample preparation, cleaning of substrates, vacuum conditions etc. play a significant role. The synthesis of samples under ambient conditions is necessary. While thin film deposition requires maintaining vacuum in the deposition chamber so as to keep the reacting gases out of the growing film and to keep high arrival energy of depositing species. It is also important to identify and outline a clear methodology of the data analyzing procedures. This chapter includes sample preparation techniques used for the present study and the various characterization techniques and methodology used to investigate the prepared samples for their structural, thermal and optical properties.

## 2.1 Bulk sample preparation

The melt quenching is one of the most established and widely used technique in the preparation of amorphous chalcogenide glasses. The chemical elements constituting the glass, weighed in appropriate atomic weight percentage, have been introduced in well cleaned quartz ampoules. These quartz ampoules have then been vacuum sealed in vacuum of $10^{-4}$ Pa using a vacuum pump and kept in a furnace. A very low heating rate has been maintained until the homogenization temperature, in order to avoid the rapid formation of vapor and therefore, the explosion of tube. The ampoules have been frequently rocked at the highest temperature for 10 h to make the melt homogeneous. The ampoules containing the melt have been quenched in ice cold water immediately after taking out the ampoules from the furnace. The quenched ampoules have been placed in a solution of $HF$ and $H_2O_2$ in order to separate the material from quartz ampoule. The samples were then extracted from the ampoules in the form of bullets. The obtained ingots have lustrous shine, a characteristic of glass. The ingots have been grounded to a fine powder using a mortar and pestle for the further characterization of the samples.

## 2.2 X–ray diffraction

X–ray diffraction (XRD) is a rapid analytical technique primarily used for phase identification of a crystalline material and can provide information on unit cell dimensions. Max von Laue, in 1912, discovered that crystalline substances act as three–dimensional diffraction gratings for x–ray wavelengths similar to the spacing of planes in a crystal lattice.

XRD is based on constructive interference of monochromatic x–rays and a crystalline sample. The incident beam diffracts from the planes of crystallites orientated at the correct angle to fulfill the Bragg condition ($n'\lambda=2d'\sin\theta$). These diffracted X–rays are then detected, processed and counted. The conversion of the diffraction peaks to d–spacings allows identification of the mineral because each mineral has a set of unique d–spacings.

For a powder x–ray diffractometer (PXD), an x–ray source of copper is usually utilized. This creates an emission of white x–rays at lower wavelengths. For higher wavelength values two very prominent peaks of $K_\alpha$ and $K_\beta$ radiation are obtained. These lines are a result of the bombarding electrons knocking electrons from the innermost K shell of the copper source. Subsequent vacancies are then filled by other electrons dropping down from the above shells (L shell for $K_\alpha$, M shell for $K_\beta$). PXD utilizes monochromatic x–rays, normally $K_\alpha$, (since these are the most intense) by use of a monochromator which is fitted and filters out the unwanted wavelengths. The sample is rotated in the path of the source and the diffracted beam leaves the sample at an angle of $2\theta$ to the incident beam (Figure 2.1). This is collected by a detector adjacent to the x–ray source.

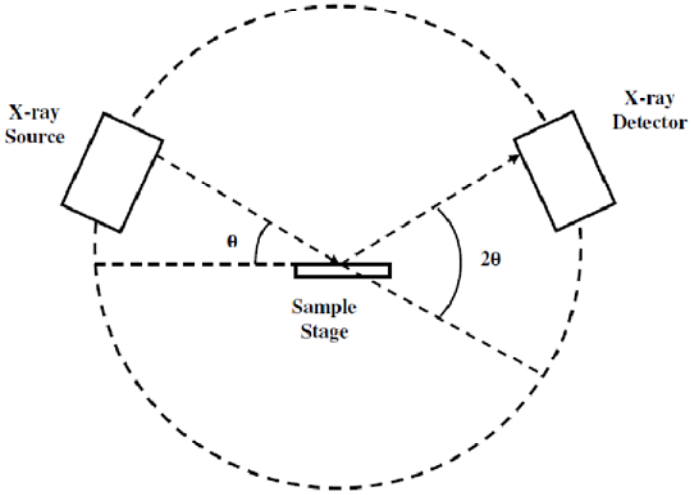

**Figure 2.1** Schematic of a powder x–ray diffractometer.

Figure 2.2 shows the XRD patterns of crystalline and amorphous materials. The crystalline material exhibits sharp diffraction peaks while no sharp peaks are observed in the spectra of amorphous materials.

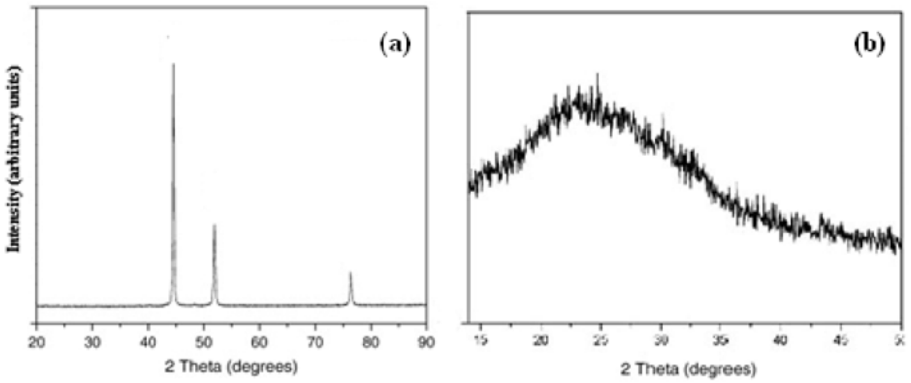

**Figure 2.2** XRD pattern of (a) crystalline and (b) amorphous material.

The nature of the bulk samples (amorphous, polycrystalline or crystalline) has been confirmed by powder XRD. Finely powdered samples have been used to take the XRD patterns. Analytical X'Pert Pro x–ray diffractometer (Radiation used was $Cu–K_{\alpha}$, $\lambda$ = 1.540598 Å, 40 KV and 25 mA) has been used to plot the XRD patterns of the samples. Data acquisition has been made in the $2\theta$ range from $10^{o}$ to $100^{o}$ with a step size of $0.05^{o}$.

## 2.3 Energy dispersive x–ray analysis

Energy dispersive x–ray analysis (EDX) is an x–ray technique used to identify the elemental composition of materials. The electron beam stimulate the atoms in the sample with uniform energy and they instantaneously send out x–rays of specific energies for each element, the so called characteristic x–rays. This radiation gives information about the elemental composition of the sample. EDX system is comprised of three basic components, an x–ray detector, pulse processor and a multiple channel analyzer (MCA). An x–ray detector detects and converts x–ray into electronic signals. A pulse processor measures the electronic signals to determine the energy of each x–ray detected and MCA displays and interprets the x–ray data. The block diagram for EDX measurements has been shown in Figure 2.3.

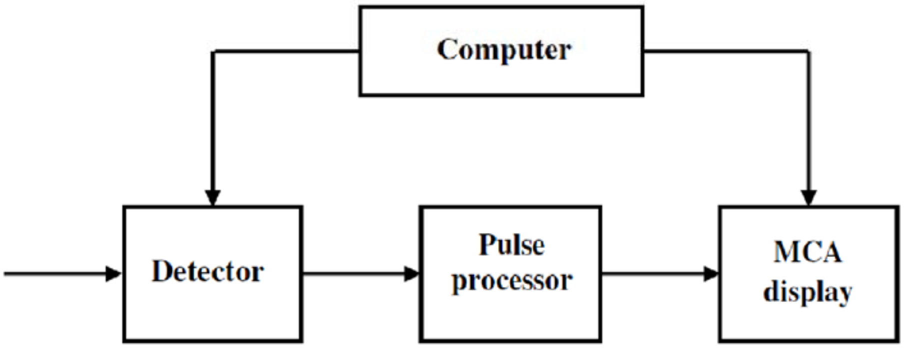

**Figure 2.3** Block diagram of components for EDX measurements.

## 2.4 Fourier–Transform infrared spectroscopy

Fourier–Transform infrared (FTIR) spectrophotometer is an instrument which obtains spectra in the range from NIR to FIR. Unlike a dispersive instrument *i.e.*, grating monochromator or spectrograph, FTIR collects all frequencies simultaneously. FTIR employs a very simple optical device called an interferometer. Interferometer produces a unique type of signal which contains all the infrared frequencies. This signal can be measured very quickly and so, the time element per sample is reduced to a few seconds.

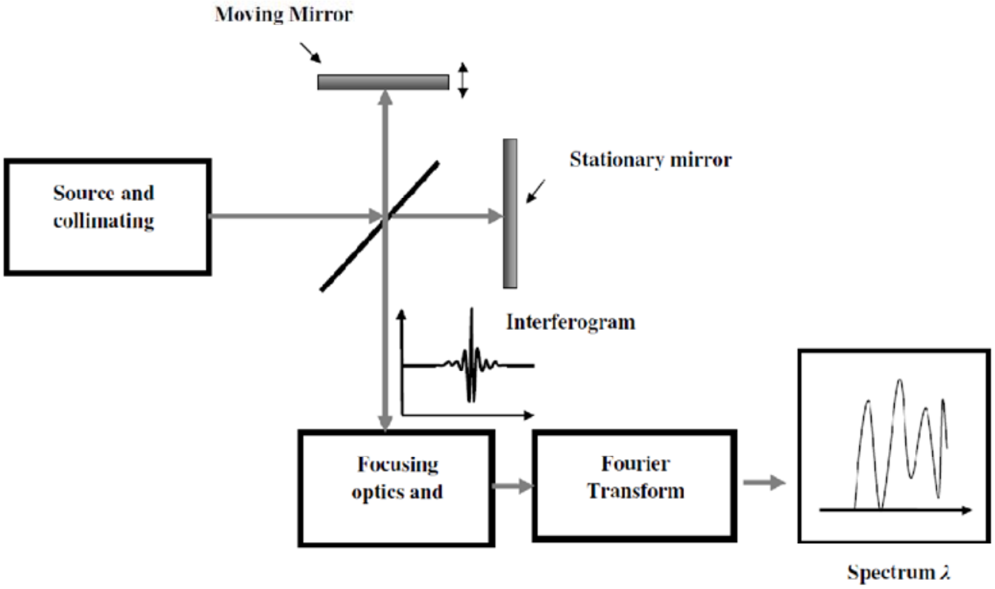

**Figure 2.4** Schematic of Fourier transform infrared spectrophotometer

Most interferometers employ a beam splitter which divides the incoming beam into two optical beams. One of the beam get reflected off from a flat mirror which is fixed in place. The other gets reflected off from a flat mirror which is on a mechanism that allows this mirror to move a very short distance away from the beam splitter. The two reflected beams recombine when they meet back at the beam splitter. The signal that is collected from the interferometer is the result of interference of two beams, one travelling with the fixed length and the other whose path is constantly changing as the mirror moves. The resulting signal is called an interferogram which contains the response of the sample to infrared frequency incident from the source. The measured interferogram cannot be interpreted directly. A means of decoding the individual frequencies is required which is accomplished by mathematical technique 'fourier transform' performed by the computer.

The far–IR transmission spectra of the alloys have been recorded using Fourier transform infrared spectrophotometer (Perkin Elmer–Spectrum RX–IFTIR) from 50 to 350 cm$^{-1}$. The resolution has been set at 1 cm$^{-1}$. Measurements have been made using the polyethylene pellet (13 mm diameter) method. The pellets have been made by mixing 2 mg sample with 200 mg of spectroscopic grade polyethylene and pressed into pallets. To take account of the polyethylene absorption, the polyethylene spectrum has been taken as reference.

## 2.5 Differential thermal analysis

Thermal analysis comprises a group of techniques in which a physical property of a substance is measured as a function of temperature, while the substance is subjected to a controlled temperature programme. In differential thermal analysis (DTA), the temperature difference that develops between a sample and an inert reference material is measured, when both are subjected to identical heat treatments. This differential temperature is then plotted against time, or against temperature. The related technique of differential scanning calorimetry (DSC) relies on differences in energy required to maintain the sample and reference at an identical temperature. The range of temperature measurable in the course of DTA is much larger than thermogravimetric (TG) determination. Thus, during TG, pure fusion reactions, crystalline transition, glass transition, crystallization and solid state reactions with no volatile product would not be indicated because they provide no change in mass of the specimen. However, these changes are indicated during DTA by endothermal or exothermal departure from the base line as shown in Figure 2.5.

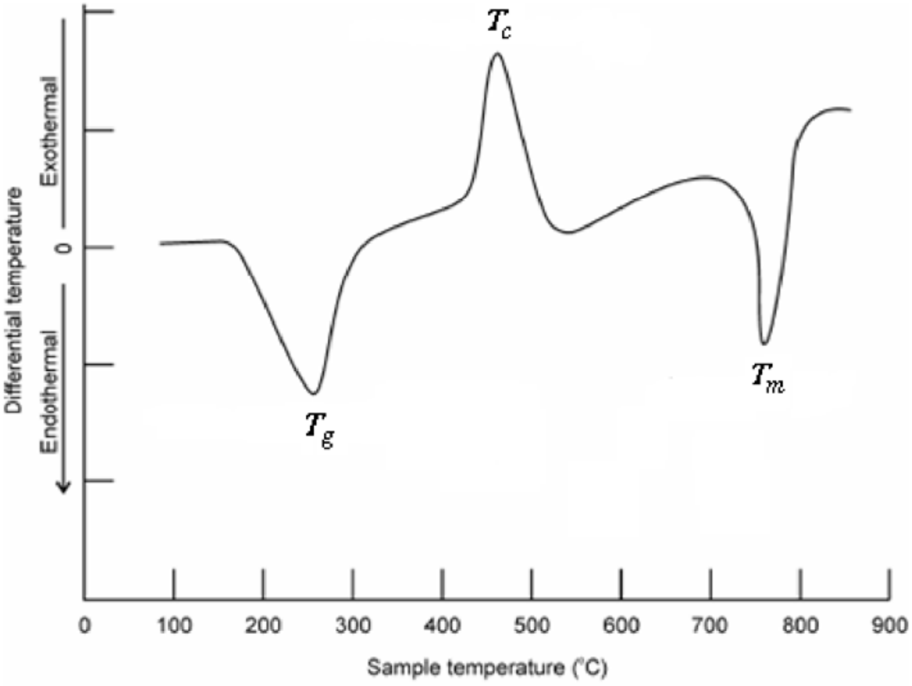

**Figure 2.5** Typical DTA curve indicating $T_g$, $T_c$ and $T_m$.

In DTA, a sample of material under investigation (specimen) is placed by the side of thermally inert material (the reference sample) usually calcite or $\alpha$ alumina in suitable sample holder or block. The temperature difference between the two is continuously recorded as they are heated. The block is heated in an electric furnace *i.e.* both are heated under identical conditions.

The thermal behavior of the samples has been investigated using DTA (EXSTAR TG/DTA 6300). DTA runs have been taken at four different heating rates 5 K/min, 10 K/min, 15 K/min and 20 K/min. For each run, approximately 10 mg of the sample has been taken in alumina pans in an atmosphere of dry nitrogen at a flow rate of 200 ml/min under non–isothermal conditions. The analyzer has been calibrated prior to the measurements using the known latent heats of high purity elements zinc, indium and lead. The temperature precision of microprocessor of thermal analyzer is ± 0.1 K.

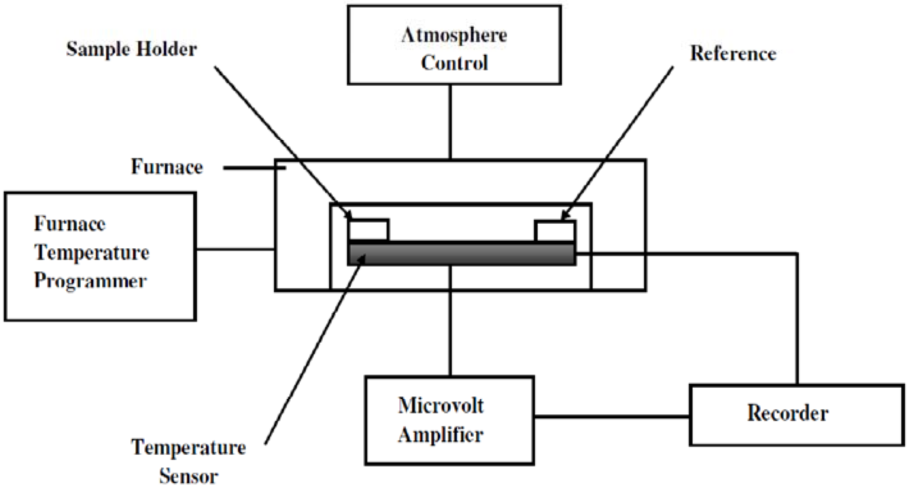

**Figure 2.6** Differential thermal analysis complete layout.

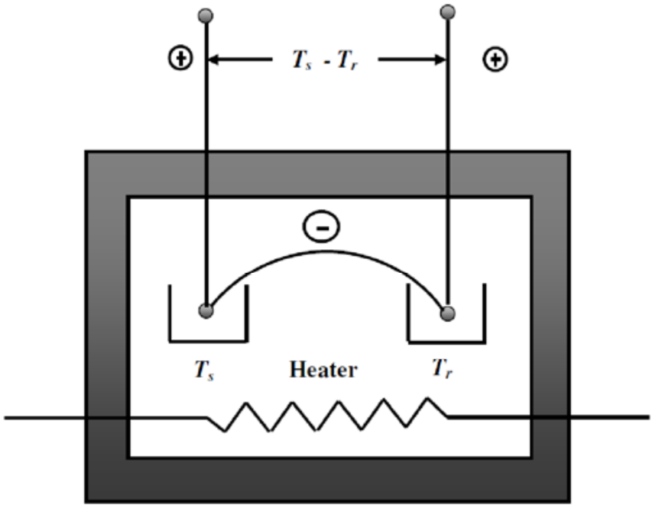

**Figure 2.7** Furnace part sharing continuous heating of sample and reference.

The DTA curves obtained have been analyzed to obtain the activation energies, interpreted with the help of well defined statistical approximations which are described below.

Kissinger first demonstrated that the variation in peak temperature can be used to determine the activation energy for a first order reaction [152]. Later on, this method was extended to higher order reactions also [153]. The Kissinger method is appropriate not only for the homogeneous reactions but also for heterogeneous reactions, well described by Avrami equation in isothermal experiments. For the crystallization processes with spherical nuclei, Kissinger equation is,

$$\ln\left(\frac{\beta}{T_c^2}\right) = -\frac{E_c}{RT_c} + constant \tag{2.1}$$

where $\beta$ is the heating rate, $T_c$ is crystallization temperature, $E_c$ is activation energy of crystallization and $R$ is gas constant.

Inspite of the fact that the above equation is used for the evaluation of $E_c$, it is suggested that this relation is also valid for glass transition process [154, 155] and hence, the above equation for its use in glass transition kinetics takes the form,

$$\ln\left(\frac{\beta}{T_g^2}\right) = -\frac{E_g}{RT_g} + constant \tag{2.2}$$

where $E_g$ is activation energy for glass transition and $T_g$ the glass transition temperature.

The heating rate dependence of $T_g$ has been interpreted by Moyinihan *et al.* [156] in terms of thermal relaxation phenomenon. They proposed that dependence of $T_g$ on heating rate yields information regarding temperature dependence of relaxation time. The relaxation equation is,

$$\frac{d(\ln\beta)}{d\left(1/T_g\right)} = -\frac{E_g}{R} \tag{2.3}$$

Equation (2.3) states that $\ln \beta$ versus $1/T_g$ plot should be straight line and the activation energy involved in molecular motion and rearrangements around $T_g$ can be calculated from the slope of the plot.

The approximation of Mahadevan *et al.* [157] can be used where the variation of $1/T_c^2$ with $\ln \beta$ is much slower than that of $1/T_c$ with $\ln \beta$. Equation (2.1) can then be simplified to,

$$\ln\beta = -\frac{E_c}{RT_c} + constant \tag{2.4}$$

The slope of $ln\ \beta$ versus $1/T_c$ gives the value of $E_c$.

$E_c$ can also be evaluated using second approach given by Augis and Benett [158]. This method is preferred over other methods as the values of kinetic parameter $K_0$ (defined as the number of attempts made by the nuclei per second to overcome the energy barrier) in addition to $E_c$ can be obtained. The relation used by them is of the form,

$$\ln\left( \beta \middle/ T_c \right) = -E_c \middle/ RT_c + \ln K_0 \tag{2.5}$$

where $K_0$ is the frequency factor. The slope in this relation gives the value of $E_c$.

## 2.6 Thin film deposition

Thin films as a two dimensional system are of great importance. Their material costs are very small as compared to the corresponding bulk material and they perform the same function when it comes to surface processes. Thus, knowledge and determination of the nature, functions and new properties of thin films can be used for the development of new technologies for future applications. Thin films are material layers ranging from fractions of a nanometer to several micrometers in thickness. Electronic semiconductor devices and optical coatings are the main applications benefiting from thin films. Thin film properties are strongly dependent on the method of deposition, the substrate materials, temperature, rate of deposition and composition. Thin films can be deposited by physical methods involving vacuum evaporation and sputtering or by chemical methods involving gas phase and liquid phase depositions. Vacuum evaporation can be achieved by resistive heating, flash evaporation, electron beam evaporation, arc evaporation or by radio frequency (rf) heating.

In the present study, vacuum evaporation technique, employing resistive heating, has been used to deposit the thin films. This method is also known as thermal evaporation. Resistive heating uses a large current passing through the resistor and the target material to be evaporated is put in to the resistor. The resistor generates high temperature and melts the target material. Traditionally, the resistors are made of either Tungsten (*W*), Tantalum (*Ta*) or Molybdenum (*Mo*) which has very high melting temperature. A *Mo* boat has been used in the present study. The resistance of the boat causes it to heat up. The melting temperature of target material is much lower than resistors. When the current passes, only the target material gets melted or vaporized.

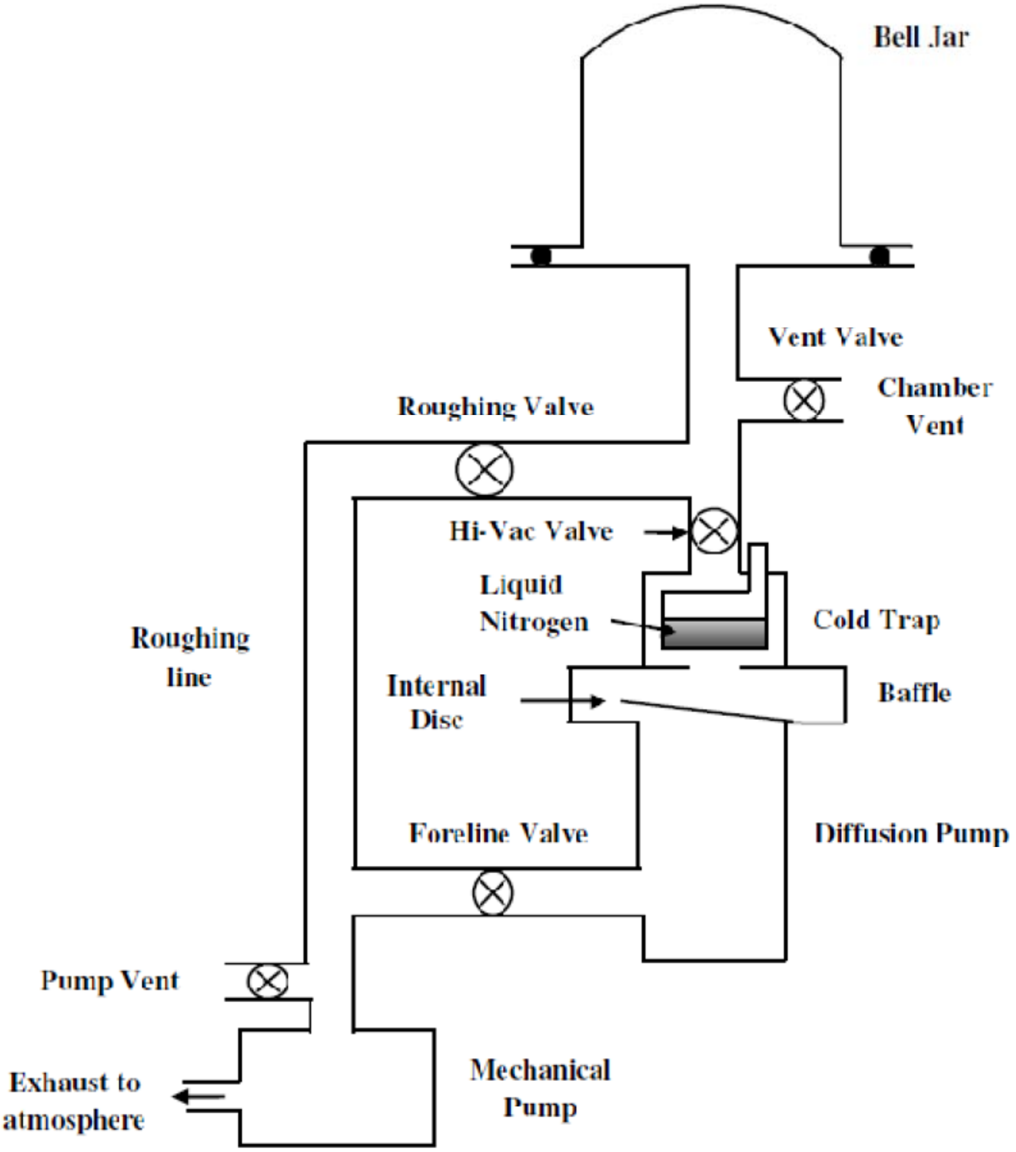

**Figure 2.8** Description of a basic vacuum system.

Prior to the deposition of thin films, substrates have been cleaned thoroughly as thin film readily adheres to a clean insulating surface. Cleaning of the substrate has been done in three steps: (i) soap solution cleaning (ii) cleaning with acetone (vapour cleaning) and (iii) with methanol. Soap solution cleaning basically involves scrubbing the substrate in the soap solution in order to remove any visible oil, grease and dust impurities, then rinsing it thoroughly with double distilled water. This procedure has been repeated 3–4 times for cleaning single substrate. The glass substrates have been sonicated for 15 minutes. Acetone vapour has been used for the removal of organic impurities. For the removal of inorganic impurities, methanol has been used. After all the cleaning, the substrates have been subjected to drying in vacuum oven at a temperature approximately 110 °C and then put into deposition chamber.

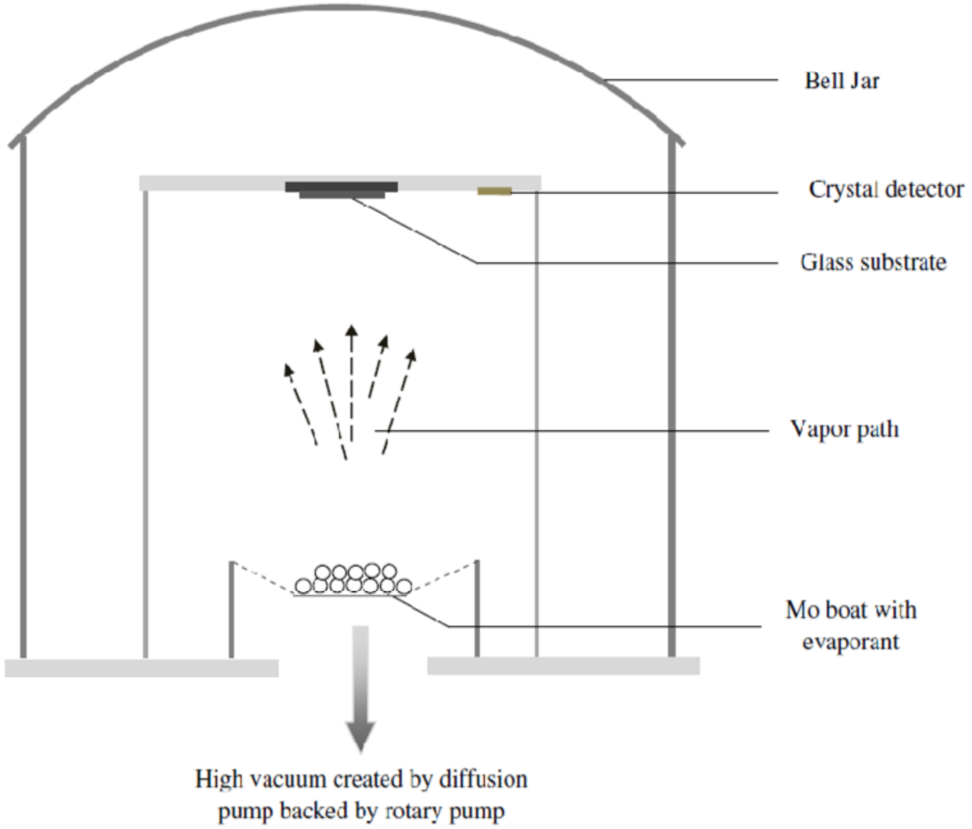

**Figure 2.9** Schematic presentations of components inside the bell jar in a thermal coating unit.

The boat has been cleaned by passing a heavy current through it so as to make it white hot or incandescent for a short while. A shutter has been incorporated in between the source and the substrate so that no vapour stream of the material can reach the substrate directly prior to attaining the required deposition conditions. About 100 mg of finely powdered material has been put in the *Mo* boat. The system has been evacuated to a base pressure of $10^{-4}$ Pa. After establishing the required source temperature, substrate temperature and vacuum in the chamber, the shutter has been removed to start the deposition of film on the cleaned substrate. When the required film thickness has been obtained the shutter was brought back to the original position. Thin films have been kept in the deposition chamber in the dark for 24 h to attain thermodynamic equilibrium as stressed by Abkowitz *et al.* [159]. The vacuum evaporation process has been carried out in a coating system (HINDHIVAC model 12A4D India).

## 2.7 UV–Visible–NIR spectroscopy

A spectrophotometer measures the transmission, reflection or absorbance characteristics of a sample.

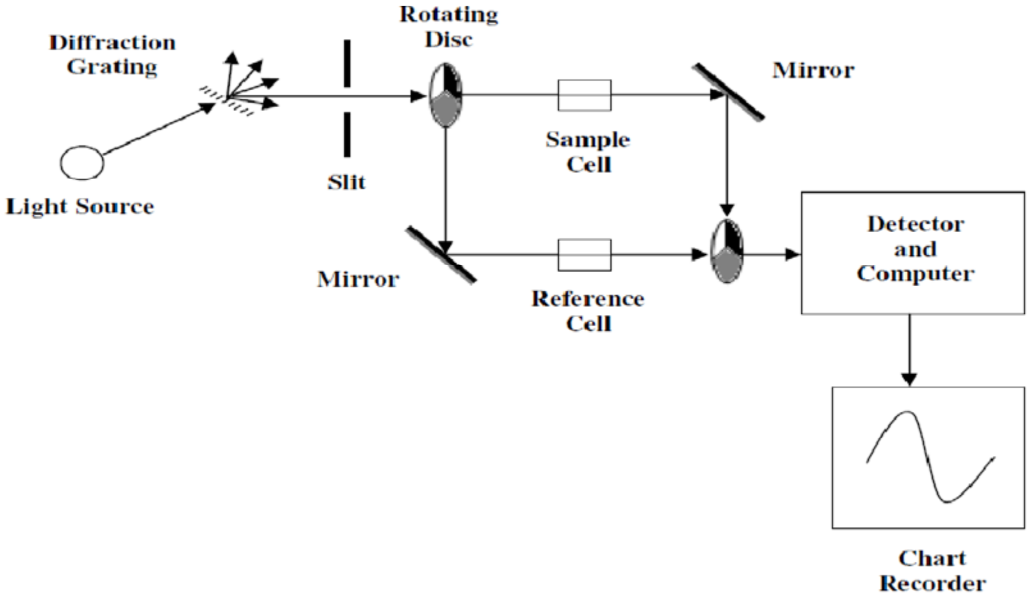

**Figure 2.10** A double beam spectrophotometer.

The respective likelihood of these outcomes depends on the angle of incidence, path length, particle size and absorption coefficient of the material.

Instrument design necessitates that the wavelength of radiation to be studied must be a narrow 'window'. Accordingly, the predetermined electromagnetic radiation wavelengths for ultra–violet (UV), visible (Vis) and near infra–red (NIR) radiation are 10 nm to 390 nm, 390 nm to 780 nm and 780 nm to 3 μm respectively.

A double beam spectrophotometer consists of a light source. The beam from the light source is alternately diverted at right angles by a rotating disk with three distinct panels. One sector allows the beam to pass straight through the disk, another has a mirror surface and the third is black. When the beam passes through the disk it shines directly into the sample cell. When the light is reflected 90° by the rotating disk then it passes through the reference cell. If the light beam falls on the black sector then no light passes through the disk. This part of the cycle is used by the computer to digitize and measure the dark current which is then subtracted from the overall light measurements made by the system. The light after passing through the sample cell and reference cell is directed towards the light detector which converts the incident photons into electrical signal. The mirrors have been placed in the path of light beam in order to collect and collimate the light.

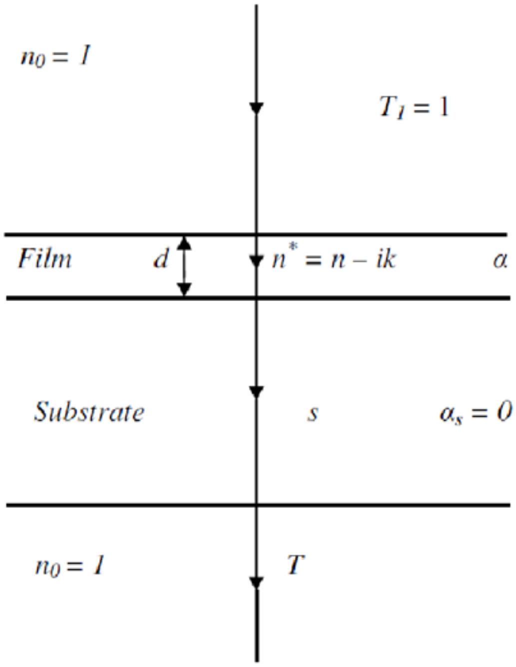

**Figure 2.11** Absorbing film on a thick finite transparent substrate.

Films are ideal specimen for reflectance and transmittance measurements. The transmission spectra of the deposited films in the spectral range 500–2500 nm have been obtained using double beam UV–Vis–NIR (Perkin Elmer Lambda 750) at room temperature (300 K). The spectrophotometer has been set with a slit width of 1 nm. Therefore, it has been unnecessary to make slit width corrections because of a small slit width value in comparison with different line widths [160]. Typical interference fringes have been obtained and the methodology to calculate the optical constants using them has been given below.

Swanepoel proposed a method to determine optical constants *i.e.* refractive index ($n$) and absorption coefficient ($\alpha$) using the transmission spectrum [161]. A representation of absorbing film on a finite transparent substrate is given in Figure 2.11. The thickness of the film is $d$ and its complex refractive index is $n^* = n - ik$, where $k$ is the extinction coefficient. The thickness of the substrate is several orders greater than that of the film and has refractive index $s$ and absorption coefficient $\alpha_s = 0$. The refractive index of the air is $n_0 = 1$.

Figure 2.12 shows the transmission spectrum of an absorbing thin film where the fringes are obtained due to interference of light. These fringes can be used to calculate the optical constants of the film. The transmission spectrum can roughly be divided into four absorption regions: (a) transparent (absorption coefficient, $\alpha \approx 0$) region where transmission is determined by $n$ and $s$ through multiple reflections, (b) weak region where transmission starts to decrease, (c) medium region and (d) strong region where transmission decreases drastically due to the influence of $\alpha$.

In the region of weak and medium absorption, $\alpha \neq 0$ and absorbance ($A$) < 1, Swanepoel suggested of creating upper and lower envelopes of the interference maxima and minima. The refractive index in this region has been calculated using,

$$n = \left[ N + \left( N^2 - s^2 \right)^{1/2} \right]^{1/2} \tag{2.6}$$

where

$$N = 2s \frac{T_{\max} - T_{\min}}{T_{\max} T_{\min}} + \frac{s^2 + 1}{2} \tag{2.7}$$

$T_{max}$ and $T_{min}$ are the transmission maximum and corresponding minimum respectively at a certain wavelength. If $n_{e1}$ and $n_{e2}$ are the refractive indices at two adjacent maxima at wavelengths $\lambda_{e1}$ and $\lambda_{e2}$, then thickness of the thin films can be calculated from the expression [161],

$$d = \frac{\lambda_{e1}\lambda_{e2}}{2\left(\lambda_{e1}n_{e2} - \lambda_{e2}n_{e1}\right)} \tag{2.8}$$

But, the above equation is sensitive to errors in $n$ and is not very accurate. The mean $d$ and $n$ are together used to calculate the order number $m'$ from the basic equation of interference, $2nd = m'\lambda$, to calculate more accurate value of $d$ by taking corresponding integral or half integral values of $m'$. The values of $n$ can be fitted to a two term Cauchy dispersion relation $n = a + b/\lambda^2$, where $a$ and $b$ are Cauchy's constants, and $n$ have been extrapolated to all wavelengths.

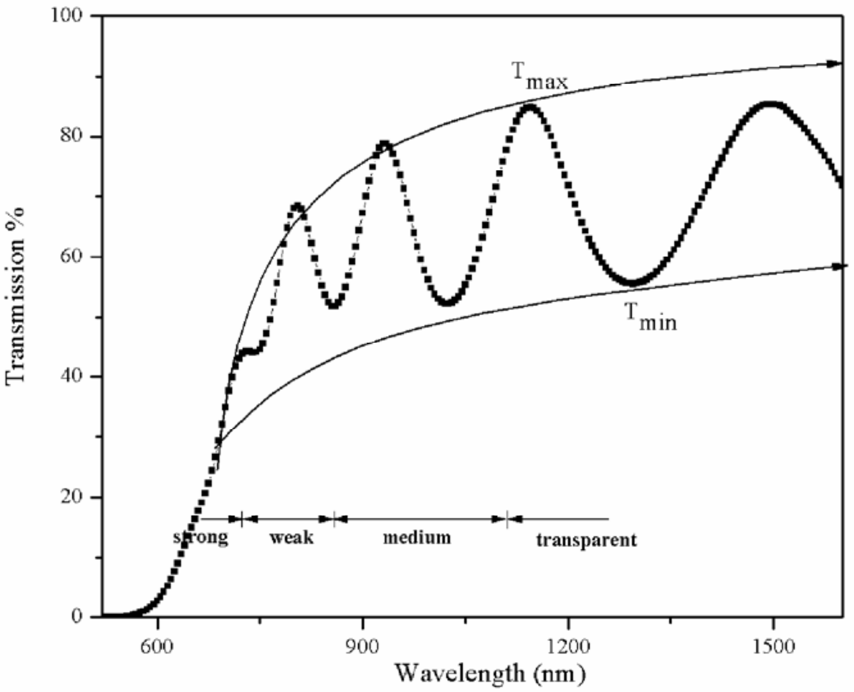

**Figure 2.12** Transmission spectrum of an absorbing thin film on transparent glass substrate.

Once $n$ is known, the absorption coefficient, $\alpha$, can be calculated using the relation [161],

$$\alpha = \frac{1}{d}\ln\left(\frac{1}{A}\right) \tag{2.9}$$

where $A$ is the absorbance given by the relation,

$$A = \frac{E_{\max} - \left[E_{\max}^{2} - \left(n^{2}-1\right)^{3}\left(n^{2}-s^{4}\right)^{1/2}\right]}{\left(n-1\right)^{3}\left(n-s^{2}\right)} \tag{2.10}$$

where $E_{max}$ is maximum energy given by,

$$E_{\max} = \frac{8n^{2}s}{T_{\max}} + \left(n^{2}-1\right)\left(n^{2}-s^{4}\right) \tag{2.11}$$

The extinction coefficient at a particular wavelength can be calculated as [151],

$$k = \frac{\alpha\lambda}{4\pi} \tag{2.12}$$

The optical band gap ($E_g^{opt}$) has been calculated using Tauc's relation [88] as given by equation (1.1). A plot between $(\alpha h\nu)^{0.5}$ and $h\nu$ has been plotted. The value of $E_g^{opt}$ has been obtained by extrapolating the absorption edge to the energy axis.

The spectral dependence of the refractive index can be fitted to the single oscillator *i.e.* Wemple–DiDomenico model [162]. It suggests a relation between refractive index and single oscillator strength, below the fundamental absorption edge,

$$n^{2}(h\nu) = 1 + \frac{E_{0}E_{d}}{E_{0}^{2} - (h\nu)^{2}} \tag{2.13}$$

where $E_0$ is the oscillator energy indicating the mean transition energy and $E_d$, the oscillator strength, is the measure of strength of interband optical transitions respectively. The dispersion energy or oscillator strength ($E_d$) also follows a simple empirical relation,

$$E_d = \beta' N_c Z_a N_e \tag{2.14}$$

where $\beta'$ is a two valued constant. According to Wemple, for covalent crystalline and amorphous materials, $\beta'$ has a value of 0.37 ± 0.04 eV and 0.26 ± 0.03 eV for ionic materials. $N_c$ is the coordination number of the cation nearest neighbor to the anion, $Z_a = 2$ is the formal chemical valency of the anion and $N_e$ is the total number of valence electrons per anion.

The complex dielectric constant,

$$\varepsilon = \varepsilon_r + i\varepsilon_i \tag{2.15}$$

where $\varepsilon_r$ is the real part representing the dielectric constant or relative permittivity and is a measure of polarizability of a material and $\varepsilon_i$ is the imaginary part of the dielectric constant indicating the energy loss *i.e.* the energy lost in aligning the dipoles. The loss tangent,

$$tan\delta = \varepsilon_i/\varepsilon_r \qquad (2.16)$$

where $\delta$ is the loss angle, measures the inherent dissipation of energy of a dielectric material. The values of $\varepsilon_r$ and $\varepsilon_i$ can be calculated using [98],

$$\varepsilon_r = n^2 - k^2 \qquad (2.17)$$

and

$$\varepsilon_i = 2nk \qquad (2.18)$$

Optical conductivity ($\sigma$) is directly related to the dielectric loss *i.e.* $\varepsilon_i$ ($\varepsilon_i = \sigma(\omega)/\omega\varepsilon_0$) and tells about the electronic structure of a system. It has dimensions of frequency which is valid only in Gaussian system of units. The optical conductivity can be determined using relation [163],

$$\sigma = \frac{\alpha nc}{4\pi} \qquad (2.19)$$

where $c$ is the velocity of light.

**Acknowledgements**

Thanks are due to RSIC, Panjab University for providing XRD and FTIR facilities, and Indian Institute of Technology, Roorkee for providing DTA facility.

# CHAPTER 3

# Physical and structural properties of *Sb–Se–Ge* and *Sb–Se–Ge–In* systems

- **Sunanda Sharda,** Neha Sharma, Pankaj Sharma and Vineet Sharma, "Finger prints of chemical bonds in Sb-Se-Ge and Sb-Se-Ge-In glasses: A far-IR study" **Journal of Non Crystalline Solids**, 362 (2013) 136-139.

- **Sunanda Sharda**, Neha Sharma, Pankaj Sharma and Vineet Sharma, "Basic physical analysis of new *Sb-Se-Ge-In* chalcogenide glassy alloys by predicting structural units: A theoretical approach" **Chalcogenide Letters**, 9 (2012) 389-395.

- **Sunanda Sharda**, Neha Sharma, Pankaj Sharma and Vineet Sharma, "Physical Analysis of Structural Transformation in Ge-Incorporated a-$Sb_xSe_{100-x}$ System" **Defect and Diffusion Forum**, 316-317 (2011) 45-53.

In this chapter, the physical and structural properties of $Sb_{10}Se_{90-x}Ge_x$ and $Sb_{10}Se_{65}Ge_{25-y}In_y$ systems have been discussed. The effect of $Ge$ addition on $Sb_{10}Se_{90}$ and $In$ alloying on $Sb_{10}Se_{65}Ge_{25}$ have been investigated with respect to their physical and structural properties.

## 3.1 Introduction

Low transmission losses, semiconducting behaviour and phase change properties of chalcogenides make them attractive candidates to be used in all–optical devices [164], conducting chalcogenide glass sensors [165] and phase change memory devices [166] etc. These glasses have wide transparency range in the IR region making them the material of choice for technological developments like microstructured fibers [167], relief fibers [168] or planar waveguides [169]. The evaluation of physical parameters is important to explore best characteristics of a system suitable for practical and scientific applications. Theoretical calculations can predict the stability of a glass system to a great extent thus, making it easier for the selection and solution of the problem without performing experiment. The bonding state between the constituent elements varies with the composition ratio. The knowledge of bonding arrangement of the system helps in predicting the experimental properties. From infrared (IR) spectroscopic studies of the amorphous alloys the concentration of different structural units can be predicted in an alloy.

The structure of chalcogenide glasses is generally described as a network of covalent bonds obeying the 8 - N rule [170]. An amorphous material is described by its short range order. The important aspects of short range order are the number and type of immediate neighbors and their spatial arrangement about a given reference atom. The short range order can be described by three parameters, the number of bonds, the bond length, and the bond angle as these parameters have well defined values in a narrow range. Based on these parameters Philips and Thorpe [64] have developed a rigidity percolation theory which compares the bond stretching and bending constraints with the number of degrees of freedom and predicted that a structural threshold is reached for the average coordination number $\langle m \rangle = 2.4$.

There is a considerable interest in interpreting the electronic and vibrational spectra of amorphous semiconductors in terms of chemical bonding [171]. For understanding their structural properties, infrared (IR) spectroscopy and Raman spectroscopy are useful tools. Vibrations modulating the molecular dipole moments are visible in the IR spectrum, while those modulating the polarizability appear in the Raman spectrum. From IR spectroscopic studies of amorphous alloys, it is known that the bonding state between the constituent elements varies with the composition ratio of the elements and the concentration of different structural units present in the alloy [172].

Ambika *et al.* [173] have theoretically analyzed the physical parameters of *Ge–Te–Bi* glassy system. The values of *m*, mean bond energy and cohesive energy increased with increasing *Bi* content. George *et al.* [174] have studied the influence of *In* additive on physical properties of $As_{40}Te_{60-x}In_x$ glasses. The average coordination number, optical gap, average heat of atomization and mean bond energy increased with increasing the *In* content. El-Sayed [175] has carried out far-infrared studies of $Sb_xGe_{28-x}Se_{72}$ and has also calculated physical parameters for the system. The average coordination number and mean bond energy decreased with increase in *Sb* content. In the IR spectra broad band at 220 $cm^{-1}$ and 225 $cm^{-1}$ was reported corresponding to the *Ge–Se* bonds. *Se* in the form of polymeric chain and rings was reported at 227 $cm^{-1}$ and 247 $cm^{-1}$.

This chapter deals with the calculation of various physical parameters like average coordination number (*m*), density ($\rho$), compactness ($\delta$), glass transition temperature ($T_g$) and number of lone pair electrons (*L*). The distribution of chemical bonds has been calculated which has further been correlated to the far-IR results. X–ray diffraction and compositional analysis has also been performed on the samples.

## 3.2 Experimental details

Bulk samples of $Sb_{10}Se_{90-x}Ge_x$ ($x$ = 0, 19, 21, 23, 25, 27) and $Sb_{10}Se_{65}Ge_{25-y}In_y$ ($y$ = 0, 3, 6, 9, 12, 15) have been prepared using melt quenching technique. Constituent elements have been weighed in their respective at.% and sealed in evacuated quartz ampoules. The ampoules have been placed in a furnace and rocked frequently for the homogenization of the melt for 24 h. Quenching of the ampoules has been done in ice cold water. The quenched ampoules have been placed in a solution of *HF* and $H_2O_2$. Samples have been obtained by breaking the ampoules and ground to fine powder using mortar and pestle. The bulk samples have been analyzed for their composition using EDX and amorphous nature by using XRD.

The far-IR transmission spectra of the alloys have been recorded using Fourier Transform infrared spectrophotometer (Perkin Elmer - Spectrum RX-IFTIR) from 50 to 350 cm$^{-1}$. The resolution has been set at 1 cm$^{-1}$. Measurements have been made using the polyethylene pellet (13 mm diameter) method. The pallets have been made by mixing 2 mg sample with 200 mg of spectroscopic grade polyethylene and pressed into pallets. To take account of the polyethylene absorption, the polyethylene spectrum has been taken as reference.

## 3.3 Results and discussion

The amorphous state of the alloys has been confirmed by the absence of sharp peaks in the x–ray diffraction patterns (Figure 3.1 and Figure 3.2).

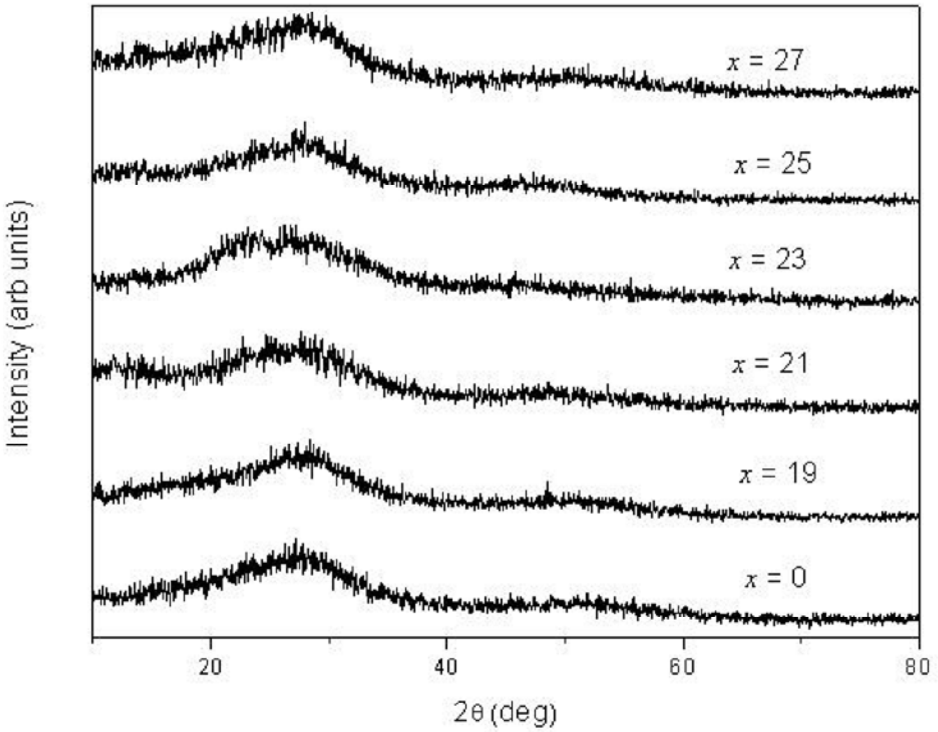

**Figure 3.1** XRD spectra of $Sb_{10}Se_{90-x}Ge_x$ system.

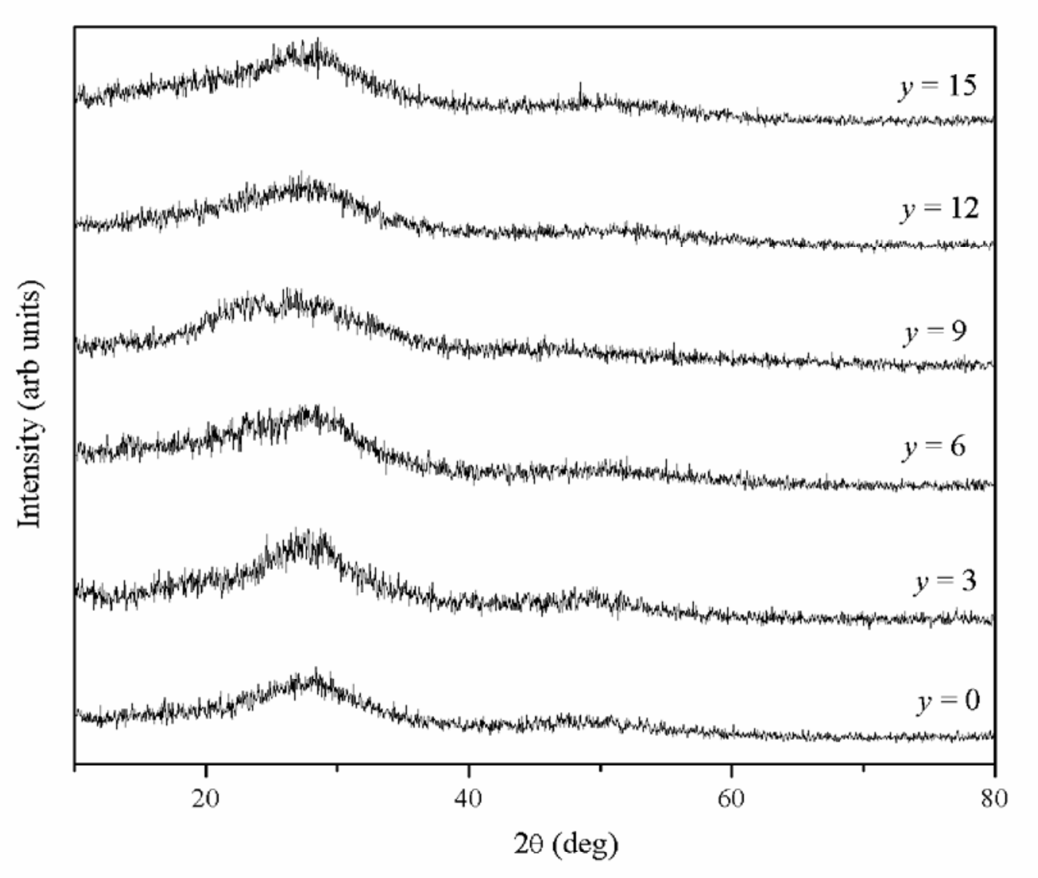

**Figure 3.2** XRD spectra of $Sb_{10}Se_{65}Ge_{25-y}In_y$ system.

EDX indicates that the atomic mass percentages of the constituent elements are close to their starting elements (Table 1).

**Table 3.1** Elemental composition for $Sb_{10}Se_{90-x}Ge_x$ ($x$ = 0, 19, 21, 23, 25, 27) and $Sb_{10}Se_{65}Ge_{25-y}In_y$ ($y$ = 0, 3, 6, 9, 12, 15) systems.

| ***x*** | ***Sb*** | ***Se*** | ***Ge*** | ***y*** | ***Sb*** | ***Se*** | *Ge* | ***In*** |
|---|---|---|---|---|---|---|---|---|
| 0 | 10.83 | 89.17 | 0 | 0 | 10.37 | 64.13 | 25.50 | 0 |
| 19 | 9.86 | 71.56 | 18.58 | 3 | 10.22 | 64.57 | 22.36 | 2.85 |
| 21 | 9.96 | 69.84 | 20.20 | 6 | 9.87 | 65.46 | 18.43 | 6.24 |
| 23 | 10.10 | 67.73 | 22.17 | 9 | 9.73 | 64.31 | 16.58 | 9.38 |
| 25 | 10.37 | 64.13 | 25.50 | 12 | 10.34 | 65.56 | 12.39 | 11.71 |
| 27 | 10.41 | 61.85 | 27.74 | 15 | 10.45 | 64.81 | 9.25 | 15.49 |

### 3.3.1 Physical properties of *Sb–Se–Ge* system

Average coordination number is a measure of crosslinking in a covalent bonded glass system. For the system $Sb_{10}Se_{90-x}Ge_x$ average coordination number ($m$) has been calculated using the formula [63]:

$$m = \frac{\gamma N_{Sb} + \varphi N_{Se} + \kappa N_{Ge}}{100} \tag{3.1}$$

where $\gamma$, $\varphi$ and $\kappa$ are the at.%, and $N_{Sb}$, $N_{Se}$ and $N_{Ge}$ are the coordination numbers of *Sb*, *Se* and *Ge* respectively.

For a given value of $m$, two types of constraints [176, 177] exist in the system, first is the bond stretching constraint ($N_a$) and the second is bond bending constraint ($N_b$). For $m$-coordinated system, $N_a = m/2$ and $N_b = 2m\text{-}3$. The total number of constraints per atom ($N_t$) is then equal to the sum of bond bending and bond stretching constraints. Phillips and Thorpe [63] suggested that the optimized condition for glass formation exists when $N_t$ equals the number of degrees of freedom ($N_d$) *i.e.* when $N_t = N_d = 3$. At this point $m$ was suggested to be 2.4 for binary systems for which there is a transition from floppy to rigid mode. The calculated values of $m$ are given in Table 3.2 and it varies from 2.10 to 2.64 as *Ge* concentration increases at the cost of *Se* concentration.

**Table 3.2** Values of average coordination number ($m$), bond stretching constraint ($N_a$), bond bending constraint ($N_b$), total number of constraints per atom ($N_t$), density ($\rho$), molar volume ($V_m$), compactness ($\delta$) and glass transition temperature ($T_g$) for $Sb_{10}Se_{90-x}Ge_x$ system.

| $x$ | $m$ | $N_a$ | $N_b$ | $N_t$ | $\rho$ (g/cm$^3$) | $V_m$ ($cm^3 mol^{-1}$) | $\delta$ | $T_g$ ($K$) |
|---|---|---|---|---|---|---|---|---|
| 0 | 2.10 | 1.05 | 1.20 | 2.25 | 4.98 | 16.72 | -0.003547 | 321.98 |
| 19 | 2.48 | 1.24 | 1.96 | 3.20 | 5.08 | 16.15 | -0.001792 | 490.87 |
| 21 | 2.52 | 1.26 | 2.04 | 3.30 | 5.09 | 16.09 | -0.001682 | 514.57 |
| 23 | 2.56 | 1.28 | 2.12 | 3.40 | 5.10 | 16.03 | -0.001586 | 539.20 |
| 25 | 2.60 | 1.30 | 2.20 | 3.50 | 5.11 | 15.97 | -0.001505 | 564.71 |
| 27 | 2.64 | 1.32 | 2.28 | 3.60 | 5.12 | 15.91 | -0.001439 | 560.70 |

Addition of 10 at.% *Sb* to *Se* may form $Sb_2Se_3$ type of structural units which increase the rigidity, but, still the system lies in floppy mode as $m < 2.4$. Further, with the addition of 19 at. % *Ge* to $Sb_{10}Se_{90}$ there is an abrupt change in $m$ value from 2.10 to 2.48. On further addition of *Ge*, $m$ increases gradually. This is because as *Ge* replaces *Se*, the chain structure of *Se* is reduced by the formation of $Ge(Se_{1/2})_4$ three dimensional units, thereby increasing the rigidity of structure. According to Phillips and Thorpe [64], at $m = 2.4$ there is rigidity percolation and transition from 2-dimensional structural network to 3-dimensional structural network takes place. These results on the addition of *Ge* to $Sb_{10}Se_{90}$, are in agreement with the results suggested by Phillips [63]. Moreover, the values of $N_t > 3$ (Table 3.2) confirm that the system makes a transition from floppy to rigid mode on the addition of *Ge*.

The density ($\rho$) for the $Sb_{10}Se_{90-x}Ge_x$ glass system has been calculated using the relation [178]:

$$\rho = \left( \sum_i \frac{m_i}{d_i} \right)^{-1} \tag{3.2}$$

where $m_i$ is the fraction of mass and $d_i$ is the density of $i^{th}$ structural unit. Density is directly related to the rigidity of the system, *i.e.*, it is related to the average coordination number of the system. The calculated density values for the above system (Table 3.2) are increasing with increasing *Ge* content. This is because *Se* is being substituted by denser *Ge* atom and also as $m > 2.4$ the system has become rigid and thus getting denser.

Using above calculated values, the molar volume ($V_m$) for the $Sb_{10}Se_{90-x}Ge_x$ glass system has been calculated using the formula:

$$V_m = \frac{\sum x_i M_i}{\rho} \tag{3.3}$$

where $x_i$ is the atomic fraction of $i^{th}$ element and $M_i$ is the molecular weight of the $i^{th}$ component in the sample. The calculated molar volume is decreasing with *Ge* content for the system as given in Table 3.2. This is in accordance with relation between $V_m$ and $\rho$ *i.e.* equation (3.3). Also *Se* is being substituted by smaller *Ge* atom leading to decrease in molar volume with increase in *Ge* concentration. Another parameter evaluated using the above calculated two parameters ($\rho$ and $V_m$) is the compactness of the system.

Compactness ($\delta$) is a measure of the normalized change of the mean atomic volume due to chemical interaction of the elements forming the network of a given solid [179]. The value of $\delta$ has been calculated using the relation [180, 179]:

$$\delta = \frac{\left( \sum_i \frac{C_i W_i}{\rho_i} - \sum_i \frac{C_i W_i}{\rho} \right)}{\sum_i \frac{C_i W_i}{\rho}} \tag{3.4}$$

where $C_i$ is the atomic fraction, $W_i$ is the atomic weight, $\rho_i$ is the atomic density of the $i^{th}$ element of the glass and $\rho$ is the density of the glass. For the system $Sb_{10}Se_{90-x}Ge_x$ the variation in the compactness has been defined in terms of change in the structure of the glass network in comparison to the mean atomic volume. The compactness for this system increases with the addition of $Ge$ to it (Table 3.2). This behaviour may also be attributed to the fact that as $Ge$ concentration increases, the density of the system also increases and hence, the rigidity. As a result, the system becomes more compact.

Parameter R indicates the deviation in stoichiometry and for the system $Sb_{10}Se_{90-x}Ge_x$, it is defined as the ratio of covalent bonding possibilities of chalcogen atom ($Se$) to the non-chalcogen atoms ($Sb$ and $Ge$) [66]:

$$\mathrm{R} = \frac{G N_{Se}}{\left( H N_{Ge} + F N_{Sb} \right)} \tag{3.5}$$

where $F$, $G$, $H$ are the atomic fractions and $N_{Sb} = 3$, $N_{Se} = 2$, $N_{Ge} = 4$ are the coordination numbers of $Sb$, $Se$ and $Ge$ respectively. From Figure 3.3, which gives the variation of R with $Ge$ content, the $Sb_{10}Se_{90-x}Ge_x$ system has been divided into three parts:

(i) R = 1: $Sb_{10}Se_{65}Ge_{25}$ is the stoichiometric composition as this composition consists of structural units of the type trigonal $Sb_2Se_3$ and tetrahedral $Ge(Se_{1/2})_4$ only and $Sb_{10}Se_{65}Ge_{25}$ can be written as $(GeSe_2)_{25}(Sb_2Se_3)_5$. This signifies that a full 3-dimensional network between the two structural units is attained.

(ii) R > 1: $Sb_{10}Se_{90-x}Ge_x$ for $x$ = 19, 21, 23 (at.% of $Ge$ < 25) systems are $Se$ rich glasses [183] as these compositions contain $Se–Se$ bonds in addition to $Sb_2Se_3$ and $Ge(Se_{1/2})_4$ units.

(iii) R < 1: $Sb_{10}Se_{63}Ge_{27}$ (at.% of $Ge$ > 25) is the $Ge$ rich [182] composition as it contains $Ge–Ge$ bonds in addition to $Sb_2Se_3$ and $Ge(Se_{1/2})_4$ units.

Glass transition temperature ($T_g$) may be regarded as a point, where a transition occurs and below which supercooled liquid becomes glass. Tichy and Ticha [66, 179] proposed that $T_g$ is proportional to some overall mean bond energy which is the averaged value of dissociation energy of the bonds and is a function of average coordination number, types of bonds, degree of crosslinking in a system and bond energy of formation of a network. Mean bond energy ($<E>$) for the system $Sb_FSe_GGe_H$ (where $F + G + H = 1$) has been calculated using the formula [66]:

$$\langle E\rangle = E_c + E_{rm} \tag{3.6}$$

where $E_c$ is the mean bond energy of the average cross linking per atom given by:

for R > 1

$$\langle E_c\rangle = 4HE_{Ge-Se} + 3FE_{Sb-Se} \tag{3.7}$$

and for R < 1

$$\langle E_c\rangle = \frac{2G(4HE_{Ge-Se} + 3FE_{Sb-Se})}{(4H + 3F)} \tag{3.8}$$

and $E_{rm}$ is the average bond energy per atom of remaining matrix given by:

for R > 1

$$E_{rm} = \frac{(2G - 4H - 3F)E_{Se-Se}}{m} \tag{3.9}$$

for R < 1

$$E_{rm} = \frac{(4H + 3F - 2G)E_{\langle\rangle}}{m} \tag{3.10}$$

where

$$E_{\langle\rangle} = \frac{E_{Ge-Ge} + E_{Sb-Sb} + E_{Ge-Sb}}{3} \tag{3.11}$$

denotes the average bond energy of metal-metal bond for R < 1. $E_{Ge–Se}$, $E_{Sb–Se}$, $E_{Se–Se}$, $E_{Ge–Ge}$, $E_{Sb–Sb}$ and $E_{Ge–Sb}$ are bond energies of $Ge–Se$, $Sb–Se$, $Se–Se$, $Ge–Ge$, $Sb–Sb$

and *Ge–Sb* bonds respectively. Tichy and Ticha established a relation between <*E*> and $T_g$ in the form [66],

$$T_g = 311[\langle E \rangle - 0.9] \tag{3.12}$$

Figure 3.3 and Table 3.2 indicates that with the addition of *Ge* to $Sb_{10}Se_{90}$, the mean bond energy and glass transition temperature increases. This is because, $Sb_{10}Se_{90}$ contain only $Sb_2Se_3$ structural units which have weak *Sb–Se* bonds. But, with the addition of *Ge*, *Sb–Se* bonds are being replaced by stronger *Ge–Se* bonds resulting in the formation of tetrahedral $Ge(Se_{1/2})_4$ units. For $Sb_{10}Se_{90-x}Ge_x$ system, the calculated values of R and <*E*> have been plotted against increasing *Ge* content (Figure 3.3).

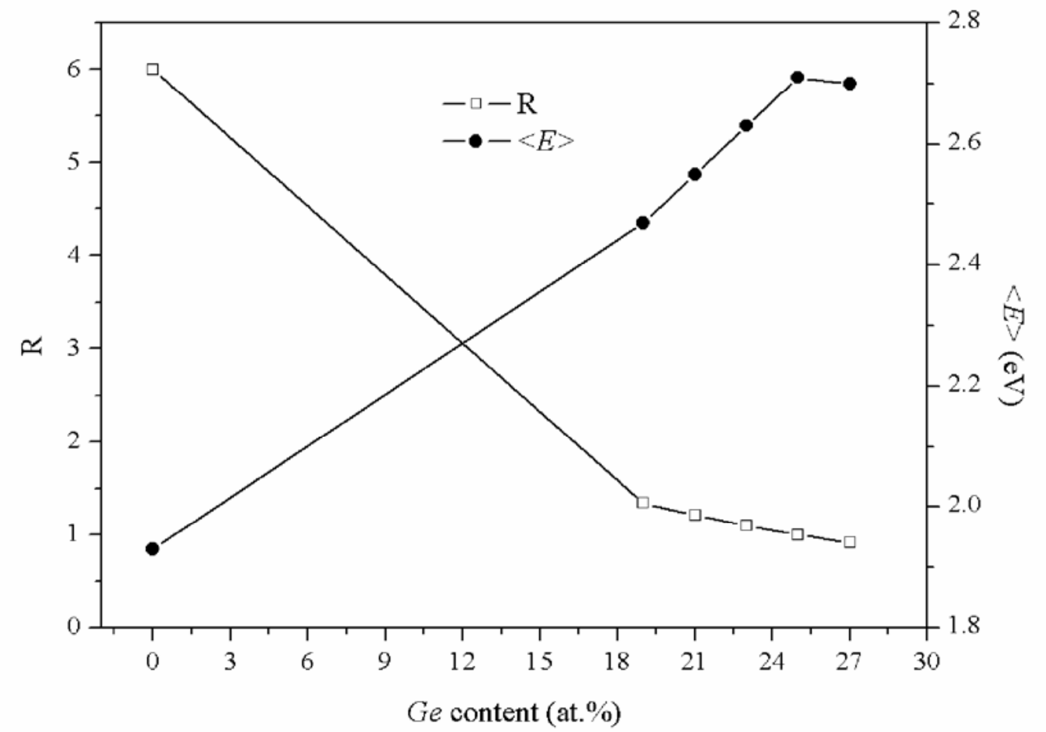

**Figure 3.3** Variation of parameter R and mean bond energy (<*E*>) with increasing *Ge* content for $Sb_{10}Se_{90-x}Ge_x$ system.

There is a sharp increase in <*E*> value with the addition of 19 at.% *Ge* to $Sb_{10}Se_{90}$ system from 1.93 eV to 2.47 eV because of the rigidity percolation at $m = 2.4$. There is a maximum for <*E*> at R = 1 *i.e.*, at $x = 25$ at.% of *Ge* addition, the stoichiometric composition is obtained, because this composition contains only the heteropolar *Sb–Se* and *Ge–Se* bonds. Above and below this composition, the value of mean bond energy, <*E*>, decreases, since above and below this composition $Sb_2Se_3$ and $GeSe_2$ units are being replaced by weaker *Se–Se* and *Ge–Ge* bonds respectively. Now, as <*E*> and $T_g$ are directly related to each other, similar variations in $T_g$, as that for <*E*> have been observed as evident from Table 3.2.

The cohesive energies, *i.e.*, the energy needed to break a solid apart into respective neutral free atoms, have been calculated using the Chemical Bond Approach (CBA) [183]. In view of this approach, atoms of one type combine more favorably with atoms of different types and the bonds are formed in the sequence of decreasing bond energy until all the available valences of the atom are filled. The bond energies of heteropolar bond ($E_{A–B}$) have been calculated using the Pauling relation [184]:

$$E_{A-B} = \left(E_{A-A} \times E_{B-B}\right)^{0.5} + 30(\chi_A - \chi_B)^2 \qquad (3.13)$$

where $E_{A–A}$ and $E_{B–B}$ are the homopolar bond energies and $\chi_A$ and $\chi_B$ are corresponding electronegativities.

**Table 3.3** Bond distribution, cohesive energies (*CE*) and bond energies (*BE*) for $Sb_{10}Se_{90-x}Ge_x$ system.

| *x* | Bond distribution<br>*Ge–Se* | <br>*Sb–Se* | <br>*Se–Se* | <br>*Ge–Ge* | *CE* (kcal/mol) | *Bonds* | *BE* (kcal/mol) |
|---|---|---|---|---|---|---|---|
| 0 | - | 0.1667 | 0.8333 | - | 43.99 | *Ge-Se* | 49.42 |
| 19 | 0.5352 | 0.2113 | 0.2535 | - | 46.89 | *Se-Se* | 44.00 |
| 21 | 0.6087 | 0.2174 | 0.1739 | - | 47.29 | *Sb-Se* | 43.96 |
| 23 | 0.6866 | 0.2239 | 0.0895 | - | 47.72 | *Ge-Ge* | 37.60 |
| 25 | 0.7692 | 0.2308 | - | - | 48.16 | *Ge-Sb* | 33.76 |
| 27 | 0.2084 | 0.2381 | - | 0.4815 | 47.99 | *Sb-Sb* | 30.22 |

Assuming the bond energies to be additive, the cohesive energy (*CE*) has been calculated using the relation

$$CE = \sum_i C_i E_i \tag{3.14}$$

where $C_i$ is the distribution of the chemical bonds and $E_i$ is the energy associated with the corresponding bond. *CE* along with the bond energies and distribution of chemical bonds are listed in Table 3.3.

The results indicate that the *CE* increases with increasing *Ge* content, attains maximum at $x = 25$, and then decreases. The variation of cohesive energy has been explained on the basis of chemical bond ordering. In $Sb_{10}Se_{65}Ge_{25}$ composition, only *Ge–Se* and *Sb–Se* bonds exist which have maximum bond energies and have priority over the formation of homopolar bonds according to CBA. Hence, the *CE* value has a maximum at $x = 25$. For compositions with $x < 25$, there exist homopolar *Se–Se* bonds having bond energy 44 kcal/mol and for the composition with $x > 25$, there exist homopolar *Ge–Ge* bonds having bond energy 37.60 kcal/mol. So, *CE* decreases above and below $Sb_{10}Se_{65}Ge_{25}$ composition.

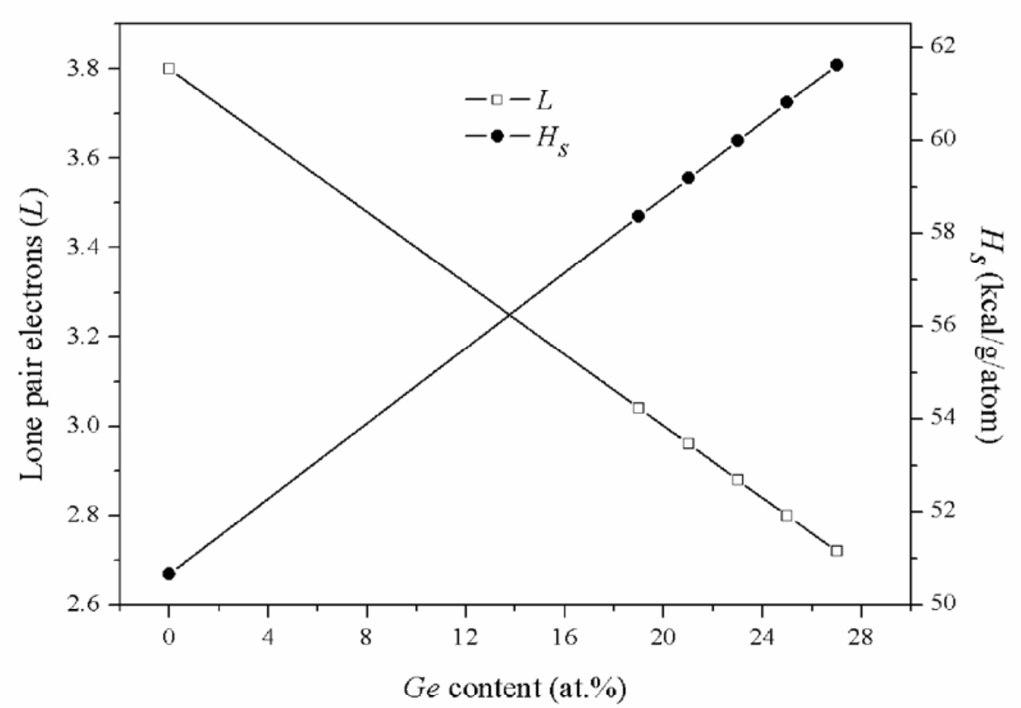

**Figure 3.4** Variation of lone pair electrons (*L*) and average heat of atomization ($H_s$) with increasing *Ge* content for $Sb_{10}Se_{90-x}Ge_x$ system.

For the ternary system $Sb_{\gamma}Se_{\varphi}Ge_{\kappa}$, the average heat of atomization $H_s$ (kcal/g/atom) is defined as [185]:

$$H_s = \frac{\gamma H_s^{Sb} + \varphi H_s^{Se} + \kappa H_s^{Ge}}{\gamma + \varphi + \kappa} \tag{3.16}$$

where $\gamma$, $\varphi$, $\kappa$ are the at.% of *Sb*, *Se* and *Ge* and $H_s$ values for *Sb*, *Se* and *Ge* are 62.0, 49.4 and 90.0 kcal/g/atom respectively [186]. The variation of $H_s$ with increasing *Ge* content has been plotted in Figure 3.4.

The average single bond energy ($H_s/m$) specifies the bond strength. The average single bond energies decrease with increase in *Ge* content (Figure 3.5), which indicates that the bond strength decreases. The electronegativity values ($\chi$) give an idea about the ionicity of the system and have been calculated using Sanderson Principle [187]. The electronegativity values of *Sb*, *Se* and *Ge* are 2.05, 2.55 and 2.01 respectively [188]. As *Ge* is less electronegative than *Se* therefore, the replacement of *Se* by electropositive *Ge* atom leads to a decrease in the $\chi$ values (Figure 3.5).

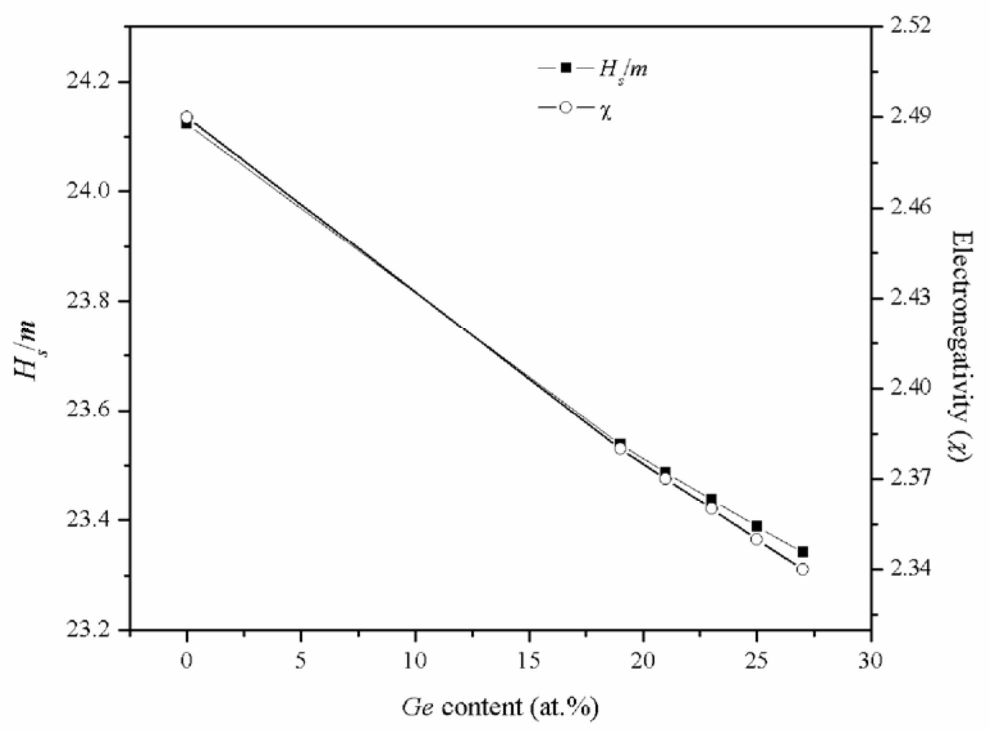

**Figure 3.5** Average single bond energy ($H_s/m$) and electronegativity ($\chi$) variation with increasing *Ge* content for $Sb_{10}Se_{90-x}Ge_x$ system.

The number of lone pair electrons (*L*) has been calculated using the formula [65]:

$$L = V - m \tag{3.17}$$

where *V* are the valence electrons. For a binary system $L > 2.62$ and for a ternary system $L > 1$ [189]. As *Se* has higher electronegativity value than *Ge*, so *Se* acts as an anion and *Ge* as a cation in *Ge–Se* bond. With the addition of *Ge* to the base system $Sb_{10}Se_{90}$ , the $Ge^{4+}$ interacts with the lone pair of more electronegative *Se* atom to form the tetrahedral structural unit $(GeSe_{1/2})_4$. The glass forming tendency of the ternary glass system decreases with increasing content of *Ge* as shown in Figure 3.4. This is due to the interaction of *Ge* with the lone pair of bridging *Se* atom in the glass system. The base composition $Sb_{10}Se_{90}$ has $L = 3.8$, but with the addition of *Ge*, there is a sharp decrease in *L* value. This shows that in order to attain structural stability, availability of lone pairs is a necessary condition. Lone pair of electrons gives an idea of good glass forming system under investigation as values of *L* are much larger than 1 [189].

### 3.3.2 Physical properties of *Sb–Se–Ge–In* system

The study of physical properties of $Sb_{10}Se_{90-x}Ge_x$ indicates that for $x = 25$ at.% of *Ge* is a stable composition. The effect of *In* addition at the cost of *Ge* has been studied to explore the variation in properties of $Sb_{10}Se_{65}Ge_{25}$ composition. Due to large electronegativity difference between *Ge* and *In*, there is a possibility of increase in the glass forming region. This may also bring configurational and conformal changes in the base system.

For the system $Sb_{10}Se_{65}Ge_{25-y}In_y$ average coordination number (*m*) has been calculated using the formula [63],

$$m = \frac{\gamma N_{Sb} + \varphi N_{Se} + \kappa N_{Ge} + \psi N_{In}}{100} \tag{3.18}$$

where $\gamma$, $\varphi$, $\kappa$ and $\psi$ are the at.% and $N_{Sb}$, $N_{Se}$, $N_{Ge}$ and $N_{In}$ are the coordination numbers of *Sb*, *Se*, *Ge* and *In* respectively. Determination of *m* allows the calculation of the total number of constraints, $N_t = N_a + N_b$. For $y = 0$ the value of $m = 2.60$ and $N_t = 3.50$ indicates that the system is stressed rigid and over constrained (Table 3.4). But, with increasing *In* concentration value of *m* decreases to 2.45 and that of $N_t$ decreases to 3.125 for $y = 15$. So, there is a decrease in the crosslinking of the system making the system less constrained which is due to the fact that more threefold coordinated *In* atoms are replacing fourfold coordinated *Ge* atoms as the *In* concentration increases.

The density ($\rho$) for the $Sb_{10}Se_{65}Ge_{25-y}In_y$ glass system has been calculated using equation (3.2). The density of the system increases on *Ge* substitution by *In* atoms (Table 3.4). As the structural modifications take place, higher density *In* atoms replace low density *Ge* atoms. Thus, the density of the system increases for each composition with increase in *In* at.%. The molar volume ($V_m$) of the glassy system has been calculated using equation (3.3). The values of $V_m$ (Table 3.4) increase with *In* content from $y = 0$ to $y = 15$. This may be attributed to the fact that *Ge* is being substituted by larger *In* atoms leading to an increase in $V_m$ with *In* content. Compactness ($\delta$) has been calculated using the equation (3.4). The compactness for the system increases with the *In* addition (Table 3.4). The density of the system increases with increasing *In* content. This leads to an increase in the compactness of the system.

**Table 3.4** Values of average coordination number ($m$), bond stretching constraint ($N_a$), bond bending constraint ($N_b$), total number of constraints per atom ($N_t$), density ($\rho$), molar volume ($V_m$), compactness ($\delta$) and glass transition temperature ($T_g$) for $Sb_{10}Se_{65}Ge_{25-y}In_y$ system.

| $y$ | $m$ | $N_a$ | $N_b$ | $N_t$ | $\rho$ (g/cm$^3$) | $V_m$ ($cm^3mol^{-1}$) | $\delta$ | $T_g$ ($K$) |
|---|---|---|---|---|---|---|---|---|
| 0 | 2.60 | 1.30 | 2.20 | 3.50 | 5.11 | 15.97 | -0.001505 | 639.06 |
| 3 | 2.57 | 1.285 | 2.14 | 3.425 | 5.17 | 16.03 | -0.001421 | 609.11 |
| 6 | 2.54 | 1.27 | 2.08 | 3.35 | 5.23 | 16.09 | -0.001252 | 580.56 |
| 9 | 2.51 | 1.255 | 2.02 | 3.275 | 5.29 | 16.14 | -0.001002 | 553.36 |
| 12 | 2.48 | 1.24 | 1.96 | 3.20 | 5.35 | 16.20 | -0.000674 | 527.42 |
| 15 | 2.45 | 1.225 | 1.90 | 3.125 | 5.41 | 16.26 | -0.000272 | 502.70 |

Parameter R for quaternary system has been calculated as the ratio of covalent bonding possibilities of chalcogen atom (*Se*) to the non–chalcogen atoms (*Sb*, *Ge* and *In*) as [66],

$$\mathrm{R} = \frac{GN_{Se}}{\left(HN_{Ge} + FN_{Sb} + IN_{In}\right)} \tag{3.19}$$

where $F$, $G$, $H$, $I$ are the atomic fractions and $N_{Sb} = 3$, $N_{Se} = 2$, $N_{Ge} = 4$, $N_{In} = 3$ are the coordination numbers of *Sb*, *Se*, *Ge* and *In* respectively. R > 1 signifies that the system is chalcogen rich and R < 1 indicates chalcogen poor material. Mean bond energy of the system $Sb_FSe_GGe_HIn_I$ has been calculated using equation (3.6).

For R > 1,

$$\langle E_c \rangle = 4HE_{Ge-Se} + 3IE_{In-Se} + 3FE_{Sb-Se} \tag{3.20}$$

$$\langle E_{rm} \rangle = \frac{\left(2G - 3F - 4H - 3I\right)}{m} E_{Se-Se} \tag{3.21}$$

where $E_{In-Se}$ is the bond energy of *In–Se* bond.

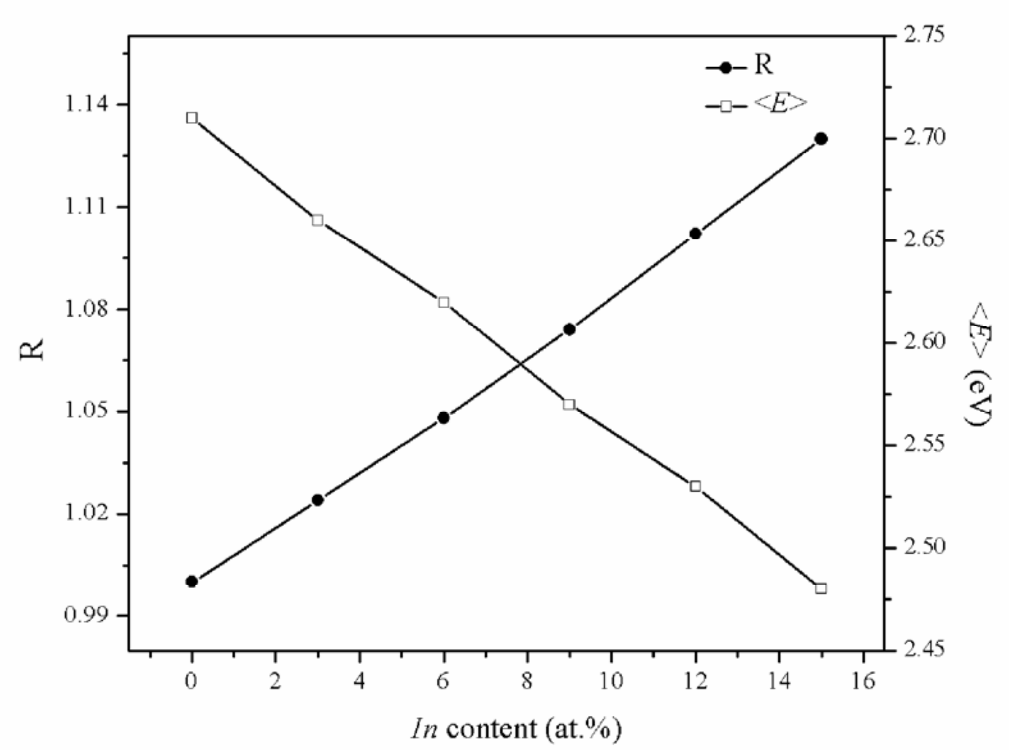

**Figure 3.6** Variation of parameter R and mean bond energy (<*E*>) with increasing *In* content in $Sb_{10}Se_{65}Ge_{25-y}In_y$ system.

The glass transition temperature for *Sb–Se–Ge–In* quaternary system has been calculated using Tanaka's approach [190],

$$T_g = e^{1.6m+2.3} \tag{3.22}$$

The calculated values of $T_g$ have been inserted in Table 3.4. Figure 3.6 shows the variation of R and <*E*>. It has been observed that for $y = 0$, R = 1, which indicates that the system contains only trigonal $Sb_2Se_3$ and tetrahedral $(GeSe_{1/2})_4$ units. This signifies that a full 3–dimensional network between the two structural units has been attained. The $Sb_{10}Se_{65}Ge_{25}$ system can be written as $(GeSe_2)_{25}(Sb_2Se_3)_5$.

With increase in *In* at.%, R increases with values greater than 1 and <*E*> decreases. The obtained values of R suggest that with *In* addition the system becomes chalcogen rich. For R > 1 the system also contains *Se–Se* homopolar bonds. The value of mean bond energy <*E*> decreases with *In* introduction into the ternary glass matrix. This may be due to the fact that for $y = 0$ only heteropolar *Ge–Se* and *Sb–Se* bonds with structural units $Ge(Se_{1/2})_4$ and $Sb_2Se_3$ exists. But, with *In* addition *Ge* content decreases and hence, the *Ge–Se* bonds. The lower energy *In–Se* bond formation takes place and increases with *In* content. This decreases the values of <*E*> with *In* alloying. As <*E*> and $T_g$ are directly related to each other so, $T_g$, also varies in accordance with <*E*> (Table 3.4).

The cohesive energy of the system has been calculated using the CBA [183]. The heteropolar bond energies have been calculated using equation (3.13). The degree of covalency ($C_c$) of these bonds has been calculated using the expression [191],

$$C_c = 100\exp\left[-(\chi_A - \chi_B)^2 \big/ 4\right] \tag{3.23}$$

where $\chi_A$ and $\chi_B$ are the electronegativities of atoms *A* and *B*. $C_c$ varies with the electronegativity difference between the two atoms. The electronegativity values of *Se*, *Sb*, *Ge* and *In* are 2.55, 2.05, 2.01 and 1.78 respectively [188]. The covalency values for different bonds in decreasing order have been given in Table 3.5.

The *CE* decreases with increase in *In* at.% from 3 to 15. The *Se* atoms are strongly bonded to the *Ge* atoms and fill the available valences of the *In* and *Sb* atoms respectively. But, still there are unsaturated *Se* atoms which appear as excess *Se–Se* bonds in the system. With increase in *In* content, *Ge–Se* bonds concentration decreases having bond energy 49.42 kcal/mol and *In–Se* bonds concentration increases having bond energy 48.20 kcal/mol. Thus, the overall bond energy of the system decreases and hence, the value of *CE*.

**Table 3.5** Values of average heat of atomization ($H_s$), bond distribution, degree of covalency and cohesive energies (*CE*) for $Sb_{10}Se_{65}Ge_{25-y}In_y$ system.

| *y* | $H_s$ | Bond distribution |  |  |  | Bonds | $C_c$ (%) | *CE* (kcal/mol) |
|---|---|---|---|---|---|---|---|---|
|  |  | *Ge–Se* | *In–Se* | *Sb–Se* | *Se–Se* |  |  |  |
| 0 | 60.81 | 0.7692 | 0 | 0.2308 | 0 | *Ge–Se* | 92.96 | 48.16 |
| 3 | 59.85 | 0.6769 | 0.0692 | 0.2308 | 0.0231 | *In–Se* | 86.22 | 47.95 |
| 6 | 58.89 | 0.5846 | 0.1385 | 0.2308 | 0.0461 | *Sb–Se* | 93.94 | 47.74 |
| 9 | 57.93 | 0.4923 | 0.2077 | 0.2308 | 0.0692 | *Ge–Sb* | 99.96 | 47.53 |
| 12 | 56.97 | 0.4000 | 0.2769 | 0.2308 | 0.0923 | *Ge–In* | 98.68 | 47.32 |
| 15 | 56.01 | 0.3077 | 0.3462 | 0.2308 | 0.1153 | *Sb–In* | 98.19 | 47.11 |

The average heat of atomization, $H_s$, has been calculated, in kcal/g/atom, for $Sb_\gamma Se_\varphi Ge_\kappa In_\psi$ using [185],

$$H_s = \frac{\gamma H_s^{Sb} + \varphi H_s^{Se} + \kappa H_s^{Ge} + \psi H_s^{In}}{100} \tag{3.24}$$

where $\gamma$, $\varphi$, $\kappa$ and $\psi$ are the at.% of *Sb*, *Se*, *Ge* and *In*.

The values of $H_s$ for *Sb*, *Se Ge* and *In* are 62.0, 49.4, 90.0 and 58.0 kcal/g/atom respectively. The $H_s$ values with increasing *In* at.% have been given in Table 3.5. Average single bond energy ($H_s/m$) decreases with an increase in the *In* at.% (Figure 3.7) indicating a decrease in the bond strength of the system.

The electronegativity values have been calculated using Sanderson's principle [187] and plotted for varying *In* content in $Sb_{10}Se_{65}Ge_{25-y}In_y$ alloys (Figure 3.7). As *Ge* is being replaced by electropositive *In* atom so, there is a decrease in the $\chi$ values (Figure 3.7).

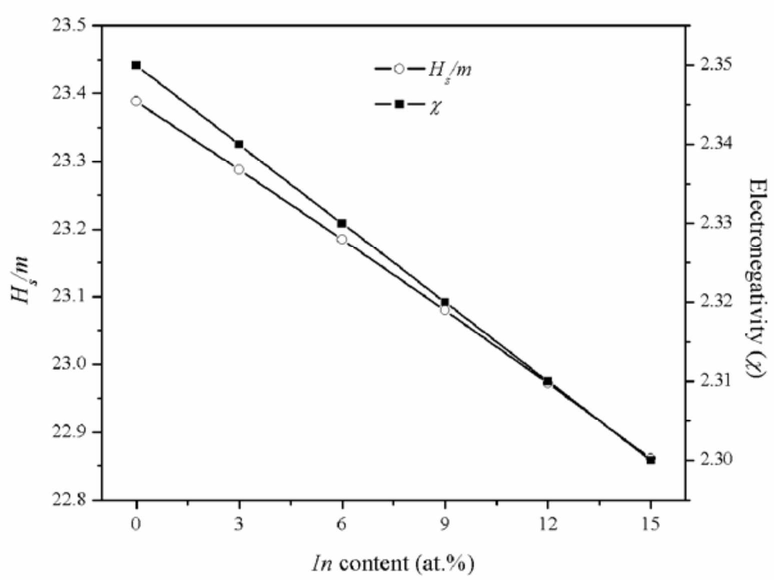

**Figure 3.7** Variation of $H_s/m$ and electronegativity ($\chi$) with increasing *In* content in $Sb_{10}Se_{65}Ge_{25-y}In_y$ system.

### 3.3.3 Structural properties of *Sb–Se–Ge* system

Figure 3.8 shows the IR spectra of $Sb_{10}Se_{90-x}Ge_x$ with $x = 0, 19, 21, 23, 25, 27$ respectively. The bond energies of the possible bonds formed for $Sb_{10}Se_{90-x}Ge_x$ have been calculated using the Pauling relation [184] and are listed in Table 3.6. The relative probabilities of bond formation have also been calculated using the probability distribution function exp ($E/kT$) [192], where $E$ is the bond energy and $k$ *is* Boltzmann constant, at room temperature $T = 300$ K and at $T = 1273$ K (Table 3.6).

The IR transmission measurements have been carried out by employing two assumptions [175]: (a) the valence force field model (VFF) [193], which proposes that a restoring force comes into play if the bond length or the angle between two valence bonds is altered; (b) the position of the intrinsic IR features is influenced by the stretching force constants of corresponding chemical bonds [175].

The wavenumber of the vibration modes of IR spectra has been determined by the interatomic force within the groups of atoms comprising the glass network. The wavenumber is given by the formula [175],

$$\nu = \frac{1}{2\pi c}\left(\frac{K_{AB}}{\mu}\right)^{1/2} \tag{3.25}$$

where $K_{AB}$ is the bond bending or stretching force constant of the bond and $\mu$ is the reduced mass of the molecule and is given by the expression,

$$\mu = {M_1 M_2}/{(M_1 + M_2)} \tag{3.26}$$

$M_1$ and $M_2$ are atomic masses of two atoms.

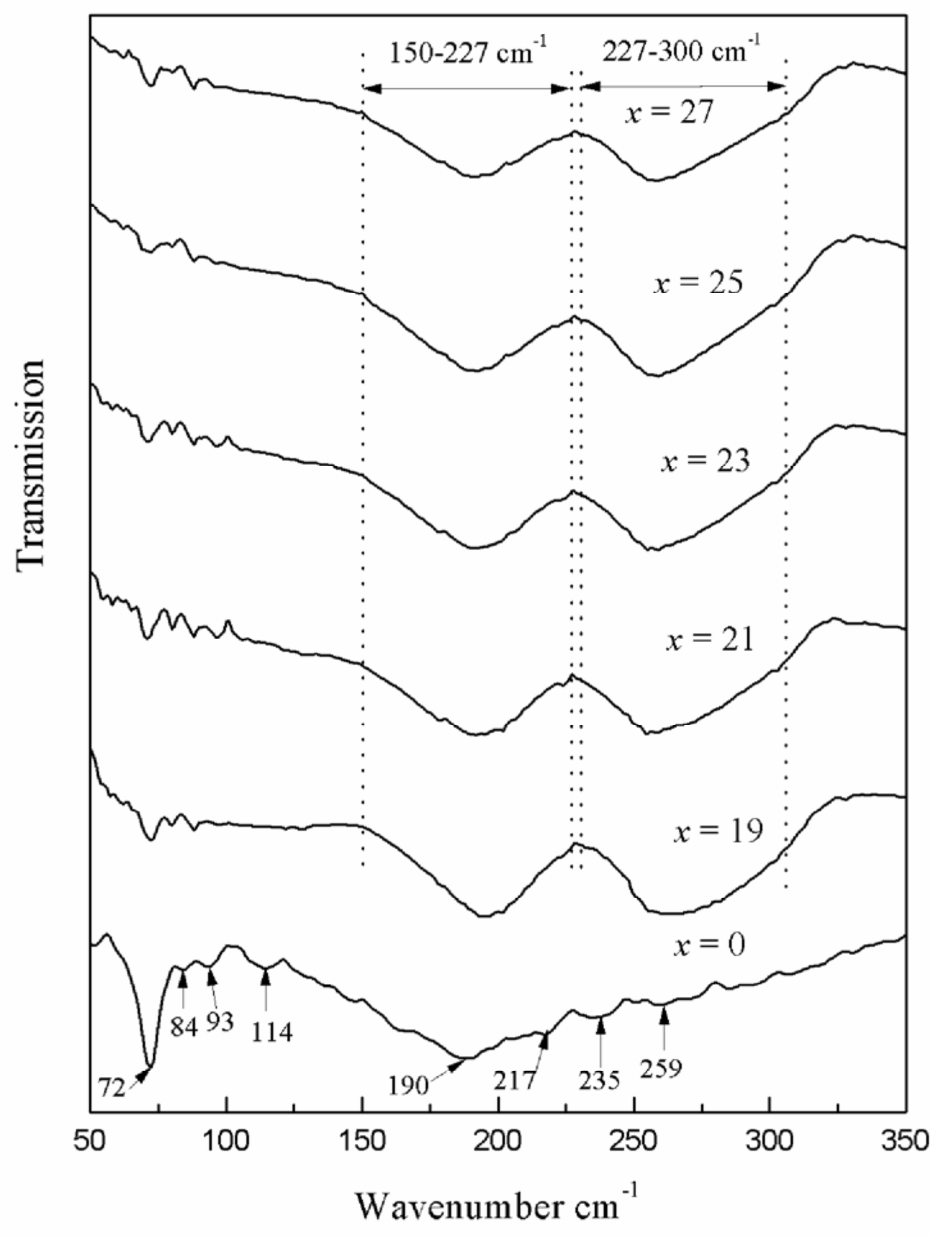

**Figure 3.8** Far–IR transmission spectra of $Sb_{10}Se_{90-x}Ge_x$ system. The $y$–axis scale for different $x$–values has been shifted for clarity.

Somayajulu [194] proposed a method for calculating the force constant using the expression,

$$K_{AB} = (K_{AA}\,K_{BB})^{0.5} + (\chi_A - \chi_B)^2 \tag{3.27}$$

where $K_{AB}$ is the force constant between the elements *A* and *B*, and $K_{AA}$ and $K_{BB}$ are the force constants for the *A–A* and *B–B* bonds respectively. Force constant values for *Sb–Sb*, *Se–Se*, *Ge–Ge* and *In–In* are 0.87, 1.91, 1.20 and 0.15 ($10^5$ dyne $cm^{-1}$) [194] respectively. The theoretically calculated values of $K_{AB}$, $\mu$ and $\nu$ for $Sb_{10}Se_{90-x}Ge_x$ have been given in Table 3.6.

**Table 3.6** Bond energies (*BE*), relative probability of bond formation at 300 K and 1273 K, $\mu$, $K_{AB}$ and $\nu$ for $Sb_{10}Se_{90-x}Ge_x$ and $Sb_{10}Se_{65}Ge_{25-y}In_y$ systems.

| **Bonds** | ***BE* (kcal/mol)** | **Relative probability of bond formation at** | | **$\mu \times 10^{-26}$ ($kgU^{-1}$)** | **$K_{AB}$ (eV)** | **$\nu$ ($cm^{-1}$)** |
|---|---|---|---|---|---|---|
| | | **300 K** | **1273 K** | | | |
| ***Ge–Se*** | 49.42 | 1 | 1 | 6.28 | 1.86 | 289 |
| ***In–Se*** | 48.2 | $1.29 \times 10^{-1}$ | $6.17 \times 10^{-1}$ | 7.76 | 1.12 | 202 |
| ***Se–Se*** | 44 | $1.12 \times 10^{-4}$ | $1.17 \times 10^{-1}$ | 6.55 | 1.91 | 287 |
| ***Sb–Se*** | 43.96 | $1.05 \times 10^{-4}$ | $1.15 \times 10^{-1}$ | 7.95 | 1.53 | 234 |
| ***Ge–Ge*** | 37.6 | $2.44 \times 10^{-9}$ | $9.34 \times 10^{-3}$ | 6.02 | 1.29 | 246 |
| ***Ge–-Sb*** | 33.76 | $3.89 \times 10^{-12}$ | $2.04 \times 10^{-3}$ | 7.55 | 1.06 | 199 |
| ***Sb–Sb*** | 30.22 | $1.02 \times 10^{-14}$ | $5.05 \times 10^{-4}$ | 1.01 | 0.87 | 156 |
| ***Ge–In*** | 29.7 | $4.29 \times 10^{-15}$ | $4.11 \times 10^{-4}$ | 7.38 | 1.73 | 258 |
| ***Sb–In*** | 27.39 | $8.90 \times 10^{-17}$ | $1.65 \times 10^{-4}$ | 9.80 | 0.43 | 112 |
| ***In–In*** | 21.02 | $2.03 \times 10^{-21}$ | $1.33 \times 10^{-5}$ | 9.52 | 1.29 | 195 |

For the $Sb_{10}Se_{90}$ glass, absorption peaks at 72 $cm^{-1}$, 114 $cm^{-1}$, ~ 190 $cm^{-1}$, 235 $cm^{-1}$, 259 $cm^{-1}$ with shoulders at 84 $cm^{-1}$, 93 $cm^{-1}$ and 217 $cm^{-1}$ have been observed. The absorption peak at 72 $cm^{-1}$ corresponds to the $Sb(Se_{1/2})_3$ pyramids [52] and the shoulders at 84 $cm^{-1}$and 93 $cm^{-1}$ represent the $Se_8$ rings as suggested by Ball *et al.* [195] and Ohsaka [196] respectively. The peak situated at 190 $cm^{-1}$ contributes to the

$SbSe_3$ stretching mode as reported by M. Kato *et al.* [197]. Similar peaks have also been observed by Rechtin *et al.* [198] and Sharma *et al.* [199]. The absorption peak at 114 cm$^{-1}$ and shoulder at 217 cm$^{-1}$ correspond well with the absorption peaks for $SbSe_3$ pyramidal units as calculated by Corredor *et al.* [200] at 112 cm$^{-1}$ and 215 cm$^{-1}$. Absorption peaks around 235 cm$^{-1}$ and 259 cm$^{-1}$ have been assigned to *Se* polymeric chain and $Se_8$ ring [$A_1$, $E_2$] modes [195] respectively. Quiroga *et al.* [201] asserted that there is a small contribution of $SbSe_3$ units to the peak around 259 cm$^{-1}$. The contribution of $Se_8$ at 84 cm$^{-1}$ and 93 cm$^{-1}$, and of polymeric *Se* modes at 235 cm$^{-1}$ is very small and may originate from small deviations from stoichiometry in the material [195].

With the addition of *Ge* to the $Sb_{10}Se_{90}$ system, the intensity of absorption peak at 72 cm$^{-1}$ has been observed to decrease gradually. For $x = 25$ the shoulders corresponding to $Se_8$ rings at 84 cm$^{-1}$ and 93 cm$^{-1}$ are not present indicating that the $Se_8$ ring concentration almost vanishes at $x = 25$ (Figure 3.9). This result is also consistent with the chemical bond distribution calculated theoretically for $x = 25$ (Table 3.3).

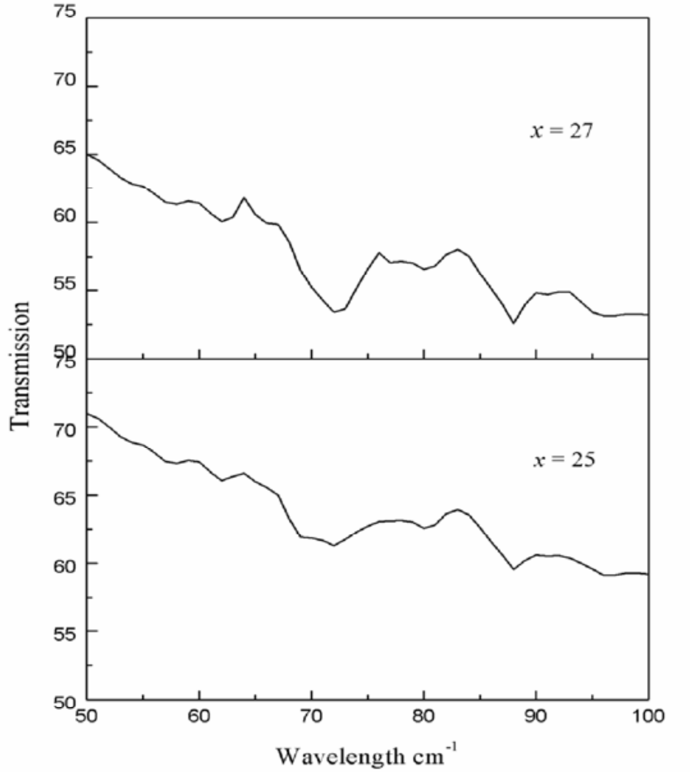

**Figure 3.9** Far–IR transmission spectra for $x = 25$ and $x = 27$ of $Sb_{10}Se_{90-x}Ge_x$ alloys.

With *Ge* alloying the broad band extending from 150 cm$^{-1}$ to 227 cm$^{-1}$ shifts slightly to the higher wavenumber side indicating the formation of new *Ge–Se* bonds having higher energy than the *Sb–Se* and *Se–Se* bonds. This broad band may be composed of various features. Ball and Chamberlain [195] have proposed $GeSe_2$ modes (Raman modes) at 166 cm$^{-1}$, 183 cm$^{-1}$, 197 cm$^{-1}$ and 217 cm$^{-1}$. Due to lack of symmetry in chalcogenide glasses, selection rules are not strictly valid. This relaxation of selection rules may make Raman modes active in the IR spectra, which would have been otherwise inactive for crystalline material [202]. There may also exist contribution of $GeSe_4$ (part of $\nu_1$ mode with 217 cm$^{-1}$) and $GeSe_4$ (part of $\nu_1$ mode with 197 cm$^{-1}$) at 197 cm$^{-1}$ and 217 cm$^{-1}$ respectively [195]. Izvekov *et al.* [203] have reported a band at 170 cm$^{-1}$ due to the vibration of *Ge–Ge* bonds in the $Ge_2(Se_{1/2})_6$ structural units. Fukunga *et al.* [204] also found a weak band at 220 cm$^{-1}$ owing to the vibration of *Ge–Ge* bonds in the $GeSe_2$. For $x$ = 19 to 27 a broad band from 230 cm$^{-1}$ to 300 cm$^{-1}$ has been observed to which the main contribution may be due to wavenumbers at 271 cm$^{-1}$ ($GeSe_2$ (Raman mode) [195]), 278 cm$^{-1}$ ($F_2$ mode of $Ge(Se_{1/2})_4$ tetrahedra [204]) and 285 cm$^{-1}$ (*Ge–Se–Ge* ($\nu_1$ mode) [195]).

The relative probability of bonds (Table 3.6) indicates that for $x = 0$, *Sb–Se* and *Se–Se* bonds are formed. With *Ge* addition broad bands in the range 150 cm$^{-1}$ to 227 cm$^{-1}$ and 230 cm$^{-1}$ to 300 cm$^{-1}$ for *Ge–Se* bonds have been observed which have higher probability of formation than *Ge–Ge*, *Ge–Sb* bonds. For $x = 25$, the glassy network becomes more crosslinked and hence, rigid (Figure 3.9). For $x > 25$ no more change in structure is observed. The theoretically calculated values of wavenumber are slightly higher than the experimentally obtained results (Table 3.6).

### 3.3.4 Structural properties of *Sb–Se–Ge–In* system

Figure 3.10 shows the far–IR spectra of $Sb_{10}Se_{65}Ge_{25-y}In_y$ ($y$ = 0, 3, 6, 9, 12, 15) system. The theoretically calculated values of $K_{AB}$, $\mu$ and $\nu$ for $Sb_{10}Se_{65}Ge_{25-y}In_y$ have been given in Table 3.6.

The effect of *In* incorporation has been studied with $Sb_{10}Se_{65}Ge_{25}$ as the base composition as it has the highest rigidity among investigated compositions. So, the glassy system $Sb_{10}Se_{65}Ge_{25-y}In_y$ ($y$ = 0, 3, 6, 9, 12, 15) has been studied for its bonding arrangements. New absorption peaks at 88 cm$^{-1}$ for $y = 0$ to $y = 15$ and at 98 cm$^{-1}$ for

$y$ = 9, 12, 15 have been observed representing $Se_8$ ($E_2$) mode and trigonal *Se* ($A_2$ mode) [53, 192]. This indicates that $Se_8$ rings reappear with *In* addition as the fourfold *Ge* may have been replaced by threefold *In,* liberating *Se* atoms. Thus, the unsaturated *Se* appears as $Se_8$ rings in the system. Similar results have been obtained from the theoretically calculated bond distribution values on *In* addition to the ternary $Sb_{10}Se_{65}Ge_{25}$ system (Table 3.5).

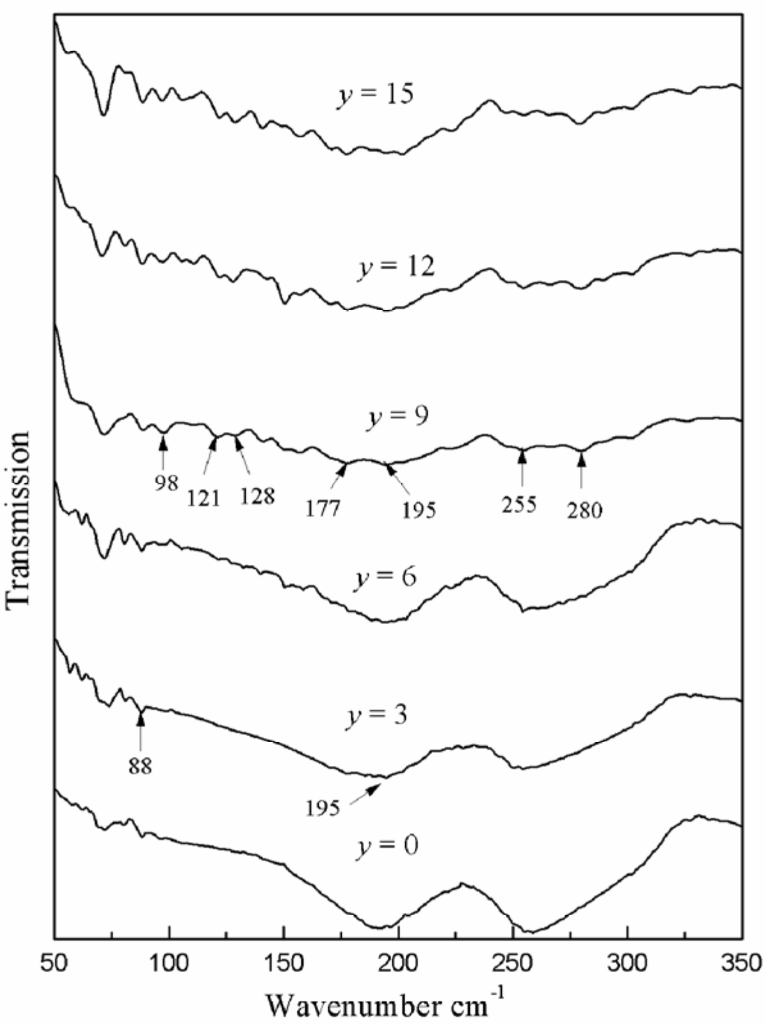

**Figure 3.10** Far–IR transmission spectra of $Sb_{10}Se_{65}Ge_{25-y}In_y$ system. The $y$–axis scale for different $x$–values has been shifted for clarity.

With the addition of *In*, the band extending from 150 cm$^{-1}$ to 227 cm$^{-1}$ has been observed to get narrower for 3 and 6 at.% *In*. As the *In* concentration increases, the intensity of this band diminishes and two absorption peaks of weak intensity become distinguishable at 177 $cm^{-1}$ and 195 $cm^{-1}$. Their intensity has been observed to increase for 9 to 15 at.% of *In* addition. In the Raman spectrum studies also [205], the peak at 177 $cm^{-1}$ has been assigned to *In–Se* bond relative to $InSe_4$ molecular units. The absorption peak of weak intensity at 195 $cm^{-1}$ is a characteristic of *In–In* bonds, as calculated theoretically (Table 3.6). This may be due to unsaturated *In* left after bonding. There is also a probability of contribution from vibrations of *Sb–Se* bond as reported by Sharma *et al.* at 200 $cm^{-1}$ [199]. The broad band ranging from 230 $cm^{-1}$ to 300 $cm^{-1}$, for $y = 0$ has been observed to become slightly narrower for 3 and 6 at.% of *In* addition. Its intensity has been found to decrease and two absorption peaks of weak intensity at 255 $cm^{-1}$ and 280 $cm^{-1}$ have been prominently observed for higher *In* concentration. Weszka *et al.* [205] have reported a peak at 255 $cm^{-1}$ in the Raman scattering spectrum of $In_2Se_3$. The absorption peak at 280 $cm^{-1}$ may be assumed to be associated with the presence of $GeSe_2$ units, by analogy with an active Raman mode [195], and to $Ge(Se_{1/2})_4$ tetrahedra, as evidenced by the isolated $F_2$ mode [204]. Though *In–Se* and *Ge–Se* bonds have very close bonding energy, the *Ge–Se* bonds are more, as has been indicated by the theoretical calculations (Table 3.6). Two absorption doublets which may arise from *Sb–Sb* and *Sb–In* bonds have been observed for $y \geq 9$ at 121 $cm^{-1}$, 128 $cm^{-1}$, and for $y \geq 6$ at 150 $cm^{-1}$, 158 $cm^{-1}$ respectively. The intensity of absorption peak at 72 $cm^{-1}$ has been found to increase with increasing *In* concentration signifying the presence of $Sb(Se_{1/2})_3$ pyramidal units [52].

The bond energies and relative probability of bond formation at room temperature (300 K) and at 1273 K (Table 3.6) indicate that for *Sb–Se–Ge–In* quaternary system, the formation of *Ge–Se*, *In–Se*, *Sb–Se* and *Se–Se* bonds is favored in respective order. However minority homopolar *In–In* and *Sb–Sb* and heteropolar *Sb–In* bonds also exist in the system with high *In* content.

## 3.4 Conclusion

The structure of the chalcogenide glass system $Sb_{10}Se_{90-x}Ge_x$ becomes rigid as the *Ge* content is increased in binary system $Sb_{10}Se_{90}$. The addition of *Ge* induces a large degree of crosslinking with an increase in density and compactness of the glass.

For $Sb_{10}Se_{65}Ge_{25}$ composition system contains only heteropolar bonds resulting in maxima for $<E>$, $T_g$ and $CE$. Average single bond energy, electronegativity and lone pair electrons decrease for ternary glass system. Indium addition to $Sb_{10}Se_{65}Ge_{25}$ decreases the crosslinking of the system. The density and compactness of the system increases with increasing *In* at.%.

Far–IR study shows that the *Ge* addition to $Sb_{10}Se_{90}$ gives rise to new *Ge–Se* modes along with $SbSe_3$ units and $Se_8$ rings. $Se_8$ rings almost disappear for $x = 25$ which is the most crosslinked composition. The *In* addition to $Sb_{10}Se_{65}Ge_{25-y}In_y$ leads to structural changes with the formation of $InSe_4$, $In_2Se_3$ units and of *In–Se* bonds at the expense of the *Ge–Se* bonds. The absorption peak at 195 $cm^{-1}$ has been attributed to *In–In* bonds, as has also been observed from the theoretically calculated bond energy. The substitution of *Ge* by *In* leads to a lesser degree of crosslinking of the glass network.

# CHAPTER 4

# Thermal properties of *Sb-Se-Ge and Sb-Se-Ge-In* systems

- **Sunanda Sharda**, Neha Sharma, Pankaj Sharma and Vineet Sharma, "Glass Transition and Crystallization Kinetics Analysis of Sb-Se-Ge Chalcogenide Glasses" 2013, **Journal of Thermal Analysis and Calorimetry**, doi: 10.1007/s10973-013-3200-6.

- **Sunanda Sharda**, Neha Sharma, Pankaj Sharma and Vineet Sharma, "Thermal Stability and Crystallization Kinetics of Sb-Se-Ge-In Chalcogenide Glasses" (2013), **Communicated**.

In this chapter, the thermal properties of $Sb_{10}Se_{90-x}Ge_x$ and $Sb_{10}Se_{65}Ge_{25-y}In_y$ glasses have been described. Non–isothermal technique has been used to get the three characteristic temperatures. The relaxation and crystallization processes of the glasses have been analyzed.

## 4.1 Introduction

The thermal stability of chalcogenide glasses is related to the nucleation and growth process which in turn depends on glass transition and crystallization kinetics [206]. Glass transition temperature ($T_g$) is a thermally activated process and the atomic rearrangements take place around this temperature [207]. The more readily atomic rearrangements take place, the more stable glass is formed. The crystallization kinetics dominate the devitrification of the glassy solids. The two processes glass transition and crystallization, limit the applications of inorganic glassy materials. Chalcogenide glasses can be potentially used in threshold and memory switching devices [23, 24]. Glassy alloys must be stable in the amorphous state at low temperature and should have a short crystallization time to be used as an optical recording media [208]. The switching properties depend upon crystallization temperature ($T_c$) and hence, the thermal stability of the glasses. These characteristics rely on the composition of the system. Higher the value of $T_c$ for a particular composition more will be the thermal stability of the glass [209] and therefore, better will be its suitability for applications.

Thermally activated transformations in the solid can be investigated by isothermal and non–isothermal processes [210, 211]. In isothermal conditions the sample is brought quickly above the $T_g$ and the heat evolved during the crystallization is noticed as a function of time. While in non–isothermal conditions the sample is heated at a constant rate and the difference in temperature between sample and reference is recorded as a function of time or temperature. Isothermal methods are more definite but non–isothermal analytical techniques are preferred over them because of their several advantages. Non–isothermal technique can be performed rapidly. The temperature range of measurements can be extended in non–isothermal techniques. Some of the transformations takes place readily which cannot be measured under isothermal techniques.

This chapter deals with the study of glass–crystal transformation of $Sb_{10}Se_{90-x}Ge_x$ ($x$ = 0, 19, 21, 23, 25, 27) and $Sb_{10}Se_{65}Ge_{25-y}In_y$ ($y$ = 0, 3, 6, 9, 12, 15) alloys. Differential thermal analysis (DTA) has been used to determine the glass transition temperature ($T_g$), crystallization temperature ($T_c$) and melting temperature ($T_m$) of alloys. Non–isothermal technique is used instead of isothermal technique. The thermal stability and glass forming tendency have been studied in terms of $\Delta T$ (= $T_c$ - $T_g$) and reduced glass transition temperature ($T_{rg}$). Heating rate dependence of $T_g$ has been evaluated. The activation energy of glass transition has been determined by Moynihan's method [156] and Kissinger's method [153]. The activation energy of crystallization has been calculated using Mahadevan's method [157] and Augis–Benett method [158].

## 4.2 Experimental details

Bulk samples of $Sb_{10}Se_{90-x}Ge_x$ and $Sb_{10}Se_{65}Ge_{25-y}In_y$ have been prepared using melt quench technique. The details of the melt quench technique have been discussed in section 3.2. The thermal behavior of the samples has been investigated using DTA (EXSTAR TG/DTA 6300). DTA runs have been taken at four different heating rates 5 K/min, 10 K/min, 15 K/min and 20 K/min on finely powdered samples. For each run, approximately 10 mg of the sample has been taken in alumina pans in an atmosphere of dry nitrogen at a flow rate of 200 ml/min under non–isothermal conditions. The analyzer has been calibrated prior to the measurements using the known latent heats of high purity elements zinc, indium and lead. The temperature precision of microprocessor of thermal analyzer for the measurements has been ± 0.1 K.

## 4.3 Results and discussion

### 4.3.1 Thermal properties of *Sb–Se–Ge* system

In the studied temperature range for DTA, three characteristic peaks are observed. The first endothermic step corresponds to $T_g$, second exothermic peak to $T_c$ and third endothermic peak to $T_m$. $T_g$ represents the rigidity of the system. Hence, it provides valuable information about the thermal stability of the glass. Crystallization process is a heating rate dependent phenomenon because nucleation is a thermally activated process whereas $T_g$ depends on heating rate ($\beta$) due to relaxation processes [207].

**Table 4.1** Values of glass transition ($T_g$), crystallization ($T_c$) and melting ($T_m$) temperatures at different heating rates for $Sb_{10}Se_{90-x}Ge_x$ system.

| $x$ | $\beta$ (K/min) | $T_g$ (K) | $T_c$ (K) | $T_m$ (K) |
|---|---|---|---|---|
| 0 | 5 | 327.76 | 400.80 | 495.80 |
| | 10 | 335.45 | 412.48 | 496.59 |
| | 15 | 340.93 | 421.11 | 497.51 |
| | 20 | 343.82 | 424.98 | 498.93 |
| 19 | 5 | 503.36 | 632.57 | 776.60 |
| | 10 | 512.71 | 650.91 | 777.04 |
| | 15 | 519.08 | 659.53 | 778.12 |
| | 20 | 524.18 | 668.40 | 779.98 |
| 21 | 5 | 507.96 | 644.18 | 782.02 |
| | 10 | 518.45 | 660.61 | 788.37 |
| | 15 | 524.20 | 671.00 | 789.62 |
| | 20 | 528.87 | 680.00 | 794.89 |
| 23 | 5 | 513.66 | 651.41 | 783.77 |
| | 10 | 523.36 | 669.37 | 786.17 |
| | 15 | 529.83 | 679.62 | 790.49 |
| | 20 | 534.61 | 687.00 | 796.21 |
| 25 | 5 | 521.59 | 660.58 | 791.56 |
| | 10 | 531.47 | 678.74 | 793.71 |
| | 15 | 538.18 | 688.57 | 795.74 |
| | 20 | 542.83 | 696.64 | 798.88 |
| 27 | 5 | 519.49 | 654.00 | 788.56 |
| | 10 | 530.28 | 670.30 | 792.71 |
| | 15 | 536.36 | 682.27 | 793.74 |
| | 20 | 540.69 | 689.00 | 796.88 |

Figure 4.1 to Figure 4.6 show three characteristic temperatures for $Sb_{10}Se_{90-x}Ge_x$ ($x$ = 0, 19, 21, 23, 25, 27) samples respectively at different heating rates

of 5, 10, 15 and 20 K/min. For $x = 0$, the three parameters, $T_g$, $T_c$ and $T_m$ increase with increase in heating rate (Figure 4.1, Table 4.1). This is due to the fact that with increase in the heating rate, the heat flow increases which shifts the peaks towards higher temperatures. These three parameters also show an increase with the increase in the *Ge* concentration.

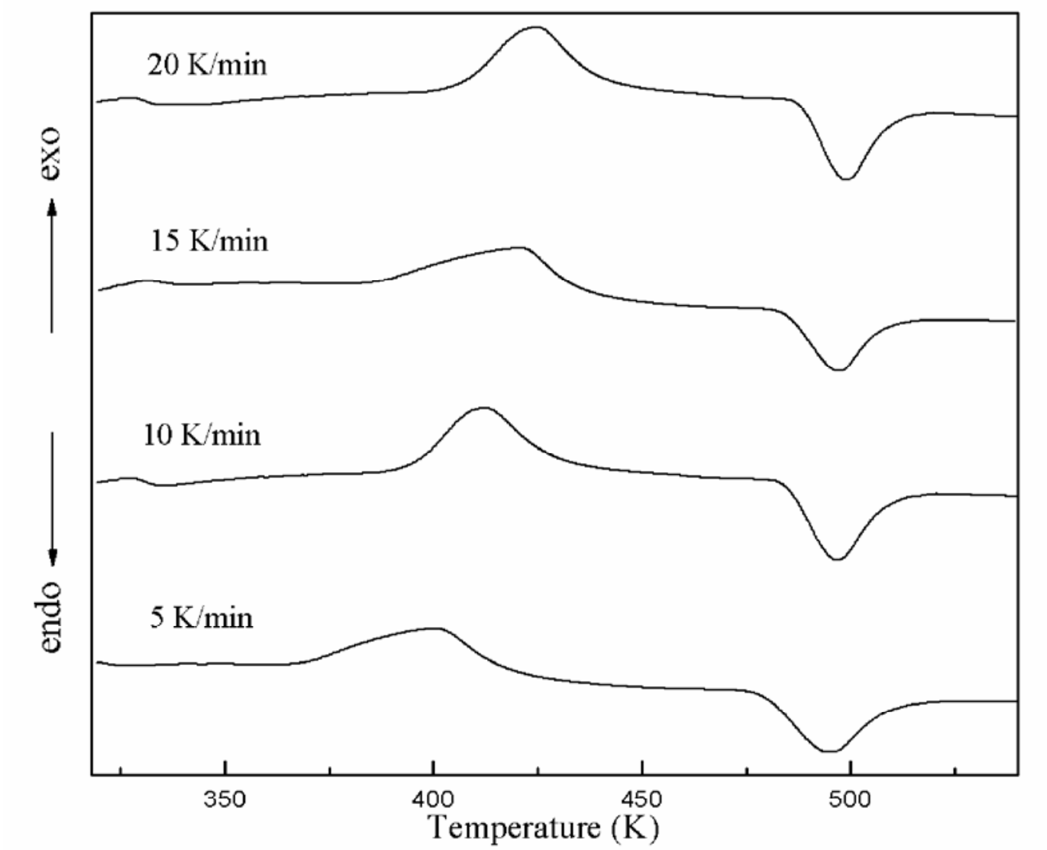

**Figure 4.1** DTA traces of $Sb_{10}Se_{90}$ system at heating rates 5 K/min, 10 K/min, 15 K/min and 20 K/min.

On introducing *Ge* in 19 at.% to the $Sb_{10}Se_{90}$ there is a prominent increase in the values of $T_g$, $T_c$ and $T_m$ (Figure 4.2, Table 4.1). The difference between $T_g$ and $T_c$ increases pointing towards an increase in stability of the system. With further increase in the *Ge* alloying concentration upto 23 at.%, $T_g$, $T_c$ and $T_m$ increase monotonously (Figure 4.3 and Figure 4.4).

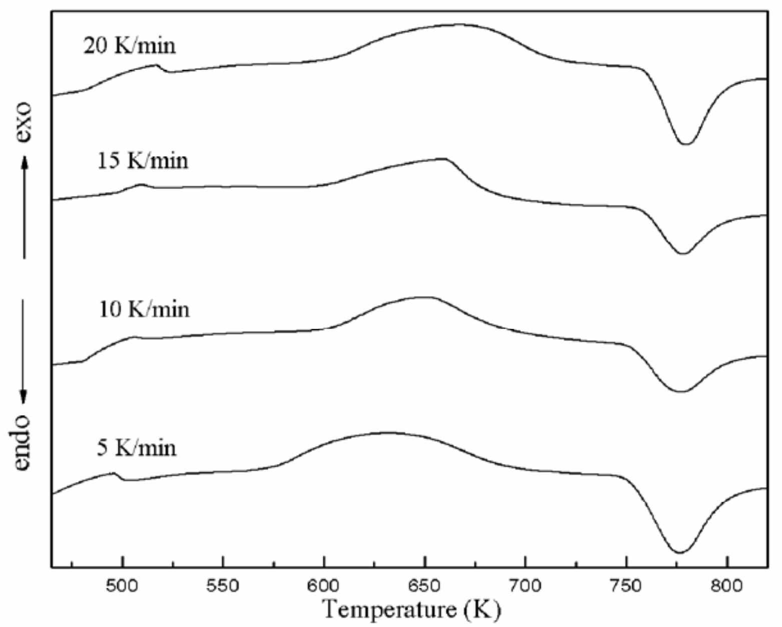

**Figure 4.2** DTA thermogram for $Sb_{10}Se_{71}Ge_{19}$ system at heating rates 5 K/min, 10 K/min, 15 K/min and 20 K/min.

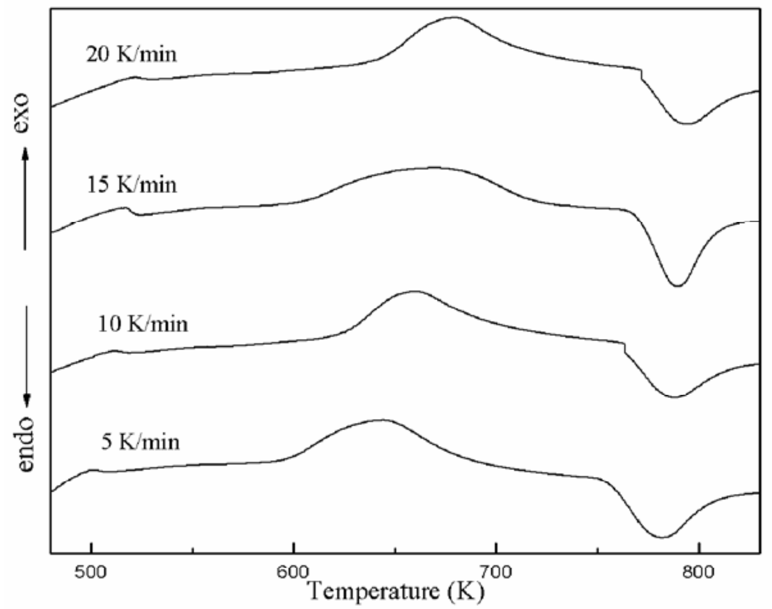

**Figure 4.3** DTA scans of $Sb_{10}Se_{69}Ge_{21}$ system at heating rates 5 K/min, 10 K/min, 15 K/min and 20 K/min.

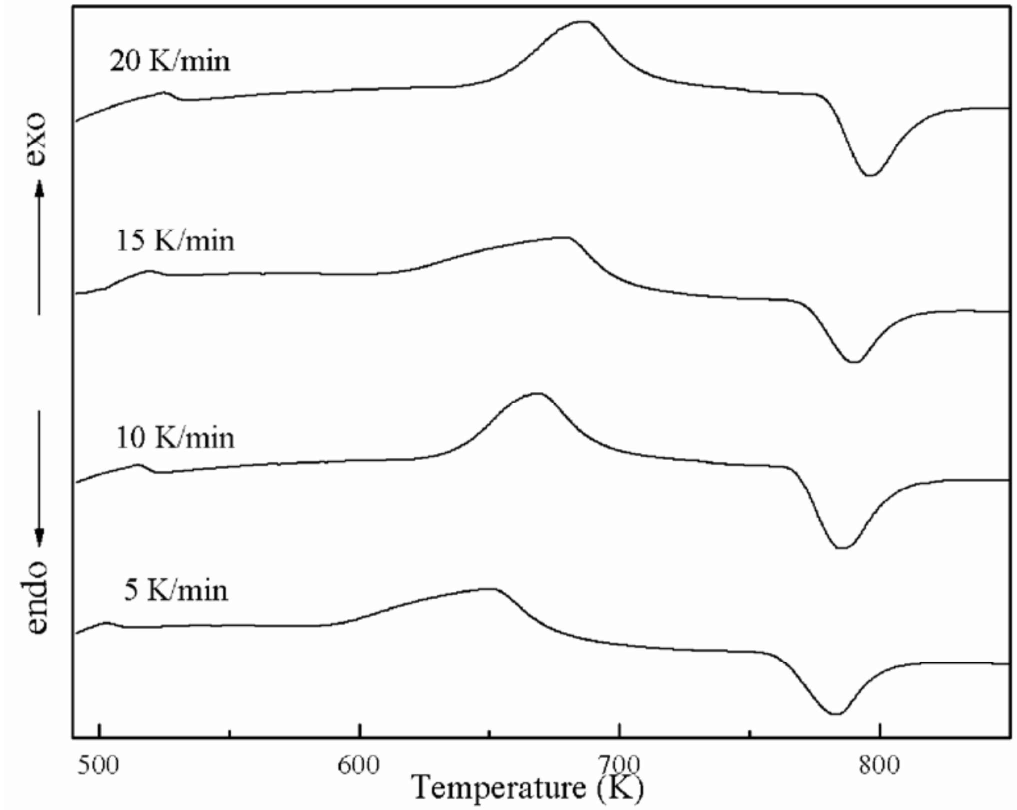

**Figure 4.4** DTA traces of $Sb_{10}Se_{67}Ge_{23}$ system at heating rates 5 K/min, 10 K/min, 15 K/min and 20 K/min.

The values of $T_g$, $T_c$ and $T_m$ are maximum for $Sb_{10}Se_{65}Ge_{25}$ (Figure 4.5 and Table 4.1). Glass transition temperature attains a maximum for $Sb_{10}Se_{65}Ge_{25}$ because *Ge* on entering the polymeric structure of $Sb_{10}Se_{90}$ forms tetrahedral $Ge(Se_{1/2})_4$ units in addition to trigonal $Sb_2Se_3$ units, replacing the *Se–Se* bonds. Thus, the system becomes heavily crosslinked with the formation of $Sb_2Se_3$ and $Ge(Se_{1/2})_4$ units only. From the theoretically calculated $T_g$ values (section 3.3.1, Table 3.2) bond distribution (section 3.3.1, Table 3.3) and far–IR results (section 3.3.3) $Sb_{10}Se_{65}Ge_{25}$ composition has been found to be most stable.

On further increase of *Ge* content, at $x = 27$, the *Sb–Se–Ge* system contains homopolar *Ge–Ge* bonds in addition to $Sb_2Se_3$ and $Ge(Se_{1/2})_4$ structural units, thereby decreasing $T_g$ (Figure 4.6).

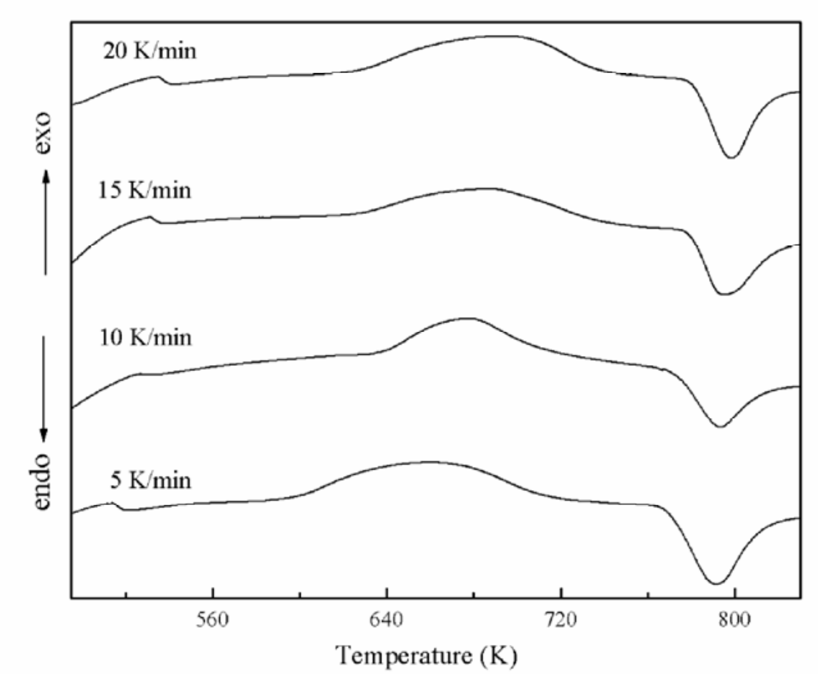

**Figure 4.5** DTA thermogram of $Sb_{10}Se_{65}Ge_{25}$ system recorded at heating rates 5 K/min, 10 K/min, 15 K/min and 20 K/min.

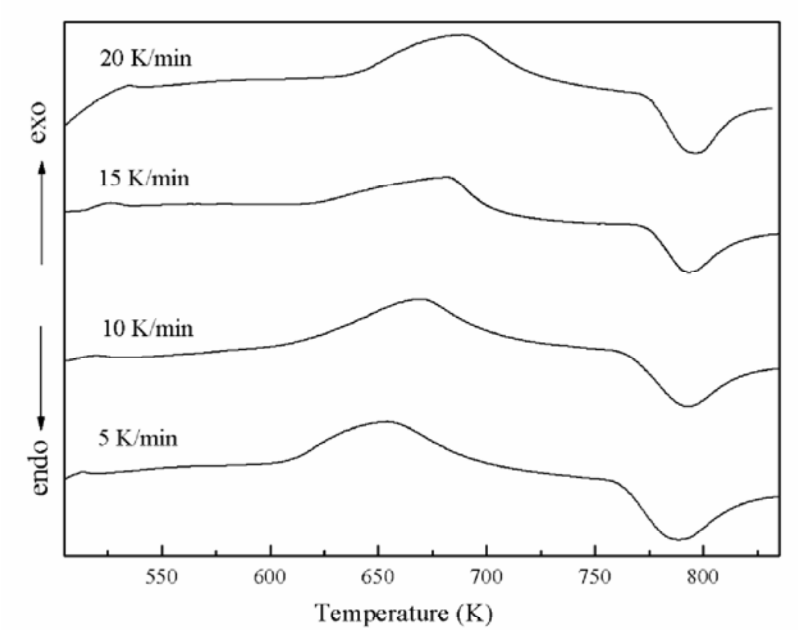

**Figure 4.6** DTA scans for $Sb_{10}Se_{63}Ge_{27}$ system at heating rates 5 K/min, 10 K/min, 15 K/min and 20 K/min.

The thermal stability factor, $\Delta T$ (= $T_c$ - $T_g$) [156], indicates the thermal stability of the glass. The ease of glass formation can also be determined by evaluating $T_{rg}$ (= $T_g/T_m$) values which obey two–third rule [212]. The $T_{rg}$ values are found to be of the order of 2/3 (Table 4.2) indicating a good glass forming tendency of the material. The values of $\Delta T$ increase with an increase in *Ge* content showing maximum at $x = 25$ (Table 4.2). The kinetic resistance to crystallization increases with increase in the $\Delta T$ values. This leads to a slowdown of nucleation rate due to the increase in viscosity of the system [213]. Thus, $Sb_{10}Se_{65}Ge_{25}$ shows maximum thermal stability and lower crystallizing ability in these studied samples.

The heating rate dependence of $T_g$ has been evaluated using the empirical relation [214],

$$T_g = D + E \ln \beta \tag{4.1}$$

where $D$ indicates $T_g$ at a heating rate of 1 K/min, $E$ is related to the cooling rate of the melt and $\beta$ is the heating rate. The values of $D$ and $E$ (Table 4.2) have been determined from the intercept and slope respectively using Figure 4.7.

**Table 4.2** Values of thermal stability factor ($\Delta T$), reduced glass transition temperature ($T_{rg}$), $D$ and $E$ for $Sb_{10}Se_{90-x}Ge_x$ system.

| ***x*** | **Δ*T* (K)** | ***T*$_{rg}$** | ***D* (K)** | ***E*** |
|---|---|---|---|---|
| 0 | 77.03 | 0.6755 | 308.76 | 11.74 |
| 19 | 138.20 | 0.6598 | 479.01 | 14.89 |
| 21 | 142.16 | 0.6576 | 483.84 | 14.98 |
| 23 | 146.01 | 0.6657 | 489.15 | 15.06 |
| 25 | 147.27 | 0.6696 | 496.68 | 15.32 |
| 27 | 140.02 | 0.6689 | 494.93 | 15.29 |

It has been observed that the slope of the curves increases with increase in *Ge* content up to $x = 25$. The slope decreases with further increase in *Ge* alloying concentration. The values of $D$ increase to maximum for $x = 25$ similar to $T_g$ as obtained from the DTA thermograms. The values of $E$ correspond to the time response of configurational changes within the glass transition region to the heating rate.

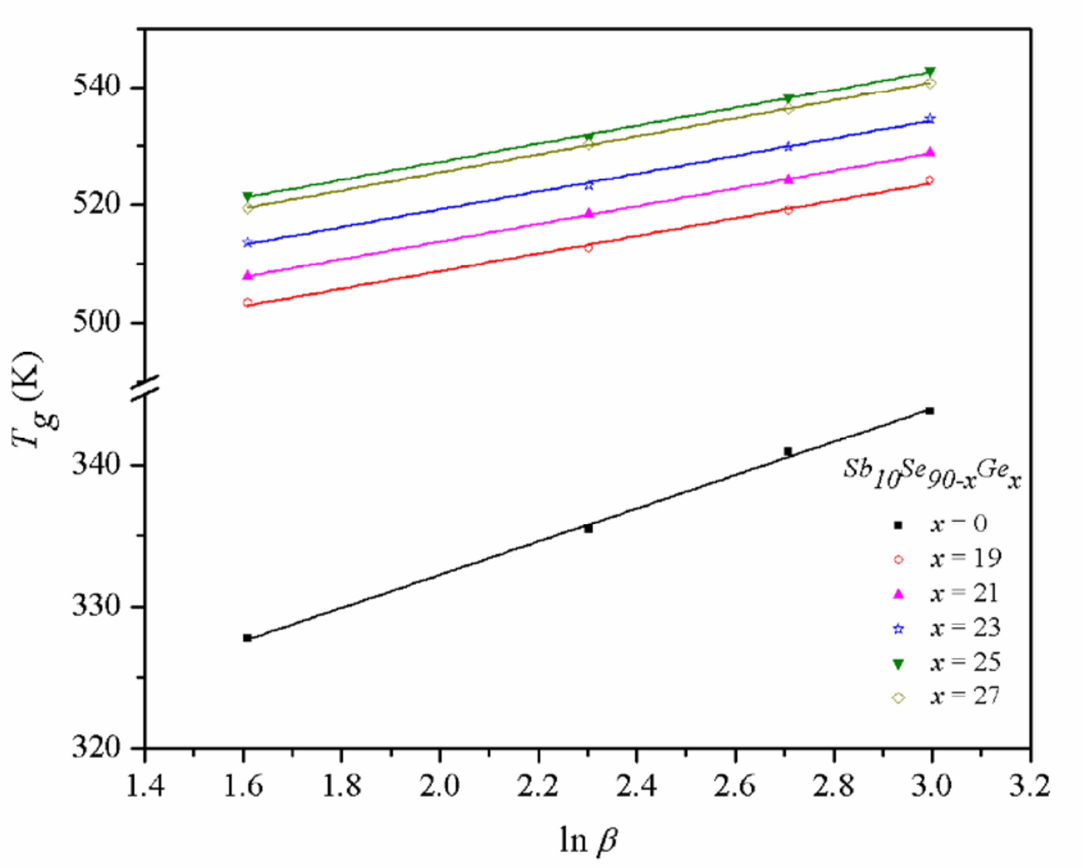

**Figure 4.7** Dependence of glass transition temperature ($T_g$) on heating rate ($\beta$) for $Sb_{10}Se_{90-x}Ge_x$ system.

The values of activation energy of glass transition ($E_g$) have been calculated from the heating rate dependence of $T_g$ using two methods, Moynihan [156] and Kissinger [153], discussed in section 2.5 employing equations (2.2) and (2.3) respectively. The slope of *ln* $\beta$ *vs.* 1000/$T_g$ (Figure 4.8, Moynihan method) and *ln* ($\beta/T_g^2$) *vs.* 1000/$T_g$ (Figure 4.9, Kissinger method) gives the activation energy involved in molecular motions and rearrangements around $T_g$. The activation energy values obtained from both the methods are in good agreement, showing a maximum in $E_g$ at $x = 25$.

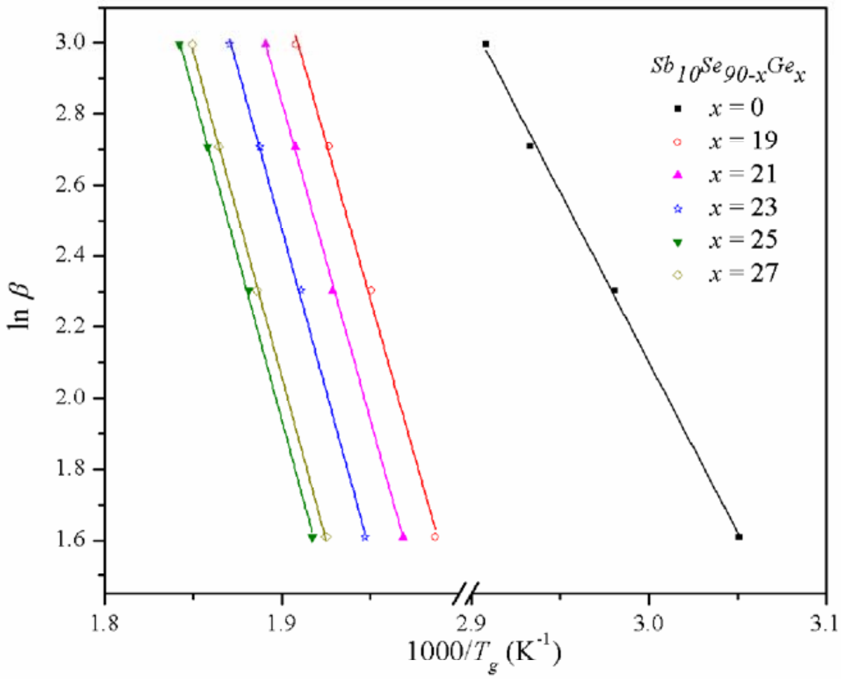

**Figure 4.8** Plot of ln $\beta$ *vs.* 1000/$T_g$ for $Sb_{10}Se_{90-x}Ge_x$ system.

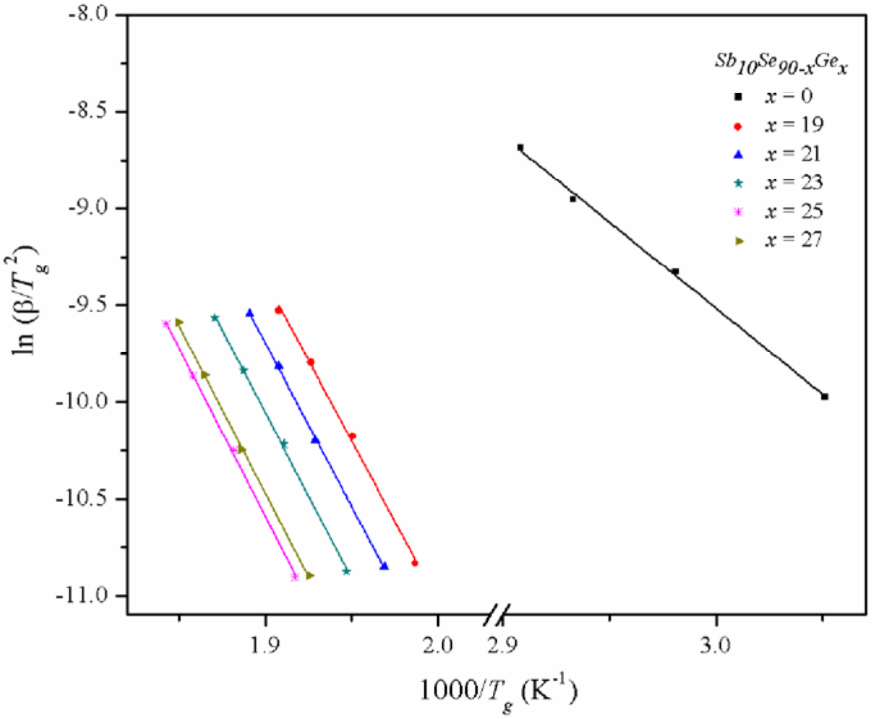

**Figure 4.9** Variation of ln ($\beta/T_g^2$) with 1000/$T_g$ for $Sb_{10}Se_{90-x}Ge_x$ system.

The variation in the values of activation energy calculated (Table 4.3) by the two methods is due to different approximations used in the models. On heating the sample in DTA furnace, atoms undergo transitions between the local potential minima having different characteristic structures in the configuration space and energy barriers. The internal energy associated with the most stable local minimum is lowest and hence, corresponds to the most stable structure. The atoms can jump more easily to these metastable states [77].

**Table 4.3** Values of activation energies for $Sb_{10}Se_{90-x}Ge_x$ system.

| $x$ | $E_g$ **[Moynihan]** ($kJmol^{-1}$) | $E_g$ **[Kissinger]** ($kJmol^{-1}$) | $E_c$ **[Mahadevan]** ($kJmol^{-1}$) | $E_c$ **[Augis and Benett]** ($kJmol^{-1}$) |
|---|---|---|---|---|
| 0 | 79.62 | 73.97 | 79.21 | 75.80 |
| 19 | 146.76 | 138.20 | 137.78 | 132.37 |
| 21 | 148.84 | 140.19 | 142.11 | 136.61 |
| 23 | 151.26 | 142.60 | 144.77 | 139.19 |
| 25 | 153.34 | 144.52 | 147.85 | 142.19 |
| 27 | 152.51 | 143.69 | 146.52 | 140.94 |

The crystallization involves three types of activation energies *i.e.* nucleation, growth and whole crystallization process. The activation energy for growth may be taken equal to the crystallization process, provided it is evaluated using thermal analysis. Activation energy of crystallization ($E_c$) has been evaluated using two different approaches, Mahadevan [157] and Augis and Benett [158], given by equations (2.4) and (2.5) respectively. The slope of $ln\ \beta$ *vs.* $1000/T_c$ (Figure 4.10, Mahadevan method) and $ln\ (\beta/T_c)$ *vs.* $1000/T_c$ (Figure 4.11, Augis and Benett method) gives the value of $E_c$. The value of $E_c$ increases to maximum for 25 at.% of *Ge* addition to $Sb_{10}Se_{90}$ followed by a decrease for $x > 25$.

The values of $E_c$ calculated using different methods are found to be in good agreement with each other (Table 4.3). The maximum for $x = 25$ at.% in $E_c$ values has been interpreted in terms of bond energies of the system calculated using Pauling relation [184] and CBA [183].

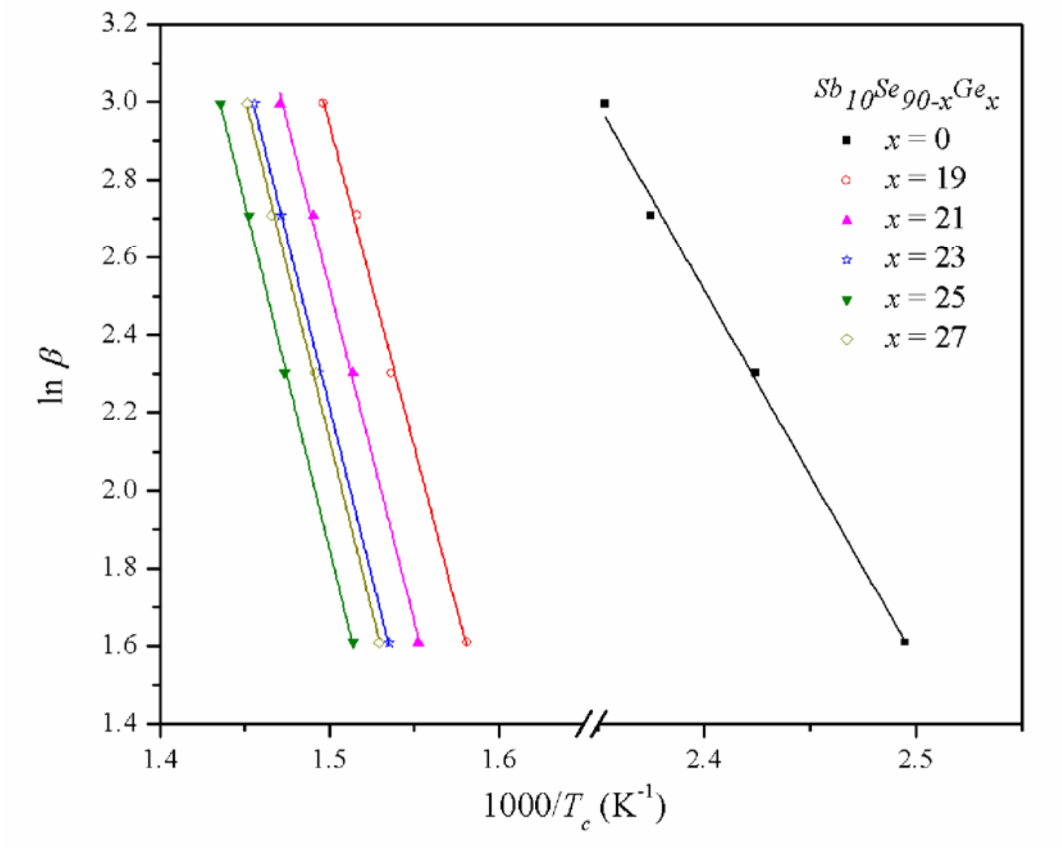

**Figure 4.10** Plot of ln $\beta$ *vs.* 1000/$T_c$ for $Sb_{10}Se_{90-x}Ge_x$ system.

On addition of *Ge*, additional *Ge–Se* bonds having energy 49.42 kcal/mol starts replacing *Se–Se* bonds resulting in an increase of cohesive energy as calculated in section 3.3.1. At $x$ = 25, the system emerges as a 3–dimensional structure with maximum cohesive energy containing only *Ge–Se* and *Sb–Se* heteropolar bonds. The increase in the cohesive energy enhances the bonding strength, therefore, increasing $T_c$ and hence $E_c$ upto $x$ = 25 [85]. The maximum value of $E_c$ for $Sb_{10}Se_{65}Ge_{25}$ indicates that atoms in its glassy state require more energy to jump to the crystalline phase. Therefore, $Sb_{10}Se_{65}Ge_{25}$ is the most stable composition among investigated compositions. For $x$ = 27, homopolar *Ge–Ge* bonds with energy 37.60 kcal/mol are also formed leading to a decrease in the cohesive energy as is evident from the Table 3.3. The decrease in cohesive energy of the system reduces $T_c$ and hence, $E_c$. Therefore, the atoms require less energy to overcome the barrier, decreasing the stability.

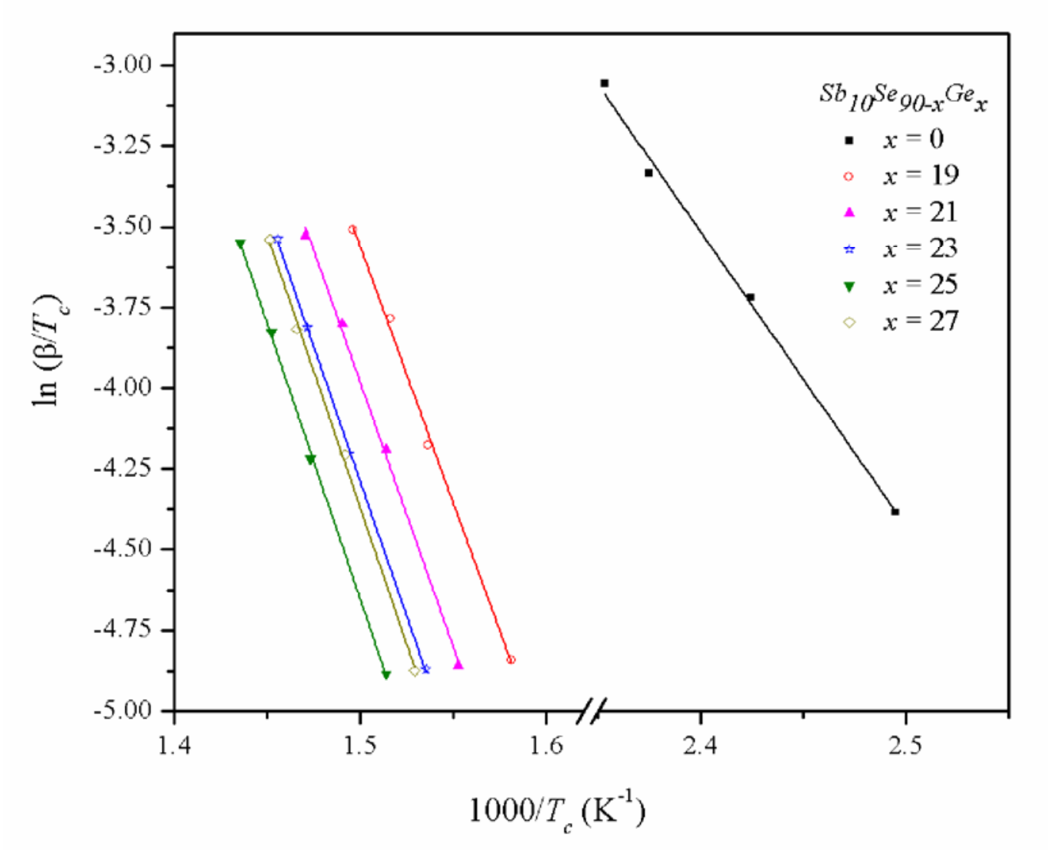

**Figure 4.11** Variation of ln (*β*/$T_c$) with 1000/$T_c$ for $Sb_{10}Se_{90-x}Ge_x$ system.

### 4.3.2 Thermal properties of *Sb–Se–Ge–In* system

The thermal study of ternary glassy alloys reveals that $Sb_{10}Se_{65}Ge_{25}$ is thermally most stable composition *i.e.* the system stays in the amorphous state for a larger temperature range and no other transition takes place between $T_c$ and $T_g$. The operating temperature range of the system may further be increased with the addition of a fourth element which may alter the properties of the system. *In* has been observed to affect the thermal properties of the chalcogenide glasses when added to different base systems [76, 82, 87]. The effect of *In* addition has been studied on the most stable ternary composition.

Figure 4.12 to Figure 4.16 shows the DTA traces of $Sb_{10}Se_{65}Ge_{25-y}In_y$ ($y$ = 3, 6, 9, 12, 15) samples. The first endothermic step corresponds to the glass transition temperature ($T_g$) which is a measure of rigidity of the structure. The second exothermic peak corresponds to the crystallization temperature ($T_c$) which is related to the nucleation and growth phenomenon. The third endothermic peak corresponds to the melting temperature ($T_m$) where all the existing bonds in the material are destroyed and constituent elements are separated.

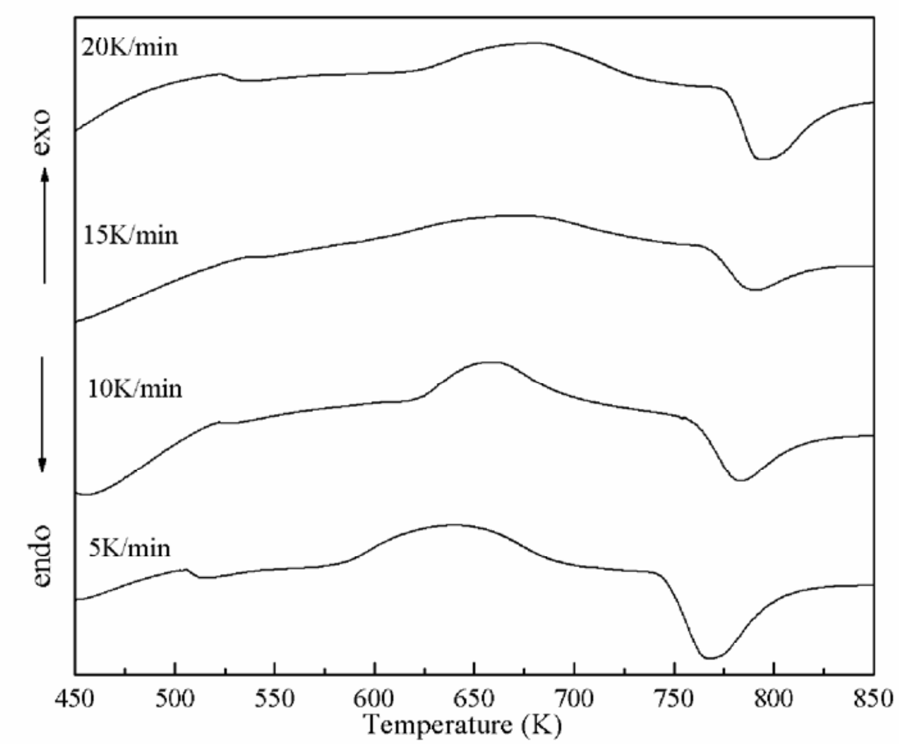

**Figure 4.12** DTA thermogram for $Sb_{10}Se_{65}Ge_{22}In_3$ system at heating rates 5 K/min, 10 K/min, 15 K/min and 20 K/min.

The values of $T_g$, $T_c$ and $T_m$ increase with increase in heating rate due to an increase in heat flow. With *In* addition to the $Sb_{10}Se_{65}Ge_{25}$ system, $T_g$, $T_c$ and $T_m$ decrease. $Sb_{10}Se_{65}Ge_{25}$ consists of only heteropolar *Ge–Se* and *Sb–Se* bonds with structural units $Ge(Se_{1/2})_4$ and $Sb_2Se_3$. But, with the addition of *In* stronger *Ge–Se* bonds are being replaced by lower energy *In–Se* bonds with the formation of $In_2Se_3$ structural units and excess *Se–Se* bonds as obtained from the physical (section 3.3.2, Table 3.5) and far–IR investigations of the quaternary system (section 3.3.4). This decreases $T_g$ and hence, the rigidity of the system. $T_c$ is rate dependent because nucleation is a thermally activated process.

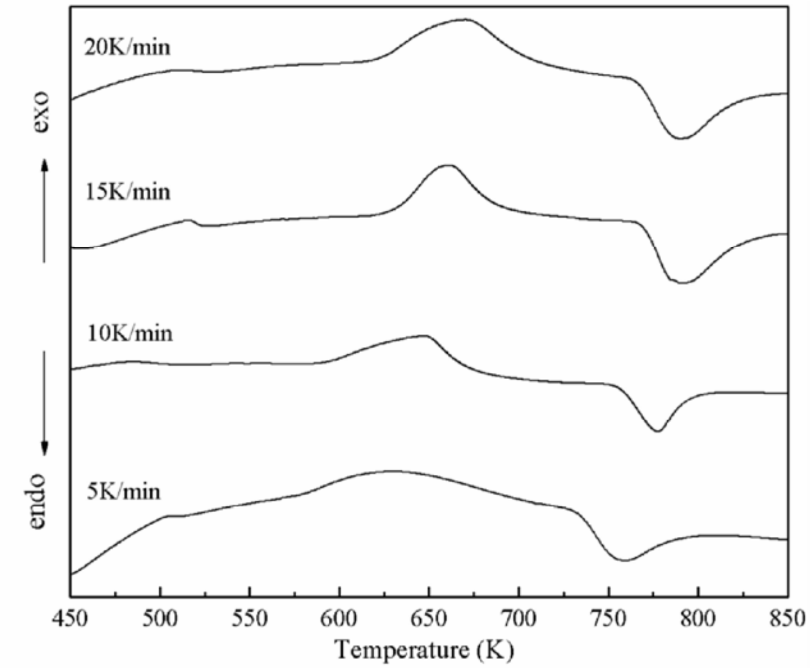

**Figure 4.13** DTA scans of $Sb_{10}Se_{65}Ge_{19}In_6$ system at heating rates 5 K/min, 10 K/min, 15 K/min and 20 K/min.

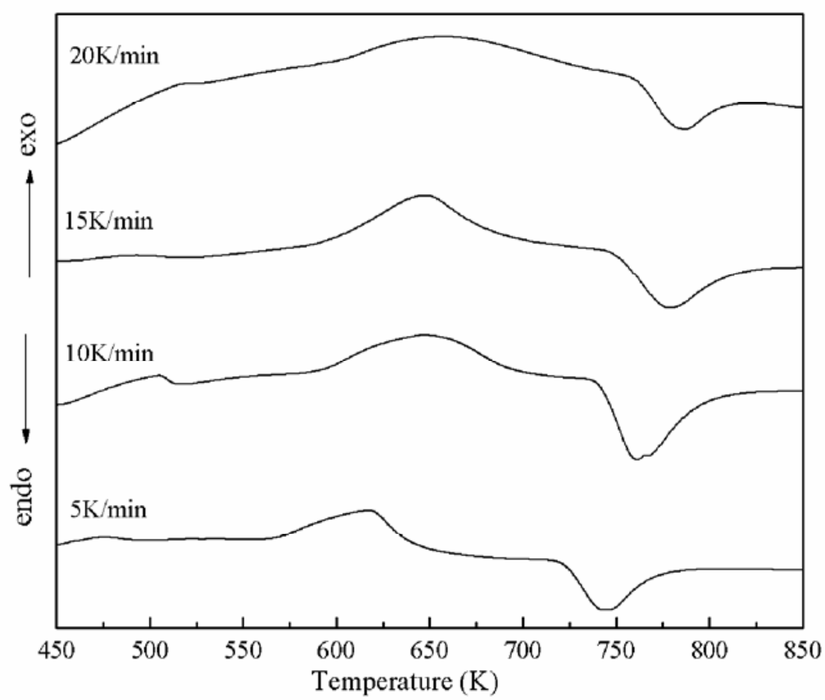

**Figure 4.14** DTA traces of $Sb_{10}Se_{65}Ge_{16}In_9$ system at heating rates 5 K/min, 10 K/min, 15 K/min and 20 K/min.

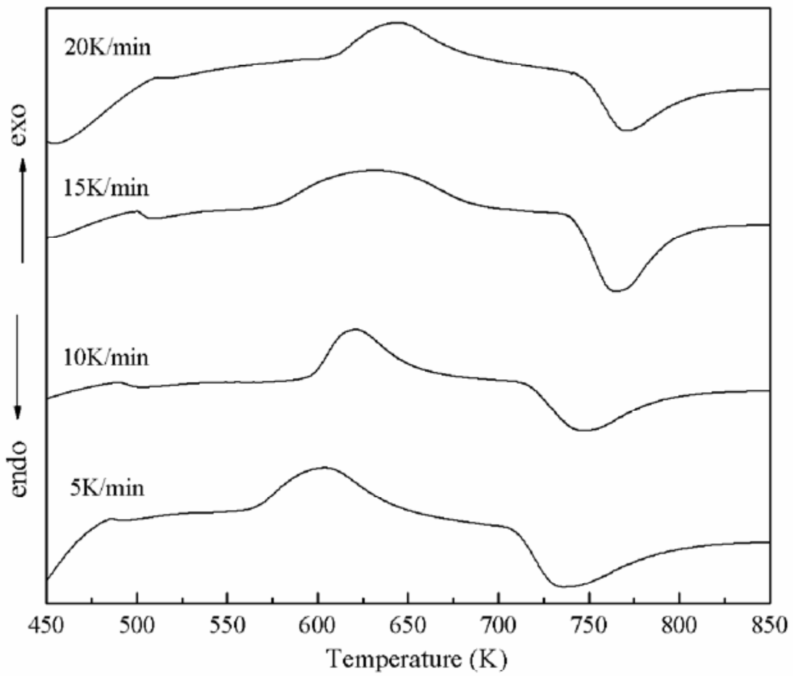

**Figure 4.15** DTA thermogram of $Sb_{10}Se_{65}Ge_{13}In_{12}$ system recorded at heating rates 5 K/min, 10 K/min, 15 K/min and 20 K/min.

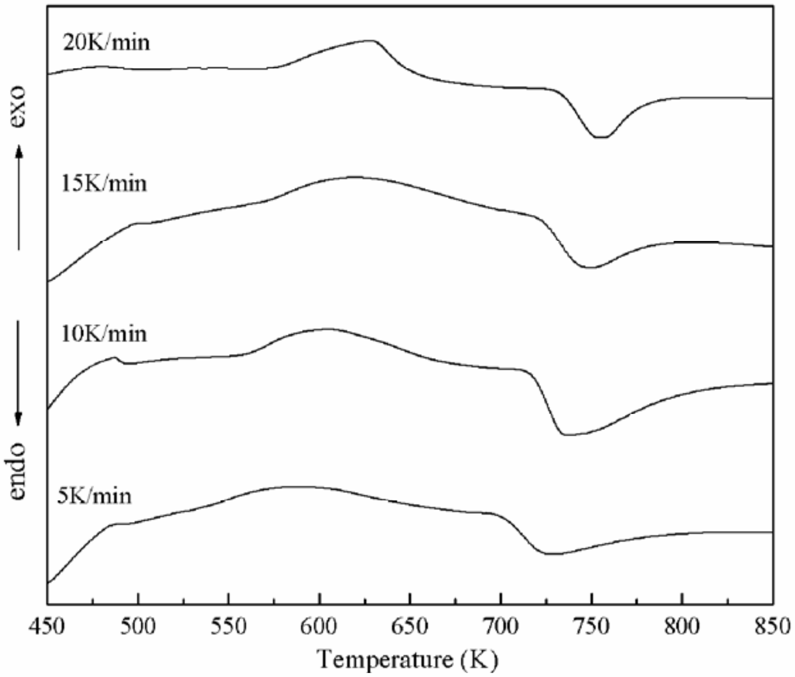

**Figure 4.16** DTA scans for $Sb_{10}Se_{65}Ge_{10}In_{15}$ system at heating rates 5 K/min, 10 K/min, 15 K/min and 20 K/min.

**Table 4.4** Values of glass transition ($T_g$), crystallization ($T_c$) and melting ($T_m$) temperatures at different heating rates for $Sb_{10}Se_{65}Ge_{25-y}In_y$ system.

| $y$ | $\beta$ (K/min) | $T_g$ (K) | $T_c$ (K) | $T_m$ (K) |
|---|---|---|---|---|
| 0 | 5 | 521.59 | 660.58 | 791.56 |
|  | 10 | 531.47 | 678.74 | 793.71 |
|  | 15 | 538.18 | 688.57 | 795.74 |
|  | 20 | 542.83 | 696.64 | 798.88 |
| 3 | 5 | 515.84 | 642.81 | 768.61 |
|  | 10 | 527.01 | 661.12 | 783.75 |
|  | 15 | 532.66 | 673.52 | 791.44 |
|  | 20 | 537.73 | 682.16 | 796.19 |
| 6 | 5 | 508.43 | 630.99 | 759.40 |
|  | 10 | 518.60 | 647.94 | 777.39 |
|  | 15 | 526.01 | 662.00 | 785.84 |
|  | 20 | 530.29 | 670.53 | 790.67 |
| 9 | 5 | 500.80 | 618.00 | 745.76 |
|  | 10 | 513.13 | 638.94 | 768.48 |
|  | 15 | 518.91 | 649.00 | 778.57 |
|  | 20 | 523.71 | 658.81 | 786.93 |
| 12 | 5 | 492.52 | 604.63 | 735.58 |
|  | 10 | 502.48 | 621.98 | 747.39 |
|  | 15 | 509.52 | 635.16 | 765.85 |
|  | 20 | 515.88 | 645.00 | 771.23 |
| 15 | 5 | 485.74 | 589.27 | 728.45 |
|  | 10 | 495.00 | 606.00 | 736.74 |
|  | 15 | 502.62 | 620.48 | 750.15 |
|  | 20 | 508.99 | 628.95 | 756.93 |

The thermal stability factor ($\Delta T$) values indicate that the thermal stability of the glass decreases with increasing *In* at.% (Table 4.5). The kinetic resistance to crystallization increases as the difference between $T_c$ and $T_g$ decreases. Thus, the thermal stability of the system decreases and the system becomes prone to crystallization with *In* addition. The values of $T_{rg}$ have been found to obey the two–third rule indicating a good glass forming ability of the *SbSeGeIn* glassy system (Table 4.5).

**Table 4.5** Values of thermal stability factor ($\Delta T$), reduced glass transition temperature ($T_{rg}$), $D$ and $E$ for $Sb_{10}Se_{65}Ge_{25-y}In_y$ system.

| $y$ | $\Delta T$ (K) | $T_{rg}$ | $D$ (K) | $E$ |
|---|---|---|---|---|
| 0 | 147.27 | 0.6696 | 496.68 | 15.32 |
| 3 | 134.11 | 0.6724 | 490.76 | 15.62 |
| 6 | 129.34 | 0.6671 | 482.58 | 15.91 |
| 9 | 125.81 | 0.6677 | 474.64 | 16.43 |
| 12 | 119.50 | 0.6723 | 465.22 | 16.59 |
| 15 | 111.00 | 0.6719 | 458.28 | 16.56 |

The heating rate dependence of $T_g$ has been evaluated using equation (4.1) [215]. The values of $D$ and $E$ (Table 4.5) have been evaluated from the intercept and slope, respectively, of Figure 4.17.

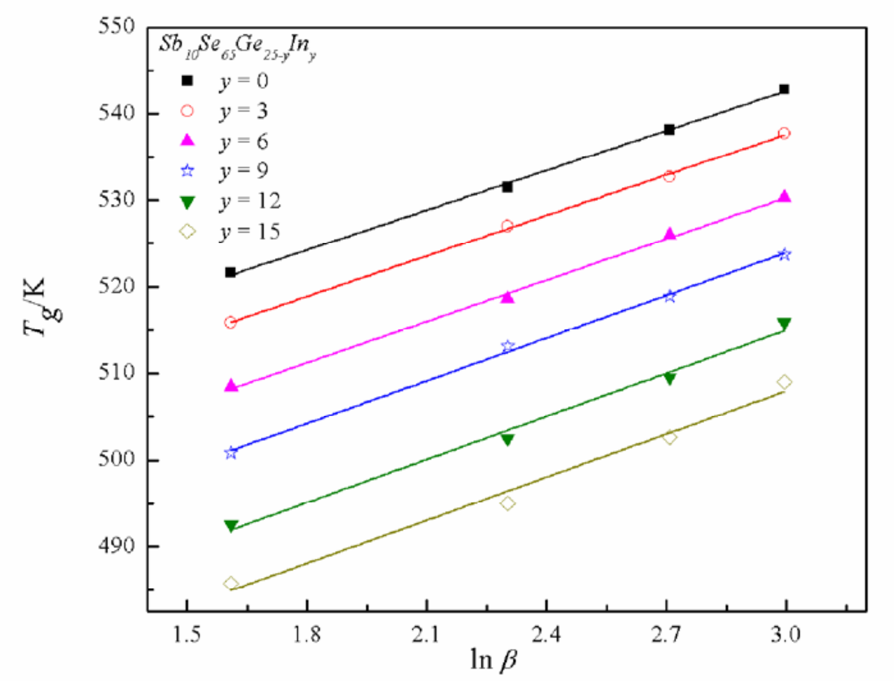

**Figure 4.17** Dependence of glass transition temperature ($T_g$) on heating rate ($\beta$) for $Sb_{10}Se_{65}Ge_{25-y}In_y$ system.

The values of $D$ decrease with increase in $In$ content since the value of $T_g$ also decreases with $In$ concentration. The values of $E$ increase with $In$ alloying concentration indicating an increase in cooling rate of the melt. Moynihan [156] and Kissinger methods [153] using equations (2.2) and (2.3) respectively have been used to calculate activation energy of glass transition ($E_g$). The slope obtained from Figure 4.18 (Moynihan method) and Figure 4.19 (Kissinger method) of $ln\ \beta$ versus $1000/T_g$ plot and ln $(\beta/T_g^2)$ vs. $1000/T_g$ plot respectively gives the value of $E_g$.

**Table 4.6** Values of activation energies for $Sb_{10}Se_{65}Ge_{25-y}In_y$ system.

| $y$ | $E_g$ **[Moynihan]** ($kJmol^{-1}$) | $E_g$ **[Kissinger]** ($kJmol^{-1}$) | $E_c$ **[Mahadevan]** ($kJmol^{-1}$) | $E_c$ **[Augis and Benett]** ($kJmol^{-1}$) |
|---|---|---|---|---|
| **0** | 153.34 | 144.52 | 147.85 | 142.19 |
| **3** | 147.35 | 138.61 | 128.21 | 123.39 |
| **6** | 140.61 | 131.96 | 121.89 | 117.31 |
| **9** | 132.20 | 123.72 | 116.23 | 111.82 |
| **12** | 126.38 | 117.98 | 111.32 | 107.07 |
| **15** | 122.64 | 114.40 | 106.08 | 102.09 |

The value of $E_g$ is the amount of energy absorbed by the group of atoms in the glassy region to jump from one metastable state to another. This indicates that some energy is involved in the molecular motions and rearrangements of the atoms around glass transition temperature. Thus, a decrease in $E_g$ values (Table 4.6) with $In$ implies that atoms have higher probability to overcome the energy barrier in order to jump from one local minimum to other local minimum as we move from $y = 0$ to $y = 15$ [215].

The values of $E_c$ have been evaluated using Mahadevan [157] and Augis and Benett method [158], equations (2.4) and (2.5). The slopes of ln $\beta$ *vs.* $1000/T_c$ (Mahadevan method) and ln $(\beta/T_c)$ *vs.* $1000/T_c$ (Augis and Benett method) in Figures 4.20 and Figures 4.21 respectively give the values of activation energy for glass crystallization.

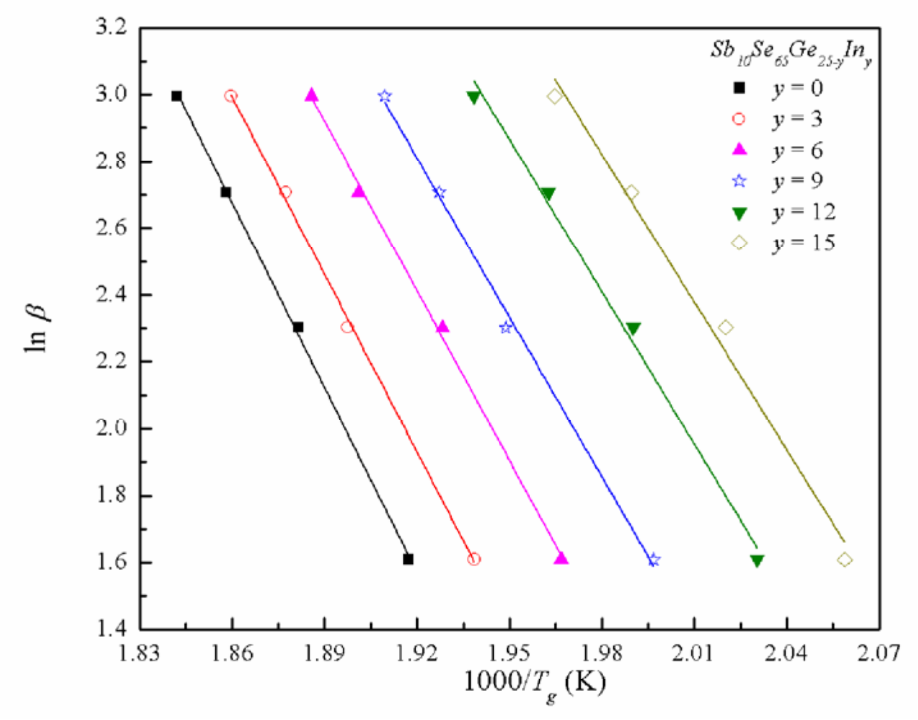

**Figure 4.18** Plot of ln $\beta$ *vs.* $1000/T_g$ for $Sb_{10}Se_{65}Ge_{25-y}In_y$ system.

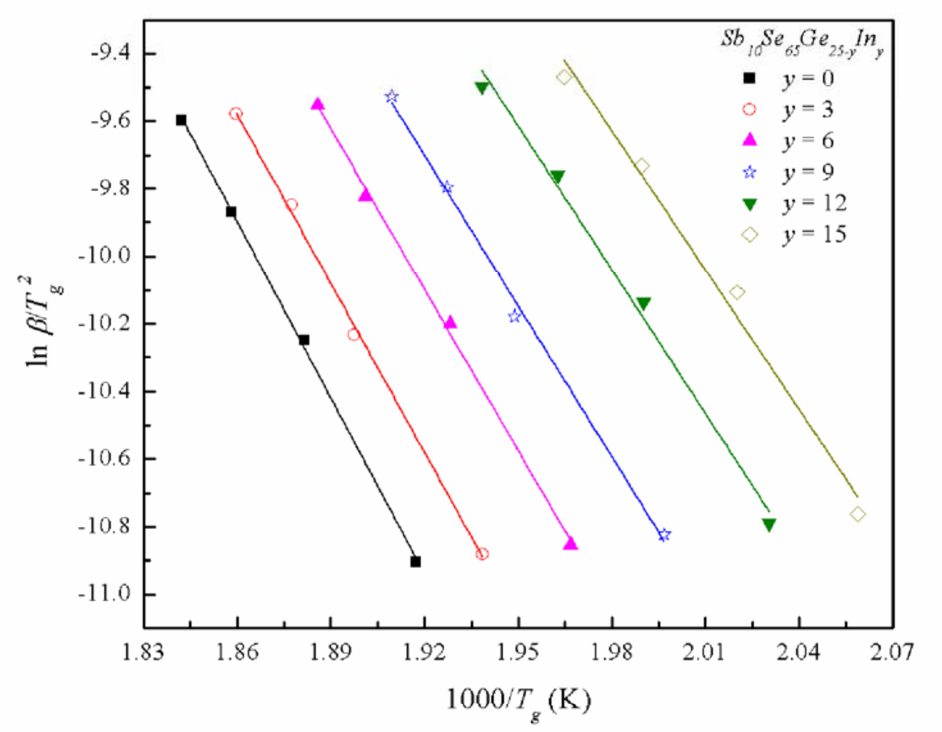

**Figure 4.19** Variation of ln $(\beta/T_g^2)$ with $1000/T_g$ for $Sb_{10}Se_{65}Ge_{25-y}In_y$ system.

The variation in $E_c$ values with *In* at.% has been interpreted in terms of bond energies of the system calculated in section 3.3.2 and given in Table 3.5. For $y = 0$, *Ge–Se* and *Sb–Se* bonds with energies 49.42 kcal/mol and 43.96 kcal/mol respectively have been formed. On addition of *In*, *In–Se* bonds having energy 48.2 kcal/mol start replacing *Ge–Se* bonds in addition to the formation of homopolar *Se–Se* bonds. This results in decrease of cohesive energy, $CE = \sum_i C_i E_i$, where $C_i$ is the distribution of chemical bonds and $E_i$ is the energy associated with bonds. The decrease in the cohesive energy weakens the bonding strength, therefore, decreasing $T_c$ and hence, $E_c$ with *In* content. Therefore, the atoms require less energy to overcome the barrier, decreasing the stability [85].

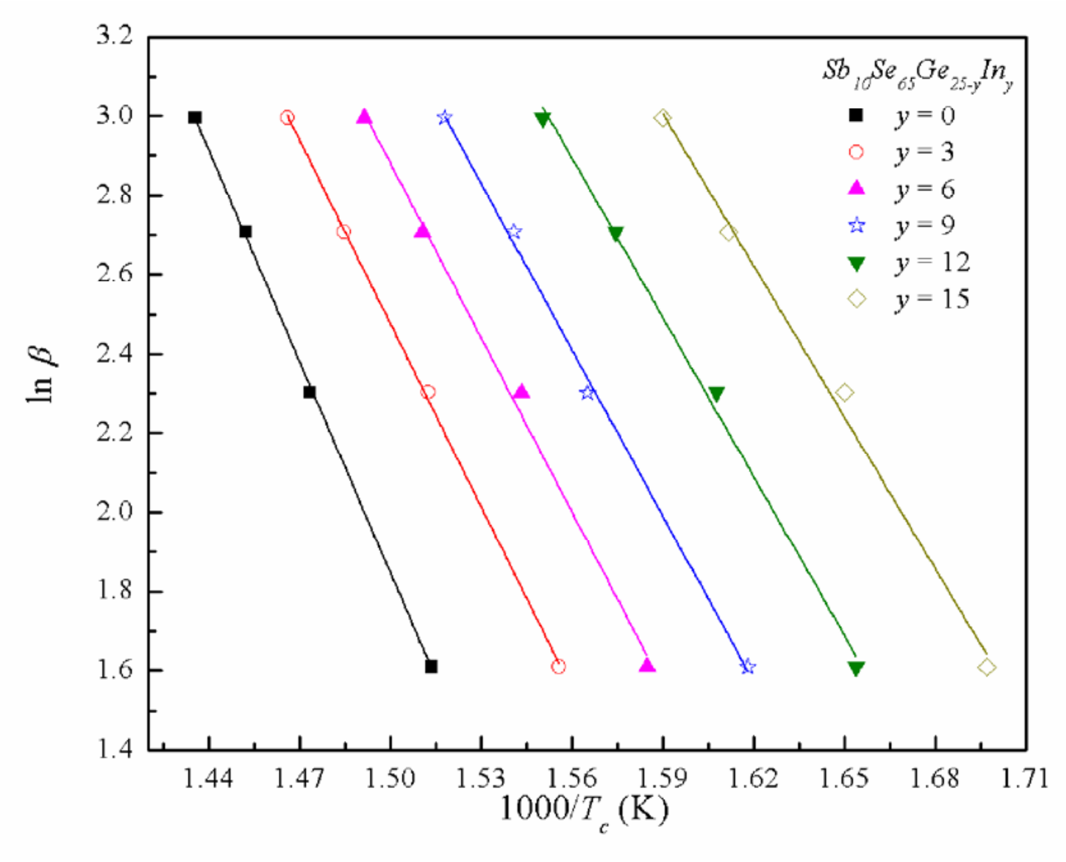

**Figure 4.20** Plot of ln $\beta$ *vs.* $1000/T_c$ for $Sb_{10}Se_{65}Ge_{25-y}In_y$ system.

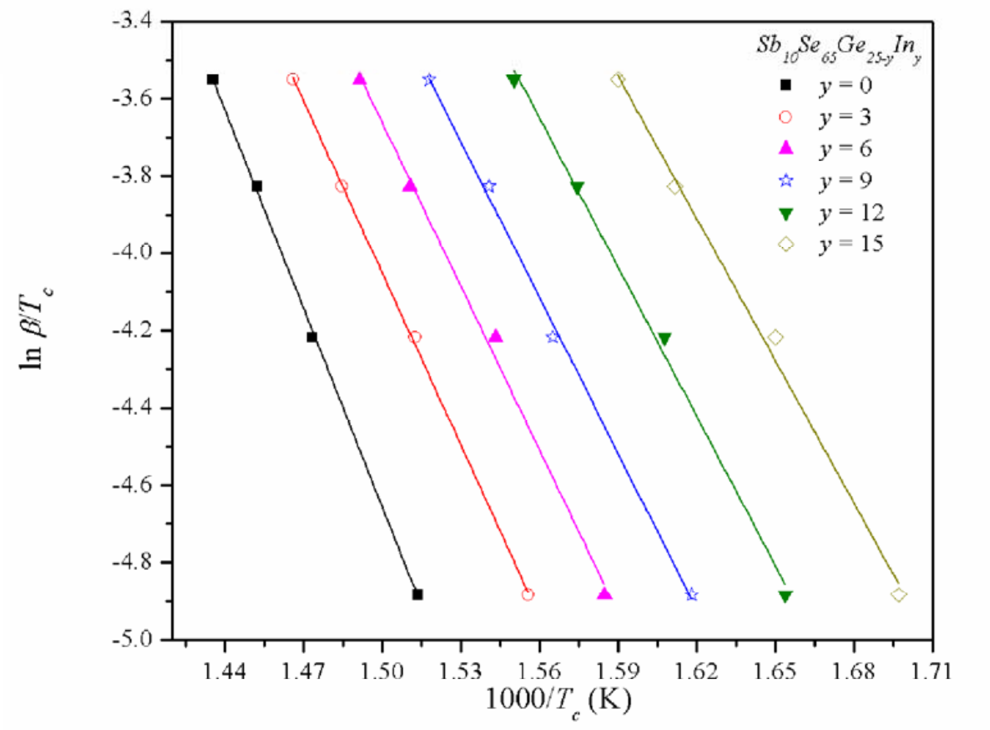

**Figure 4.21** Variation of ln ($\beta/T_c$) with $1000/T_c$ for $Sb_{10}Se_{65}Ge_{25-y}In_y$ system.

## 4.4 Conclusion

For $Sb_{10}Se_{90-x}Ge_x$ glass system $T_g$, $T_c$ and $T_m$ increase to maximum for $x = 25$ at.% *Ge*. This signifies an increase in the rigidity and resistance to devitrification of the glassy system. At $x = 25$, the thermal stability factor ($\Delta T$) and activation energy of crystallization ($E_c$) show maximum which indicates that this composition is thermally stable.

For $Sb_{10}Se_{65}Ge_{25-y}In_y$ alloys all three characteristic temperatures, $T_g$, $T_c$ and $T_m$ decrease with increase in *In* at.%. A decrease in $T_g$ results in decrease of rigidity of the system. $\Delta T$ also decreases with *In* content indicating that the system becomes more prone to crystallization. The probability of atoms to jump to lower metastable states increases as $E_g$ decreases from $y = 0$ to $y = 15$. The heating rate dependence of $T_c$ reveals that $E_c$ decreases due to the replacement of stronger *Ge–Se* bonds with *In–Se* bonds and formation of homopolar *Se–Se* bonds.

# CHAPTER 5

# Optical properties of *Sb-Se-Ge* and *Sb-Se-Ge-In* thin films

- **Sunanda Sharda,** Neha Sharma, Pankaj Sharma and Vineet Sharma, "Band gap and dispersive behavior of Ge alloyed *a-SbSe* thin films using single transmission spectrum" **Materials Chemistry and Physics**, 134 (2012) 158–162.

- **Sunanda Sharda,** Neha Sharma, Pankaj Sharma and Vineet Sharma, "New quaternary *Sb-Se-Ge-In* chalcogenide glasses: Linear and non-linear optical properties" (2013), **Communicated.**

This chapter includes the optical properties of $Sb_{10}Se_{90-x}Ge_x$ and $Sb_{10}Se_{65}Ge_{25-y}In_y$ thin films. Based on transmission spectra, various optical parameters have been calculated and discussed.

## 5.1 Introduction

Various optical properties of chalcogenide glasses such as transparency to IR radiation in the wavelength range 3–5µm and 8–14µm, high refractive index, low optical losses and phonon energies make them efficient materials for switching devices, IR optical fibers and anti reflection coatings [216–218]. Due to their high refractive index and optical band gap lying in the sub–band gap region, chalcogenide glasses are used as core materials for optical fibers which are further used for transmission, especially when short length and flexibility is required.

Chalcogenide glasses have emerged as promising non–linear materials among other glassy systems, like fluorides and oxides, due to their more polarizable covalent bonds, low energy gap and high transmission. Optical fibers exploiting third order electric susceptibility give rise to the optical Kerr effect and thus, are suitable for ultrafast signal processing [219]. These optical fibers have advantages like broadband low–loss transmission and passive operation, not requiring feedback temperature control or electric biasing [219].

*SbSeGe* are promising materials as infrared optical fibers not only due to their high transparency in IR region but because of their large bandgap, low material dispersion, low light scattering and long wavelength multiphonon edge [175, 192]. With *Ge* addition to $Sb_{10}Se_{90}$, at $x = 25$ at.% of *Ge* alloying in $Sb_{10}Se_{90-x}Ge_x$ glassy alloys, a more rigid composition with minimum light scattering losses is obtained. But, a composition with higher percentage of *Ge* increases optical losses in the system. Therefore, the increasing *Ge* concentration has been optimized by alloying $Sb_{10}Se_{65}Ge_{25}$ with *In*.

In this chapter the transmission spectra of the films $Sb_{10}Se_{90-x}Ge_x$ ($x$ = 0, 19, 21, 23, 25, 27) and $Sb_{10}Se_{65}Ge_{25-y}In_y$ ($y$ = 0, 3, 6, 9, 12, 15) have been used for the evaluation of optical parameters. Swanepoel method [161] has been employed to calculate refractive index ($n$) and thickness ($d$) of the films. Optical band gap $E_g^{opt}$ has been estimated using Tauc's extrapolation method [88]. The dispersion of refractive index has been studied in terms of Wemple–DiDomenico single oscillator model [162]. Dielectric constant, loss factor and optical conductivity have also been determined. Third order non–linear susceptibility ($\chi^{(3)}$) and non–linear refractive index ($n_2$) have also been calculated.

## 5.2 Experimental details

The thin films of $Sb_{10}Se_{90-x}Ge_x$ ($x$ = 0, 19, 21, 23, 25, 27) and $Sb_{10}Se_{65}Ge_{25-y}In_y$ ($y$ = 0, 3, 6, 9, 12, 15) glasses have been deposited using vacuum evaporation technique, onto well cleaned glass substrates, employing resistive heating at a vacuum of $10^{-4}$ Pa. The detailed procedure for substrate cleaning and film deposition has been given in section 2.6. The transmission spectra of the deposited films have been obtained using double beam UV–Vis–NIR spectrophotometer (Perkin Elmer Lambda 750) in the spectral range 500–2500 nm at room temperature (300 K). The slit width of 1 nm has been used for measurements.

## 5.3 Results and discussion

### 5.3.1 Optical properties of *Sb–Se–Ge* thin films

The variation of transmission with wavelength in Figure 5.1 shows that the interference fringes are formed with alternate maxima and minima. With the addition of *Ge* to the base $Sb_{10}Se_{90}$ composition, the transmission fringes show a blue shift *i.e.*, a shift towards the smaller wavelength, indicating an increase in the transmission of light through the medium as the *Ge* concentration increases.

The refractive index ($n$) of the *SbSeGe* system has been evaluated using Swanepoel method [161] following the equation (2.6) as described in section 2.7. Figure 5.2 indicates that for shorter wavelengths the refractive index decreases but becomes almost constant at higher wavelengths. The refractive index decreases with an increase in *Ge* content. The refractive index $n = c/v$ increases with decrease in the velocity of light in the medium due to oscillation of negative electron cloud stimulated by incident electromagnetic radiation [220]. Conversely, $n$ decreases with increasing wavelength for the system under study (Figure 5.2). The $n$ values also decrease with the addition of *Ge* to the $Sb_{10}Se_{90}$ system. On substituting *Ge* at the cost of *Se* atoms, the density to atomic radius ratio decreases from $x$ = 19 to 27 at.% *Ge*.

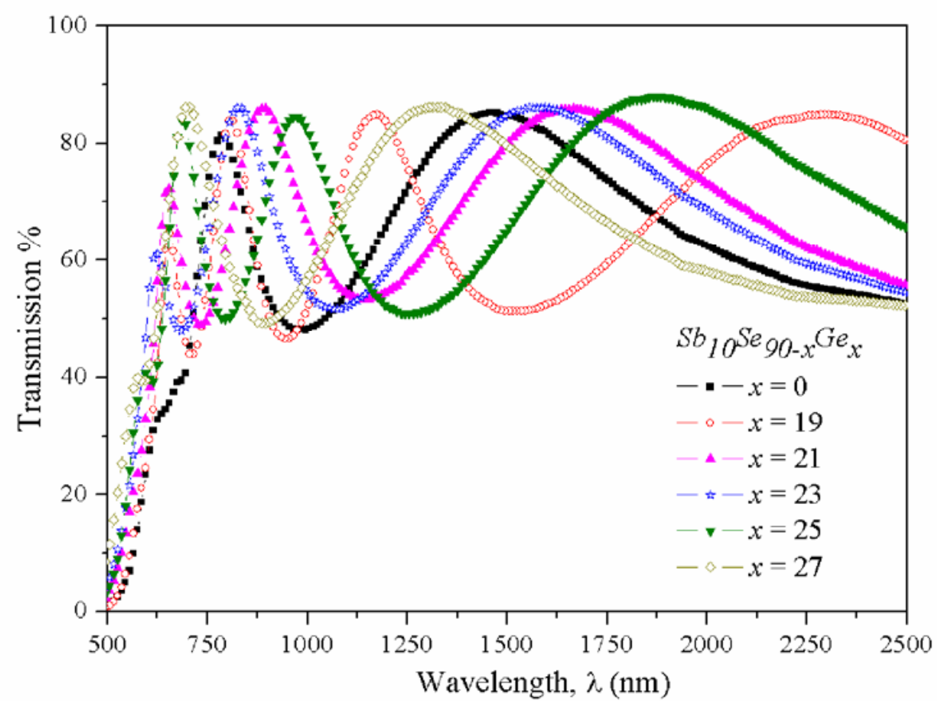

**Figure 5.1** Transmission spectra of $Sb_{10}Se_{90-x}Ge_x$ thin films.

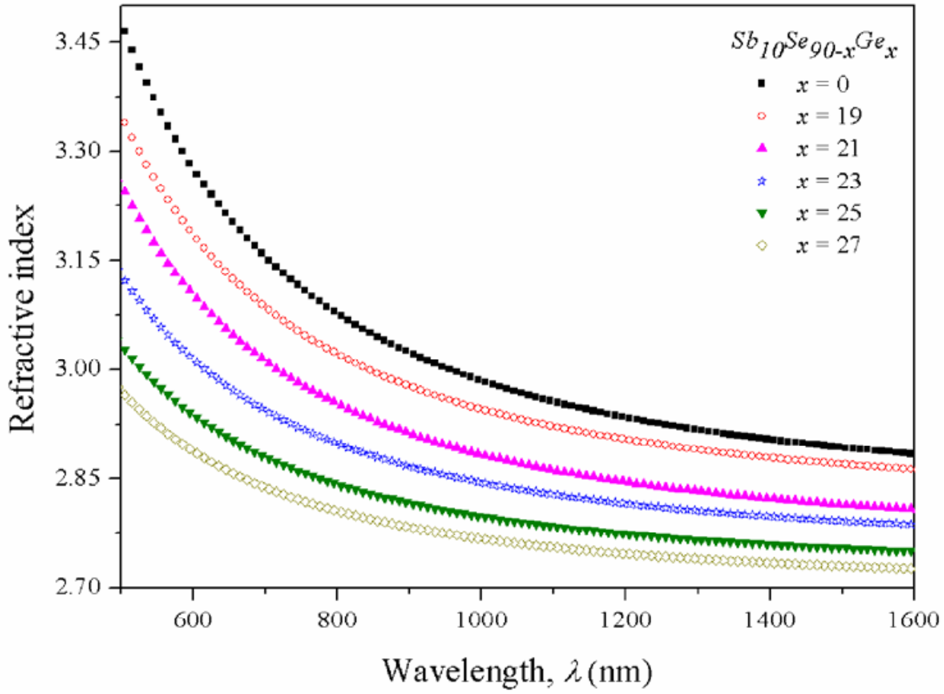

**Figure 5.2** Refractive index *vs.* wavelength for $Sb_{10}Se_{90-x}Ge_x$ thin films.

This drop in the ratio indicates a decrease in the polarizability of the system. The refractive index being proportional to the atomic polarizability leads to a decrease in refractive index with decreasing polarizability of the system [221].

The absorption coefficient ($\alpha$), signifying the number of absorbed photons per incident photon, has been calculated using equation (2.9). The extinction coefficient ($k$) is a measure of fraction of light lost due to scattering and has been evaluated using equation (2.12). The value of $k$ decreases with increase in wavelength as shown in Figure 5.3. This indicates a decrease in the fraction of light scattered and therefore, the transmission increases with increasing wavelength. This loss decreases to a minimum for 25 at.% of *Ge* addition to *a–SbSe*.

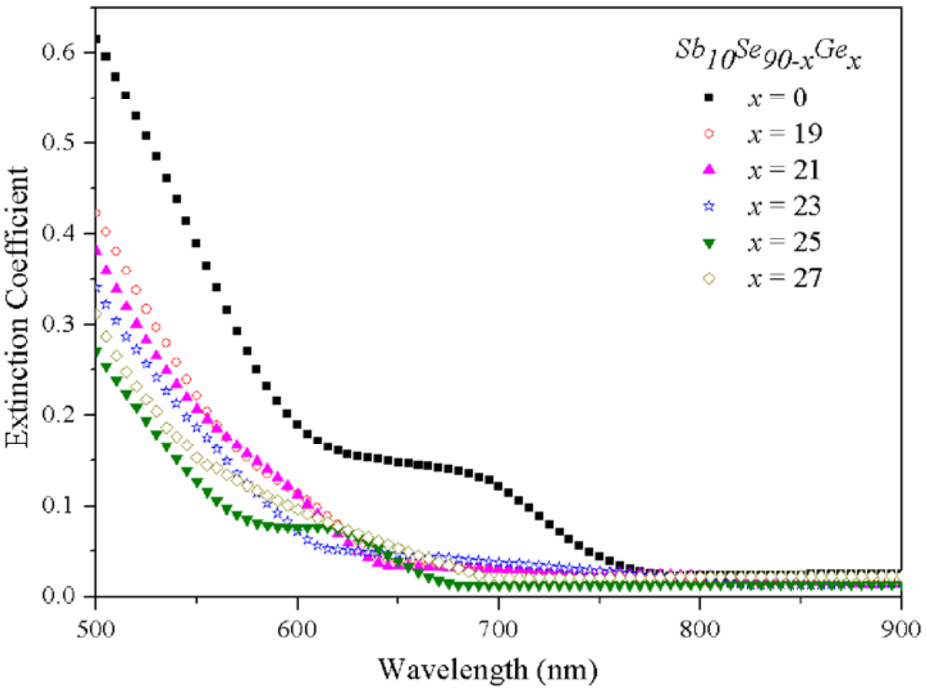

**Figure 5.3** Variation of extinction coefficient with wavelength for $Sb_{10}Se_{90-x}Ge_x$ thin films.

For high absorption region ($\alpha \geq 10^4$ cm$^{-1}$), corresponding to the transitions between extended states in both valence and conduction bands, the value of $\alpha$ is given by Tauc's relation (equation 1.1) [88]. The intercepts on extrapolation with the energy axis give the values of optical band gap ($E_g^{opt}$) (Figure 5.4). The $E_g^{opt}$ increases with increasing *Ge* incorporation attaining a maximum for $x = 25$ and these values have been given in Table 5.1.

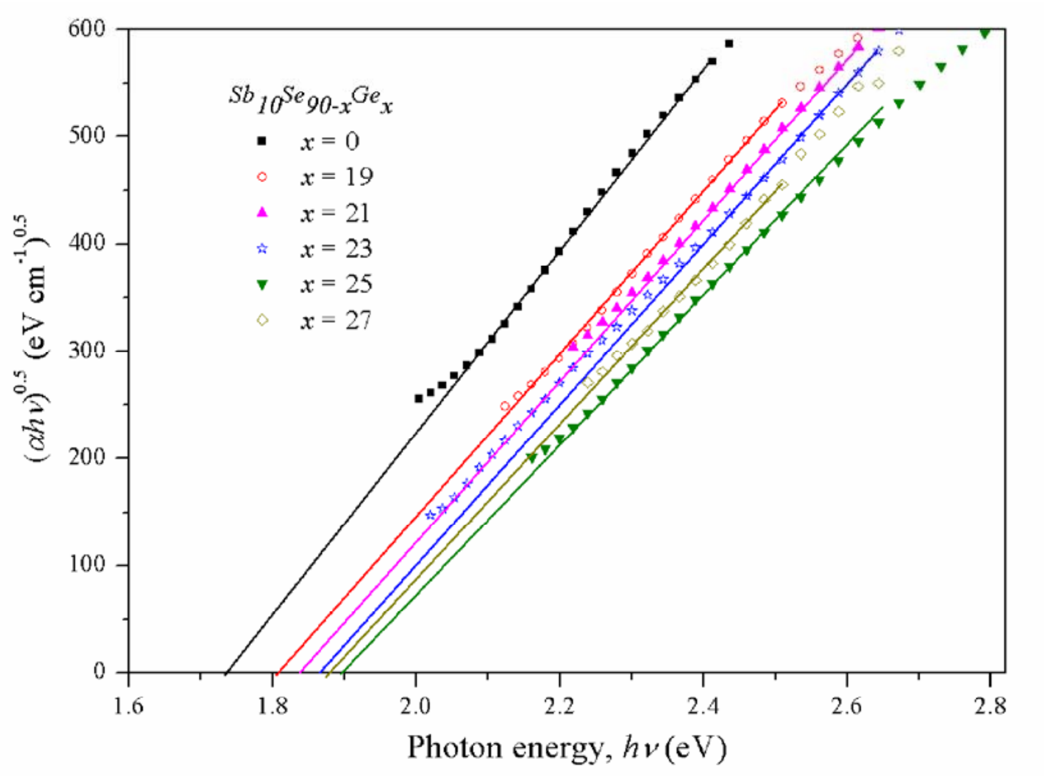

**Figure 5.4** Plot of $(\alpha h\nu)^{0.5}$ *vs.* photon energy for $Sb_{10}Se_{90-x}Ge_x$ thin films.

This observed change in optical band gap (Table 5.1) can be explained on the basis of the structural changes in the glassy network. $Sb_{10}Se_{90}$ contains only $Sb_2Se_3$ structural units which have weak *Sb–Se* bonds. But, with the addition of *Ge*, *Sb–Se* bonds are replaced by stronger *Ge–Se* bonds forming tetrahedral $Ge(Se_{1/2})_4$ units. At $x = 25$, only *Sb–Se* and *Ge–Se* heteropolar bonds exist as obtained in section 3.2.1 (Table 3.3). The cohesive energy of the system has been calculated to be maximum at $x = 25$ (Table 3.3). The values of *CE* decrease above and below this composition due to the replacement of $Sb_2Se_3$ and $Ge(Se_{1/2})_4$ units by weaker *Se–Se* and *Ge–Ge* bonds respectively. Thus, the density of defect states show a minimum for $x = 25$. This results in maximum $E_g^{opt}$ for $x = 25$ at.% *Ge* alloying (Figure 5.5).

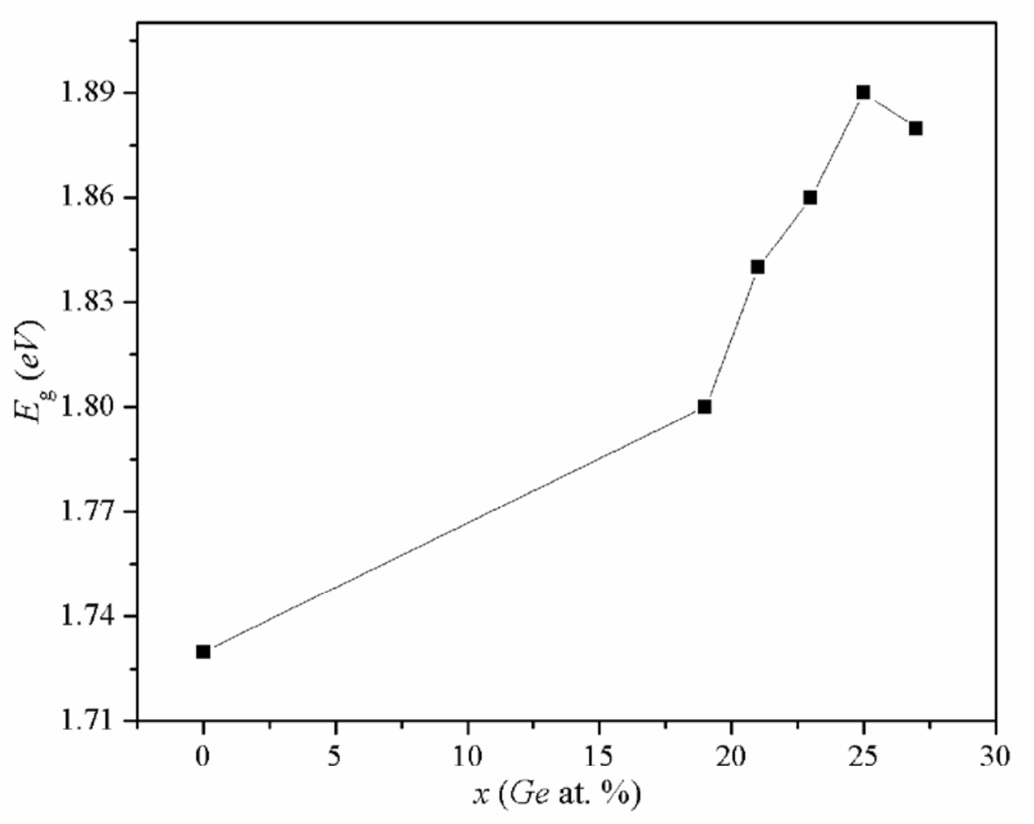

**Figure 5.5** Variation of $E_g^{opt}$ with varying *Ge* at.%

Absorption coefficient ($\alpha$) can be correlated to $E_g^{opt}$ on the basis of density of defect states as $\alpha$ follows the Tauc relation with $p = 2$, a characteristic of indirect band gap. Therefore, $\alpha$ decreases till $x = 25$ and then increases for $x = 27$ due to variation in the bonding arrangements and hence, in the defect states.

The spectral dependence of the refractive index has been fitted to the single oscillator *i.e.* Wemple–DiDomenico model [162]. It suggests a relation between refractive index and single oscillator strength, below the fundamental absorption edge (equation (2.13)). The values of oscillator energy ($E_0$) and oscillator strength ($E_d$) have been determined from the intercept $E_0/E_d$ and slope $(E_0E_d)^{-1}$ respectively of the fitted straight lines in Figure 5.6 and are given in Table 5.1. The values of static refractive index ($n_0$) *i.e.* refractive index when $h\nu = 0$, have been calculated from $E_0$ and $E_d$ values (Table 5.1).

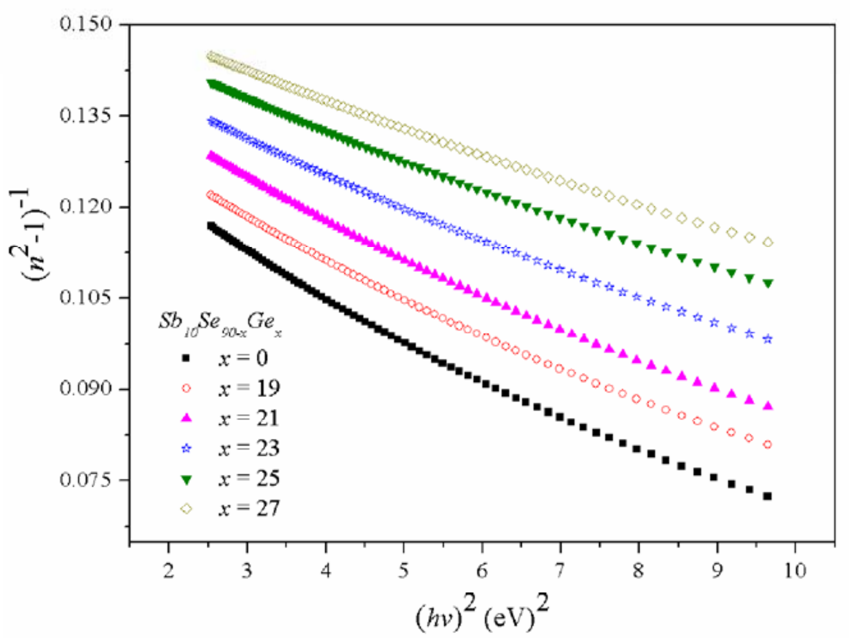

**Figure 5.6** Plot of $(n^2-1)^{-1}$ *vs.* $(h\nu)^2$ for $Sb_{10}Se_{90-x}Ge_x$ thin films.

The static refractive index ($n_0$) is the lower limit of refractive index and represents the response of the material to DC electric field. The values of $E_0$ and $E_d$ increase, while $n_0$ decreases as the *Ge* alloying increases in the base system.

**Table 5.1** Values of optical band gap ($E_g^{opt}$), oscillator energy ($E_0$), oscillator strength ($E_d$), static refractive index ($n_0$), theoretically calculated $E_d$, real part of dielectric constant ($\varepsilon_r$), imaginary part of dielectric constant ($\varepsilon_i$) and loss tangent (*tanδ*) for $Sb_{10}Se_{90-x}Ge_x$ thin films.

| $x$ | $E_g^{opt}$ (eV) | $E_0$ (eV) | $E_d$ (eV) | $n_0$ | $E_d$ (eV) (theoretical) | $\varepsilon_r$ | $\varepsilon_i$ | $\tan\delta$ |
|---|---|---|---|---|---|---|---|---|
| 0 | 1.73 | 4.51 | 34.30 | 2.93 | 15.73 | 11.06 | 2.27 | 0.2201 |
| 19 | 1.80 | 4.77 | 35.21 | 2.89 | 22.73 | 10.46 | 1.22 | 0.1266 |
| 21 | 1.84 | 4.87 | 34.26 | 2.83 | 23.36 | 9.90 | 1.16 | 0.1243 |
| 23 | 1.86 | 5.31 | 36.23 | 2.80 | 24.01 | 9.29 | 0.99 | 0.1150 |
| 25 | 1.89 | 5.66 | 37.28 | 2.75 | 24.68 | 8.80 | 0.63 | 0.0781 |
| 27 | 1.88 | 5.95 | 38.29 | 2.73 | 25.38 | 8.48 | 0.82 | 0.0996 |

The oscillator energy $E_0$ corresponds to the distance between the centers of gravity of the valence and conduction bands. It is the 'average' energy gap and approximately scales with Tauc's gap, $E_g^{opt}$ *i.e.* $E_0 \approx 2\ E_g^{opt}$ [222]. Therefore, $E_0$ can be related to the bond energies of the different chemical bonds present in the system as the optical band gap is a bond sensitive property. $E_0$ increases as *Ge* at.% increases from $x$ = 19 to 27 at.% which is consistent with Tanaka's relation [222]. The dispersion energy or oscillator strength, $E_d$, also follows a simple empirical relation (equation (2.14)) The total number of valence electrons per anion ($N_e$), for the $Sb_{10}Se_{90}$ binary system is, $N_e = (5\times 10 + 6\times 90)/90 \approx 6.556$. The base composition can be written as $(Sb_1Ge_0)_{10}Se_{90}$. Considering a hypothetical cation $Sb_1Ge_0$, cation coordination number ($N_c$) can now be calculated as, $N_c = (3\times 1 + 4\times 0) = 3$. Similarly, for $Sb_{10}Se_{71}Ge_{19}$ composition, $N_e = (5\times 10 + 6\times 71 + 4\times 19)/71 \approx 7.775$. Rewriting the $Sb_{10}Se_{71}Ge_{19}$ composition in the form $(Sb_{0.345}Ge_{0.655})_{29}Se_{71}$, the hypothetical cation is $Sb_{0.345}Ge_{0.655}$. Therefore, $N_c = (3\times 0.345 + 4\times 0.655) \approx 3.655$.

The incorporation of *Ge* into the $Sb_{10}Se_{90-x}Ge_x$ glass system increases the oscillator strength ($E_d$) indicating that one of the parameter ($N_c$) in the empirical relation is increasing. *Ge* addition may change the nature of chemical bonding into more ionic but, this cannot be the major factor behind the increase in $E_d$, since this will decrease $\beta'$. In WDD model [162], $\beta'$ is assumed to be a constant. The cation coordination number and total number of valence electrons per anion are increasing with *Ge* incorporation in the base system. The cation coordination number, $N_c$, can be reasonably assumed to affect the oscillator strength with an increase in *Ge* concentration. The overall increase observed in the values of $E_d$ and consequently in $N_c$ suggests a greater interaction between the structural layers [221], which is consistent with the increase in theoretically calculated structural compactness of $Sb_{10}Se_{90-x}Ge_x$ system (Table 3.2). The compactness of the *SbSeGe* system increases due to change in the structure of the glass network with *Ge* addition. *Ge* breaks the polymeric structure of $Sb_{10}Se_{90}$ system forming tetrahedral $Ge(Se_{1/2})_4$ units, increasing the rigidity of the system and hence, compactness. The decrease in $n_o$ with increasing *Ge* content may be explained using the fundamental Kramers–Kronig [101] relationship. Accordingly, the relation, ( $n(0)-1=\frac{1}{2\pi^{2}}\int_{0}^{\infty}\alpha\, d\lambda$ ), predicts a blue shift in the absorption spectrum leading to a decrease in refractive index.

The refractive index and oscillator parameter variation with *Ge* addition has been further analyzed by considering the dielectric behaviour of the *SbSeGe* system. The values of $\varepsilon_r$, $\varepsilon_i$ and *tanδ* have been calculated using equations (2.16), (2.17) and (2.18) respectively and are given in Table 5.1. The values of $\varepsilon_r$ decrease for $x = 0$ to $x = 27$ whereas $\varepsilon_i$ and *tanδ* decrease to a minimum for $x = 25$ and increases for $x = 27$. To get a better idea of the effect of *Ge* addition to *SbSe* on the dielectric loss, the optical conductivity ($\sigma$) has been calculated. The optical conductivity of the present system has been calculated using equation (2.19). Figure 5.7 shows that the optical conductivity shifts towards lower photon energy with a minimum at $x = 25$ followed by an increase for $x = 27$.

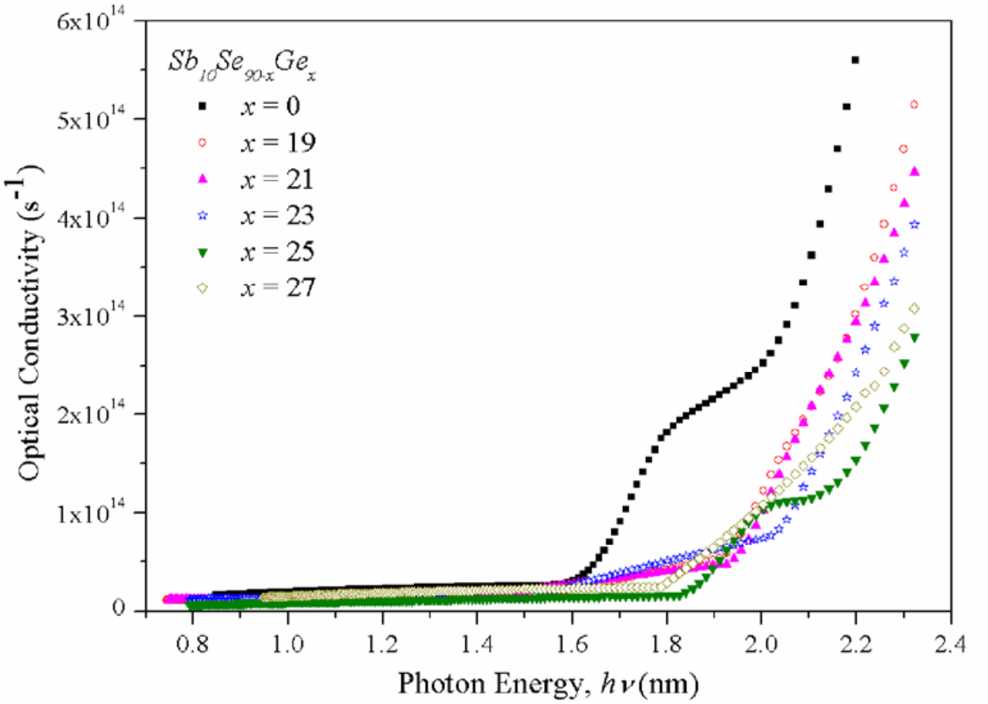

**Figure 5.7** Variation of optical conductivity with $h\nu$ for $Sb_{10}Se_{90-x}Ge_x$ thin films.

The dielectric dispersion gives an idea about the dielectric losses which in turn is useful for the determination of electronic structure or defects in the system. The electron transfer, in chalcogenide glasses, from one chain to another form dangling bonds *i.e.* the paired $D^-$ and $D^+$ defect states [223]. *Ge* alloying in the *SbSe* system decreases the charge defects and hence, the number of dipoles to minimum for 25 at.% of *Ge* addition hence, decreasing the dielectric parameters. The addition of *Ge* in excess of 25 at.% increases the charged defects, enhancing the dielectric parameters. The optical conductivity is related to absorption coefficient of the system. So, $\sigma$ varies in accordance with $\alpha$ due to a change in the density of defect states in the forbidden gap of the system as the *Ge* alloying concentration increases in the *SbSe* base system.

For the assessment of non–linear optical properties of *SbSeGe* system, two models, as proposed by Tichy–Ticha [224] and Fournier Snitzer [225] have been used. Third order non–linear susceptibility ($\chi^{(3)}$) is produced by excitation in the transparent frequency region well below $E_g^{opt}$. According to Miller's generalized rule $\chi^{(3)} = A(\chi^{(1)})^4$ where $A = 1.70 \times 10^{-10}$ (when $\chi^{(3)}$ is measured in esu) and $\chi^{(1)}$ is linear optical susceptibility, which for the case of chalcogenide glasses is $\chi^{(1)} = (n^2 - 1)/4\pi$ [224]. Then for $h\nu \rightarrow 0$,

$$\chi^{(3)} = \frac{A}{(4\pi)^4}\left(n_0^2 - 1\right)^4 \tag{5.2}$$

The values of $\chi^{(3)}$ decrease as *Ge* concentration increases (Table 5.2).

**Table 5.2** Values of third order non–linear susceptibility ($\chi^{(3)}$), non–linear refractive index ($n_2$, Tichy–Ticha) and density of polarizable constituents ($N^*$) for $Sb_{10}Se_{90-x}Ge_x$ thin films.

| $x$ | $\chi^{(3)} \times 10^{-11}$ (esu) | $n_2 \times 10^{-10}$ (esu) [Tichy–Ticha] | $N^* \times 10^{22}$ |
|---|---|---|---|
| 0 | 2.26 | 2.91 | 3.60 |
| 19 | 2.00 | 2.60 | 3.73 |
| 21 | 1.65 | 2.19 | 3.74 |
| 23 | 1.50 | 2.01 | 3.76 |
| 25 | 1.27 | 1.74 | 3.77 |
| 27 | 1.18 | 1.63 | 3.78 |

The value of non–linear refractive index ($n_2$) is related to $\chi^{(3)}$ as [224],

$$n_2 = \frac{12\pi\chi^{(3)}}{n_0} \tag{5.3}$$

The values of non–linear refractive index (in esu) (Table 5.2) have been found to decrease with *Ge* concentration.

Fournier and Snitzer proposed another relation to calculate the value of $n_2$ [225],

$$n_2 = \frac{(n^2+2)^2(n^2-1)}{48\pi n N^*}\frac{E_d}{(E_0)^2} \tag{5.4}$$

where $N^*$ is the density of polarizable constituents (Table 5.2). The variation of $n_2$ with photon energy ($h\nu$) has been shown in Figure 5.8. The non–linear refractive index increases with increase in $h\nu$ and decreases with *Ge* at. % in $Sb_{10}Se_{90-x}Ge_x$ alloys (Figure 5.8).

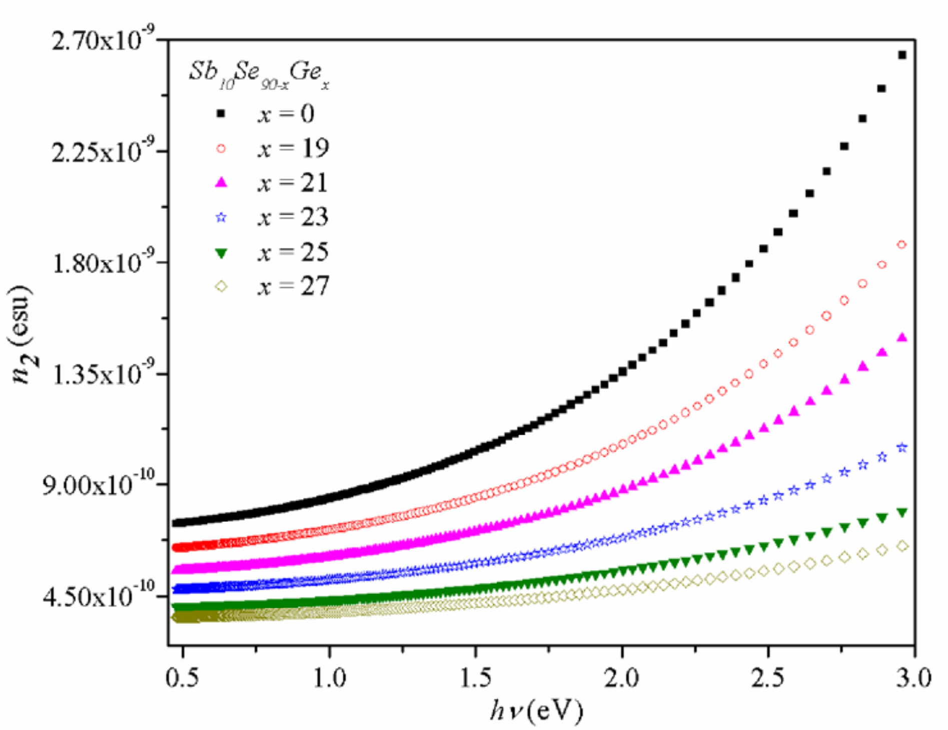

**Figure 5.8** Variation of $n_2$ (Fournier and Snitzer) with $h\nu$ for $Sb_{10}Se_{90-x}Ge_x$ thin films.

### 5.3.2 Optical properties of *Sb–Se–Ge–In* thin films

The transmission spectra for $Sb_{10}Se_{65}Ge_{25-y}In_y$ thin films (Figure 5.9) show a shift of absorption edge towards higher wavelength indicating a red shift with the increase in *In* content. The values of *n* and *k* have been calculated using Swanepoel method [161]. The complex refractive index for uniform thickness is given by $n^* = n - ik$. The value of *k* is related to absorption coefficient in the strong absorption region as, $k = \alpha\lambda/4\pi$. It is observed from Figure 5.10, that *n* decreases with increasing wavelength showing normal dispersion.

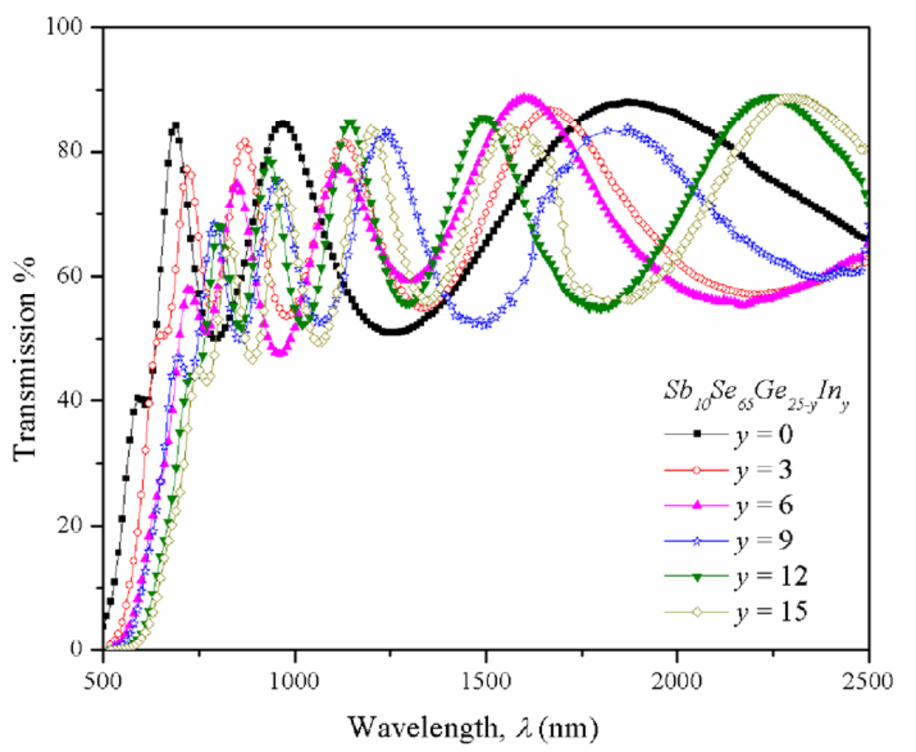

**Figure 5.9** Transmission spectra of $Sb_{10}Se_{65}Ge_{25-y}In_y$ thin films.

With *In* addition *n* increases, which can be explained using Lorentz–Lorentz relation [101]. According to this relation, larger the atomic radius more will be the polarizability and hence, larger will be the refractive index. Since, *Ge* (1.22Å) [188] is being replaced by larger *In* (1.50 Å) [188] atoms so, there is an increase in the value of *n*.

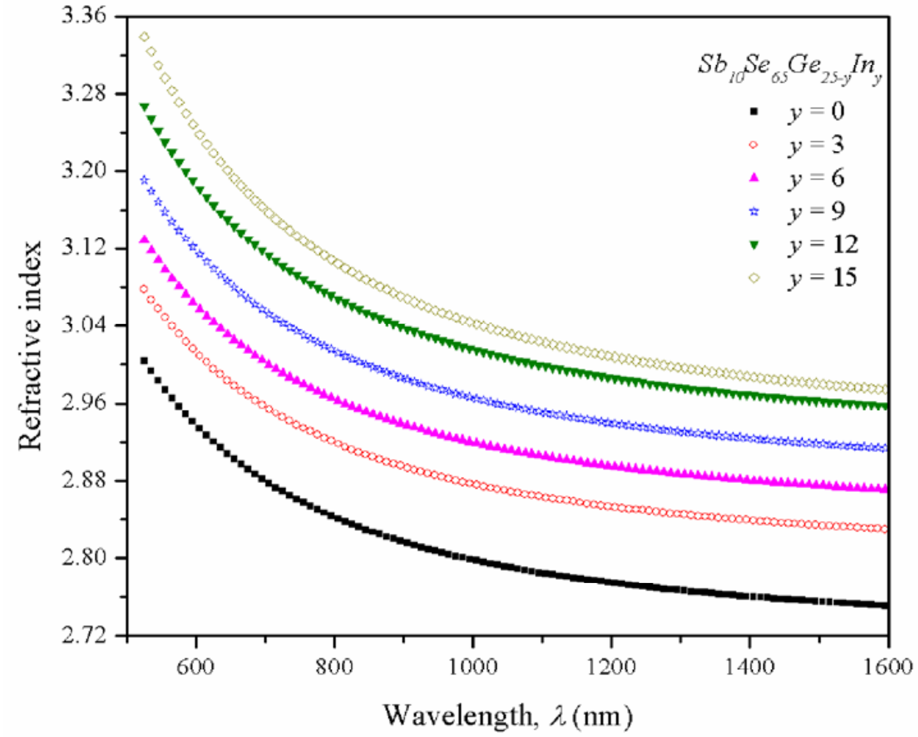

**Figure 5.10** Plot of refractive index *vs*. wavelength for $Sb_{10}Se_{65}Ge_{25-y}In_y$ thin films.

A red shift in the transmission spectrum must necessarily give an increased value of refractive index, following the fundamental Kramers–Kronig relation [101]. The value of *k* increases with an increase in wavelength (Figure 5.11) which indicates that there is an increase in the fraction of light scattered in the interference free region. This loss increases with increase in *In* concentration from $y = 0$ to $y = 15$.

The optical band gap has been determined from relation proposed by Tauc, equation (1.1) [88]. The intercepts on extrapolation with the energy axis give the values of $E_g^{opt}$ (Figure 5.12).

The value of $E_g^{opt}$ decreases with increase in *In* concentration (Table 5.3). With the addition of *In* to $Sb_{10}Se_{65}Ge_{25}$, stronger *Ge–Se* bonds are replaced by *In–Se* bonds and unsaturated *Se–Se* bonds are also formed as calculated theoretically in Table 3.4.

The unsaturated *Se–Se* bonds give rise to defect states producing localized states which are responsible for the decrease in $E_g^{opt}$ values with *In* addition (Figure 5.13).

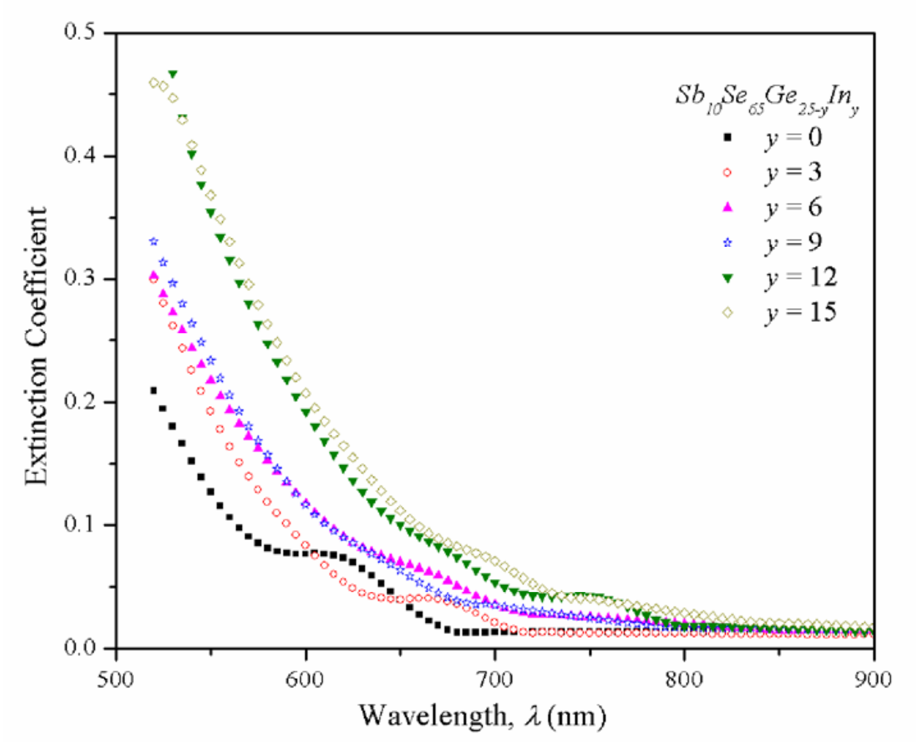

**Figure 5.11** Extinction coefficient with wavelength for $Sb_{10}Se_{65}Ge_{25-y}In_y$ thin films.

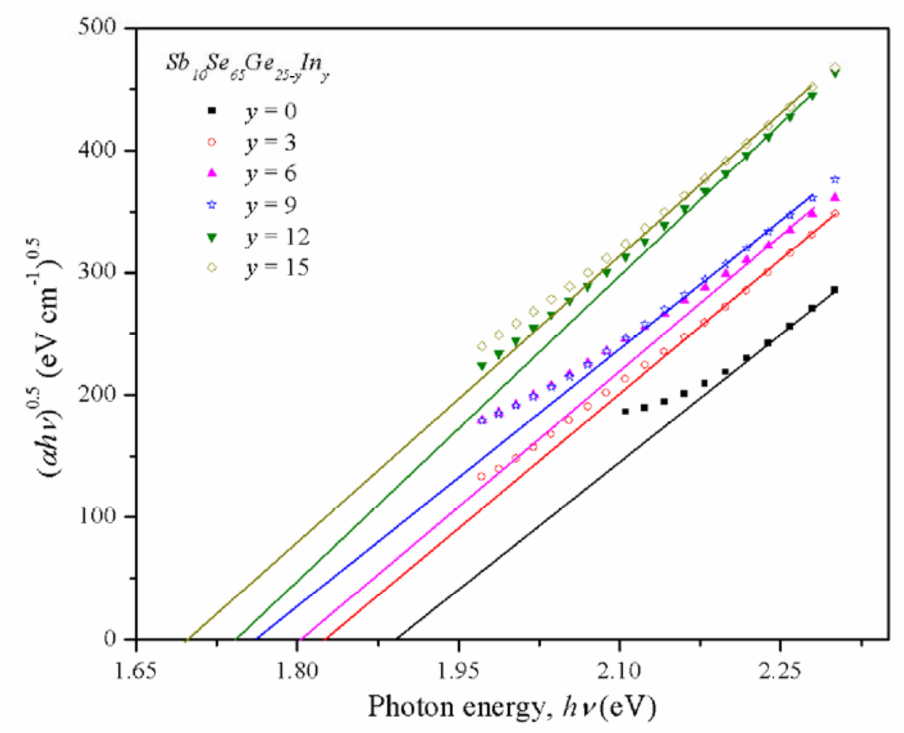

**Figure 5.12** Plot of $(\alpha h\nu)^{0.5}$ *vs.* photon energy for $Sb_{10}Se_{65}Ge_{25-y}In_y$ thin films.

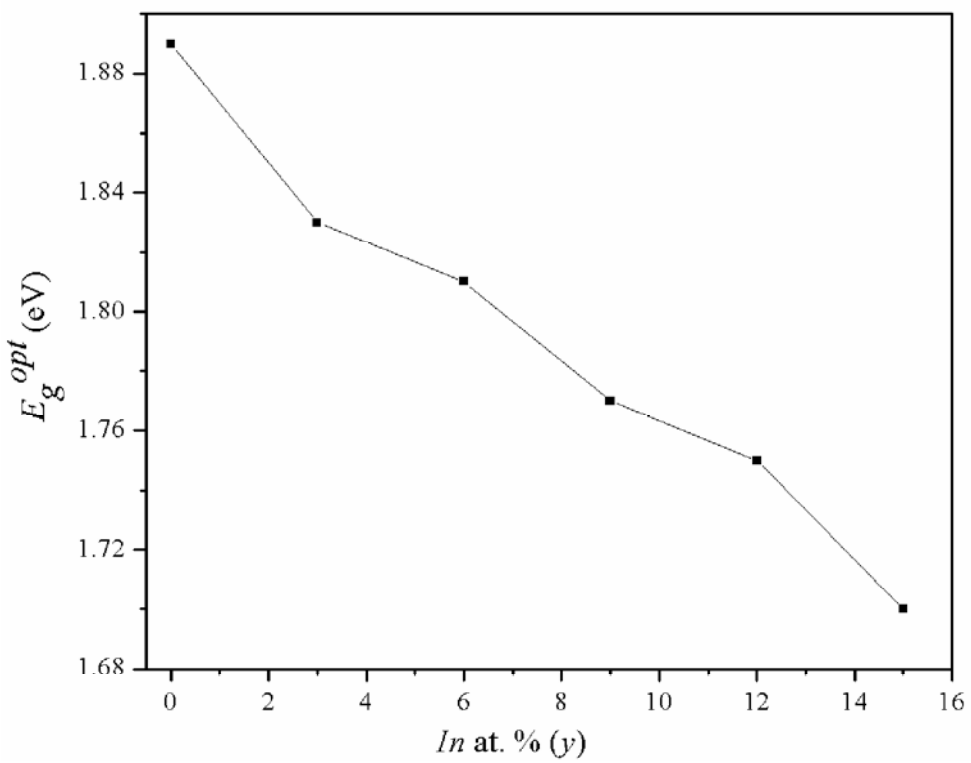

**Figure 5.13** Variation of $E_g^{opt}$ with varying *In* at.%.

The dispersion of refractive index has been evaluated using Wemple–DiDomenico single oscillator model (Figure 5.14) [162]. The deviation from linearity is a result of proximity of the band edge to Fermi level at higher photon energies [226]. $E_0$ is the average energy gap and approximately scales with the Tauc gap *i.e.* $E_0 \approx 2\ E_g^{opt}$ [222]. Therefore, $E_0$ also decreases with increase in *In* alloying concentration (Table 5.3). Static refractive index ($n_0$), *i.e.* refractive index when $h\nu \rightarrow 0$, has also been calculated using $E_0$ and $E_d$ values. The value of $n_0$ increases due to the formation of more polarizable *In–Se* bonds in the system.

The loss tangent and optical conductivity have also been calculated for $Sb_{10}Se_{65}Ge_{25-y}In_y$ (equation 2.18 and 2.19). With the addition of *In* concentration real and imaginary parts of dielectric constant, $\varepsilon_r$, $\varepsilon_i$, and loss tangent, *tanδ*, increases (Table 5.3). This may be attributed to the fact that *In* addition increases the charge defects and hence, the number of dipoles to maximum which causes an increase in the value of the dielectric parameters.

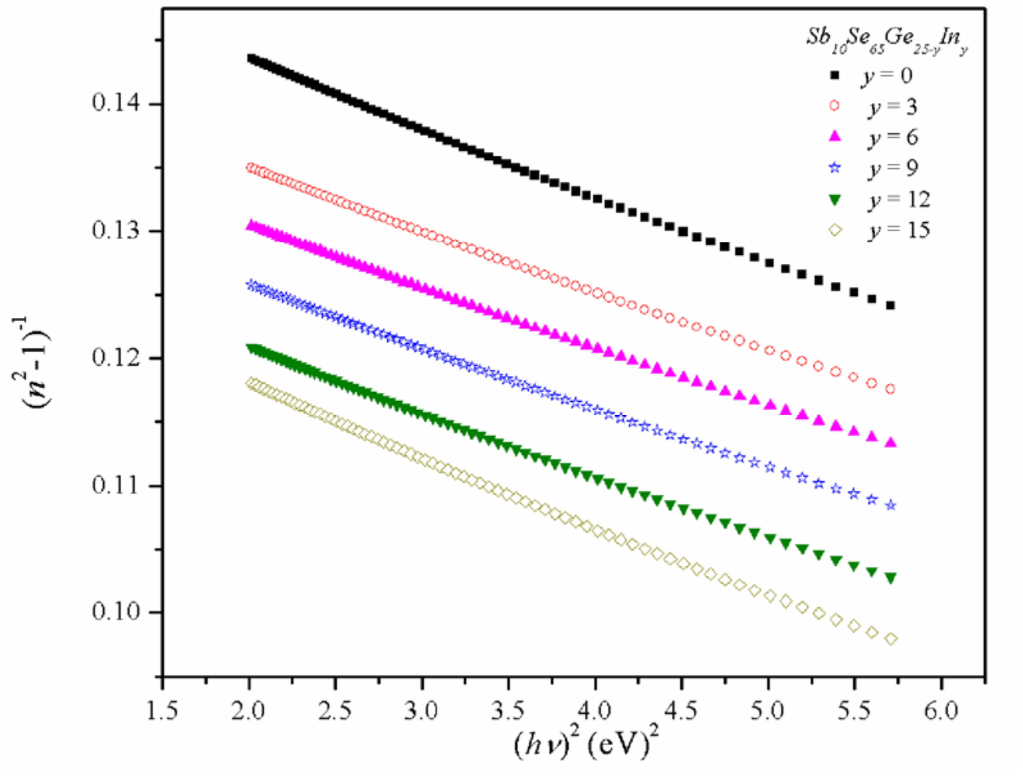

**Figure 5.14** Plot of $(n^2-1)^{-1}$ *vs.* $(h\nu)^2$ for $Sb_{10}Se_{65}Ge_{25-y}In_y$ thin films.

**Table 5.3** Values of optical band gap ($E_g^{opt}$), oscillator energy ($E_0$), oscillator strength ($E_d$), static refractive index ($n_0$), real part of dielectric constant ($\varepsilon_r$), imaginary part of dielectric constant ($\varepsilon_i$) and loss tangent ($tan\delta$) for $Sb_{10}Se_{65}Ge_{25-y}In_y$ thin films.

| $y$ | $E_g^{opt}$ (eV) | $E_0$ (eV) | $E_d$ (eV) | $n_0$ | $\varepsilon_r$ | $\varepsilon_i$ | $tan\delta$ |
|---|---|---|---|---|---|---|---|
| 0 | 1.89 | 5.66 | 37.28 | 2.75 | 8.80 | 0.63 | 0.0781 |
| 3 | 1.83 | 5.51 | 38.20 | 2.82 | 9.23 | 0.99 | 0.1077 |
| 6 | 1.81 | 5.47 | 39.16 | 2.86 | 9.53 | 1.19 | 0.1255 |
| 9 | 1.77 | 5.34 | 39.57 | 2.90 | 9.90 | 1.29 | 0.1309 |
| 12 | 1.75 | 5.15 | 39.42 | 2.94 | 10.30 | 2.03 | 0.1972 |
| 15 | 1.70 | 4.84 | 37.57 | 2.96 | 10.71 | 2.17 | 0.2029 |

Figure 5.15 shows that the optical conductivity shifts towards lower photon energy with an increase in value from $y = 0$ to $y = 15$. The optical conductivity increases with *In* alloying concentration due to change in density of defect states in the forbidden gap of the system.

The third order susceptibility decreases while non–linear refractive index calculated by Tichy–Ticha approach (equation (5.3)) increases with *In* content, (Table 5.4). The non–linear refractive index using Fournier and Snitzer approach [225] (equation (5.4)) has been plotted with photon energy in Figure 5.16. The value of density of polarizable constituents ($N^*$) has been given in Table 5.4 and shows a decrease with increase in *In* concentration.

**Table 5.4** Values of third order non–linear susceptibility ($\chi^{(3)}$), non–linear refractive index ($n_2$, Tichy–Ticha) and density of polarizable constituents ($N^*$) for $Sb_{10}Se_{65}Ge_{25-y}In_y$ thin films.

| ***x*** | **$\chi^{(3)} \times 10^{-11}$ (esu)** | **$n_2 \times 10^{-10}$ (esu) [Tichy–Ticha]** | **$N^* \times 10^{22}$** |
|---|---|---|---|
| 0 | 2.26 | 1.74 | 3.77 |
| 3 | 2.00 | 2.13 | 3.76 |
| 6 | 1.65 | 2.39 | 3.74 |
| 9 | 1.50 | 2.68 | 3.73 |
| 12 | 1.27 | 2.99 | 3.72 |
| 15 | 1.18 | 3.16 | 3.70 |

An increase in $n_2$ can be correlated to $E_g^{opt}$ by the relation, $n_2 \propto 1/(E_g^{opt})^4$ [227], according to which $n_2$ increases as the $E_g^{opt}$ value decreases on *In* addition. This shows the results to be consistent with the given relation.

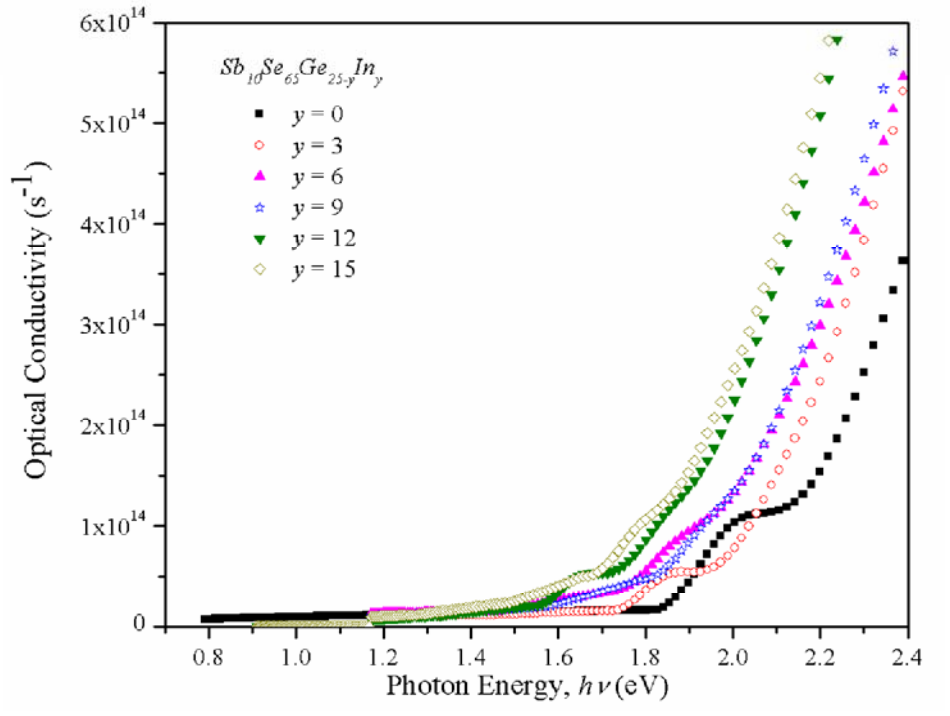

**Figure 5.15** Variation of optical conductivity with *hν* for $Sb_{10}Se_{65}Ge_{25-y}In_y$ thin films.

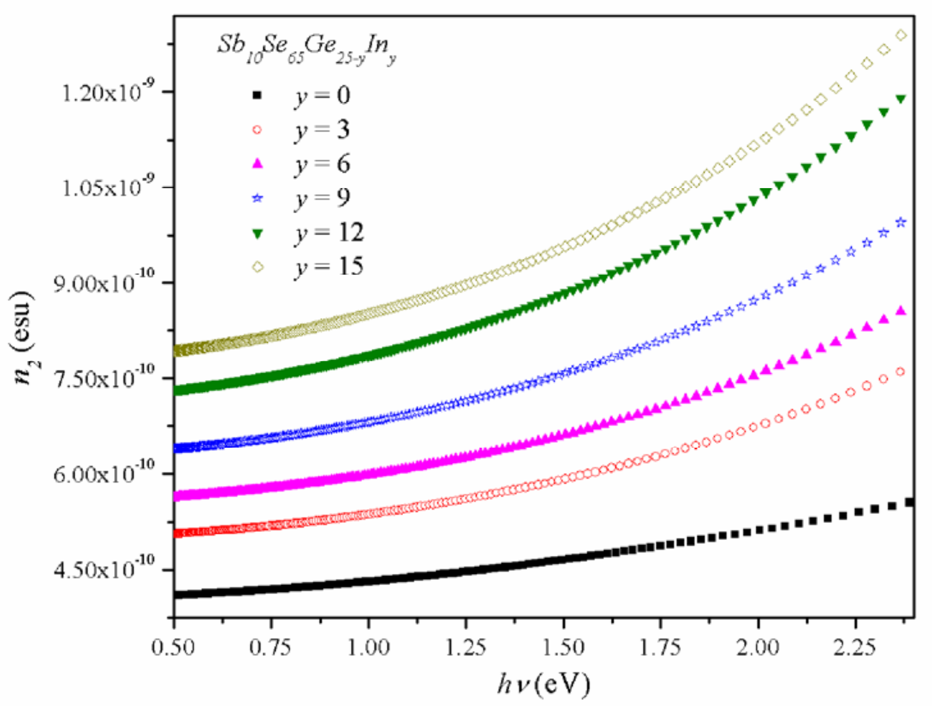

**Figure 5.16** Variation of non–linear refractive index ($n_2$) (Fournier and Snitzer) with *hν* for $Sb_{10}Se_{65}Ge_{25-y}In_y$ thin films.

## 5.4 Conclusion

For $Sb_{10}Se_{90-x}Ge_x$ glass system the refractive index decreases with increasing $Ge$ at.%. The defect states density decreases to a minimum for the stoichiometric composition $Sb_{10}Se_{65}Ge_{25}$ with maximum $E_g^{opt}$. This results in a minimum for extinction coefficient, loss tangent and optical conductivity at $x = 25$ at.% of $Ge$ addition. The values of $E_0$ and $E_d$ increase while that of static refractive index decreases with $Ge$ alloying. The non–linear refractive index decreases with increase in $Ge$ additive.

For $Sb_{10}Se_{65}Ge_{25-y}In_y$ glass system the refractive index increases due the formation of more polarizable $In–Se$ bonds. Optical band gap decreases on $In$ addition due to the formation of unsaturated $Se–Se$ bonds. The values of $E_0$ decrease while $E_d$, static refractive index and dielectric parameters increase with $In$ alloying concentration. The values of $\chi^{(3)}$ and non–linear refractive indices increase with $In$ content.

# CHAPTER 6

## Summary

Transparency in the IR region and phase change property of chalcogenide glasses makes them an important class of materials. Two glassy systems *viz.* $Sb_{10}Se_{90-x}Ge_x$ ($x$ = 0, 19, 21, 23, 25, 27) and $Sb_{10}Se_{65}Ge_{25-y}In_y$ ($y$ = 0, 3, 6, 9, 12, 15) have been investigated for their physical, structural, thermal and optical properties. Bulk samples of the glasses have been prepared using melt quench technique. The amorphous nature of the samples has been confirmed from x–ray diffraction. Thin films of the glasses have been deposited using vacuum evaporation technique.

The structure of the chalcogenide glass system $Sb_{10}Se_{90-x}Ge_x$ becomes rigid as the *Ge* content is increased in binary system $Sb_{10}Se_{90}$. The addition of *Ge* induces larger degree of crosslinking in the glass. This enhances the density and compactness of the system. For $x = 25$, R (deviation in stoichiometry) = 1 *i.e.* only heteropolar bonds are formed indicating a complete 3-dimensional network leading to a maximum for glass transition temperature and cohesive energy.

With *In* addition to $Sb_{10}Se_{65}Ge_{25}$ the crosslinking of the system decreases. The system becomes denser with increase in *In* at.% which increases compactness of the system. With *In* addition, parameter R > 1 indicating the formation of *Se–Se* bonds which causes a decrease in glass transition temperature and cohesive energy.

The far–IR study shows that the structural units contain *Sb–Se* bonds, $Se_8$ rings and *Se* polymeric chains for $x = 0$. The *Ge* addition to $Sb_{10}Se_{90}$ gives rise to new *Ge–Se* modes along with $SbSe_3$ units and $Se_8$ rings. However, $Se_8$ rings almost disappear for $x = 25$, which is the most crosslinked composition.

The *In* addition to $Sb_{10}Se_{65}Ge_{25-y}In_y$ leads to structural changes with the formation of $InSe_4$, $In_2Se_3$ units and *In–Se* bonds. The absorption peak at 195 cm$^{-1}$ has been assigned to *In–In* bonds, which is in accordance with theoretically calculated wavenumber value.

For $Sb_{10}Se_{90-x}Ge_x$ glass system $T_g$, $T_c$ and $T_m$ increase to maximum for $x = 25$ at.%. At $x = 25$, the thermal stability factor ($\Delta T$) and activation energy of crystallization ($E_c$) show maximum which indicates that this composition is thermally stable with a complete three dimensional network.

For $Sb_{10}Se_{65}Ge_{25-y}In_y$ alloys all three characteristic temperatures, $T_g$, $T_c$ and $T_m$ decrease with increase in *In* at.%. $\Delta T$ also decreases with *In* content indicating that the system becomes more prone to crystallization. The heating rate dependence of $T_g$ and

$T_c$ reveals that activation energy for glass transition and crystallization decreases with increase in *In* content.

The transmission spectra show a blue shift on *Ge* addition in $Sb_{10}Se_{90-x}Ge_x$ thin films. The refractive index decreases with increasing *Ge* at.%. Extinction coefficient decreases to minimum and optical band gap increases to maximum at $x = 25$. The values of $E_0$ and $E_d$ increase while that of static refractive index decreases with *Ge* alloying. The loss tangent shows a minimum for $x = 25$ indicating a decrease in the dielectric loss of the system. The third order susceptibility and non–linear refractive index calculated from Tichy–Ticha and Fournier Snitzer approach decreases with increase in *Ge* additive.

The transmission spectra of $Sb_{10}Se_{65}Ge_{25-y}In_y$ thin films show a red shift with *In* content. With the incorporation of *In*, refractive index and extinction coefficient increases. The values of optical band gap and $E_0$ decrease while $E_d$, static refractive index and dielectric parameters increase with *In* alloying concentration. The optical band gap values decrease due to the reappearance of *Se–Se* unsaturated bonds which increase localized states. The values of $\chi^{(3)}$ and non–linear refractive indices calculated by both approaches increase with increase in *In* content.

Chalcogenide glasses are promising candidates for photoconductive applications. So, photoconductivity studies can be carried out on ternary *SbSeGe* as well as quaternary *SbSeGeIn* glassy system. The study of effect of other additives like *Bi*, *Pb*, *Sn* etc. on ternary $Sb_{10}Se_{90-x}Ge_x$ system can also be carried out.

# References

## References

[1] Popescu M A 2000 *Non-crystalline chalcogenides* vol 8 (Springer).

[2] Schultz-Sellack C 1870 *Ann Phys.* 215 182.

[3] Wood R W 1902 *Phil Mag.* 3 607.

[4] Meier W 1910 *Annal Phys.* 336 1017.

[5] Zachariasen W H 1932 *J Am Chem Soc.* 54 3841.

[6] Frerichs R 1950 *Phys Rev.* 78 643.

[7] Goriunova N A and Kolomiets B T 1955 *Zhurnal Tekhnicheskoi Fiziki (russ.)* 25 2069.

[8] Glaze F W, Blackburn D H, Osmalov J S, Hubbard D and Black M H 1957 *J Res Nat Bur Standards* 59 83.

[9] Ioffe A F and Regel A R 1960 *Prog. Semicond.* 4 237.

[10] Hilton A R and Brau M 1963 *Infrared Phys.* 3 69.

[11] Jones C and Hafner H 1968 Final Technical Report, Contract No. AF 33 (615)-3963.

[12] Ovshinsky S R 1968 *Phys Rev Lett.* 21 1450.

[13] Harkin J M, Dong A and Chesters G 1976 *Nature* 259 204.

[14] Ciureanu P and Middelhoek S 1992 *Thin Film Resistive Sensors* (London, *IOP Publishing*).

[15] Johanson R E, Kasasp S O, Rowlands J and Polischuk B 1998 *J Non-Cryst Solids* 227-230 1359.

[16] Quiroga I, Corrector C, Bellido F, Valazquez J, Villares P and Garay R J 1996 *J. Non-Cryst. Solids* 196 183.

[17] Bicerano J and Ovshinsky S R 1985 *J Non-Cryst Solids* 74 75.

[18] Boolchand P 2001 *J Optoelectron Adv Mater.* 3 703.

[19] Tao H, Lin C, Gu S, Jing C and Zhao X 2007 *Appl Phys Lett.* 91 011904.

[20] Zhong X, Yuan J, Tao H, Liu Y, Zu C and Wuhan J 2012 *Univ. Technol. – Mater. Sci. Ed.* 27 1180.

[21] Maurugeon S, Bureau B, Pledel C B, Faber A J, Zhang X H, Geliesen W and Lucas J 2009 *J Non-Cryst Solids* 355 37.

[22] Wilhelm A A, Pledel C B, Coulombier Q, Lucas J, Bureau B and Lucas P 2007 *Adv Mater.* 19 3796.

- [23] Mott N F 1979 *Electronic Processes in Non-Crystalline Materials* (Clarendon, London).
- [24] Fritzsche H 2007 *J Phys Chem Solids* 68 878.
- [25] Hisakuni H and Tanaka K 1995 *Science* 270 974.
- [26] Sanghera J S, Shaw L B, Aggarwal I D and Chim C R 5 873.
- [27] Ramachandran S 2005 *IEEE J Sel Topics Quantum Electron* 11 260.
- [28] Quemard C, Smektala F, Couderc V, Barthelemy A and J. Lucas 2001 *J Phys Chem Glasses* 62 1435.
- [29] Harbold J M 2002 *IEEE Photon Technol Lett.* 14 822.
- [30] Sainov S, Sainov V and Dikaova J 2001 *J Optoelectron Adv Mater.* 3 399.
- [31] Taillades G, Valls O, Bratov A, Dominguez C, Pradel A and Ribes M 1999 *Sensor Actuat B-Chem.* 59 123.
- [32] Keirsse J, Pledel C B, Loreal O, Sire O, Bureau B, Turlin B, Leroter P and Lucas J 2003 *J Non-Cryst Solids* 326-327 430.
- [33] Tiwari A N 2005 *Thin Solid Film* 480-481 1.
- [34] Wong S, Deubel M, Perea-Willard F, John S, Ozin G A, Wegener M and Freymann G 2006 *Adv Mater.* 18 265.
- [35] Samson Z L, Yen S C, MacDonald K F, Knight K, Li S, Hewak D W, Tsai D P, Zheludev N I 2010 *Phys Status Solidi – RRL* 4 274.
- [36] Sanchez E A, Waldmann M and Arnold C B 2010 *Appl Opt.* 50 1974.
- [37] Desevedavy F, Renversez G, Troles J, Houizot P, Brilland L, Vasiliet I, Coulombier Q, Traynor N, Smektala F and Adam J 2010 *Opt. Mater.* 32 1532.
- [38] Faraon A, Englund D, Bulla D, Davies B L, Eggleton B J, Stoltz N, Petroff P and Vuckovic J 2008 *Appl Phys Lett.* 92 043123.
- [39] Thorpe M F and Weaire D 1971 *Phys Rev B* 4 3518.
- [40] Anderson P W 1975 *Phys Rev Lett.* 34 953.
- [41] Cohen M H, Fritzsche H and Ovshinsky S R 1969 *Phys. Rev. Lett.* 22 1065.
- [42] Cohen M H 1970 *J Non-Cryst Solids* 4 391.
- [43] Adler D 1982 *Naturwissenschaften* 69 574.
- [44] Davis E A and Mott N F 1970 *Phil Mag.* 22 903.
- [45] Marshall J M and Owen A E 1971 *Phil Mag.* 24 1281.
- [46] Emin D, Seager C H and Quinn R K 1972 Phys Rev Lett. 28 813.

[47] Street R A and Mott N F 1975 *Phys Rev Lett.* 35 1293.

[48] Mott N F, Davis E A and Street R A 1975 *Phil Mag.* 32 961.

[49] Kastner M, Adler D and Fritzsche H 1976 *Phys Rev Lett.* 37 1504.

[50] Warren B E, Kruther H and Star M 1936 *J. Am. Cer. Soc.* 19 202.

[51] Lucovsky G, Galeener F L, Keezer R C, Geils R H and Six H A 1974 *Phys. Rev. B* 10 5134.

[52] Kumar P, Sathiaraj T S and Thangaraj R 2010 *Phil Mag Lett.* 90 183.

[53] Kumar R, Sharma P, Katyal S C, Sharma P and Rangra V S 2011 *J. Appl. Phys.* 110 013505.

[54] Wang G, Nie Q, Wang X, Shen X,Chen F, Xu T, Dai S and Zhang X 2011 *J Appl. Phys.* 110 043536.

[55] Nikolic P M, Paraskevopoulos K M, Vujatovic S S, Bojicic A, Zorba T T, Nikolic M V, Stamenovic B, Ivetic T and V. Blagojevic 2008 *J. Mater. Sci.* 43 5516.

[56] Sharma P and Katyal S C 2008 *J. Non-Cryst.* Solids 354 3836.

[57] Singh A K and Singh K 2009 *J. Mod. Optic.* 56 471.

[58] Adel Gh, Ali A K, Abd-Rabo A S and Nabhan E 2009 *Chalcogenide Lett.* 6 343.

[59] Singh A K, Mehta N and Singh K 2009 *Physica B* 404 3470.

[60] Pamukchieva V, Todorova1 K, Mocioiu O C, Zaharescu M, Szekeresl A and Gartner M 2012 *J Phys:Conference Series* 356 012047.

[61] Petkov K, Vassilev G, Todorov R, Tasseva J and Vassilev V 2011 *J Non-Cryst. Solids* 357 2669.

[62] Dai S, Wang G, Nie Q, Wang X, Shen X, Xu T, Ying L, Sun J, Bai K, Zhang X and Heo J 2010 *Infrared Phys. Technol.* 53 392.

[63] Phillips J C 1979 *J Non-Cryst. Solids* 34 153.

[64] Phillips J C and Thorpe M F 1985 *Solid State Commun.* 53 699.

[65] Zhenhua L 1991 *J Non-Cryst. Solids* 127 298.

[66] Tichy L and Ticha H 1995 *J. Non-Cryst. Solids* 189 141.

[67] Singh D, Kumar S and Thangaraj R 2010 *J Optoelectron. Adv. Mater.* 12 1505.

[68] Mainika, Sharma P and Thakur N 2009 *Phil. Mag.* 89 3027.

[69] Sharma P, Rangra V S, Katyal S C and Sharma P 2007 *Optoelectron. Adv. Mater.* 1 363.

[70] Ediger M D, Angell C A and Nagel S R 1996 *J Phys. Chem.* 100 13200.

[71] Angell C A 1991 *J Non-Cryst Solids* 131-133 13.

[72] Yinnon H and Uhlmann D R 1983 *J. Non-Cryst. Solids* 54 253.

[73] Varshneya, A. K. 1994 *Fundamentals of inorganic glasses: Arun K. Varshneya*. (Academic Pr.).

[74] Swanson S E, 1977 *Am. Mineral.* 62 966.

[75] Abu-Sehly A A 2011 *Mater. Chem. Phys.* 125 672.

[76] Kotkata M F and Mansour Sh A 2011 103 957.

[77] Al-Ghamdi A A, Alvi M A and S A Khan 2011 *J Alloy Compd.* 509 2087.

[78] Abu-Sehly A A 2009 *Thermochim Acta* 485 14.

[79] Deepika, Rathore K S and Saxena N S 2009 *J Phys: Condens Matter* 21 335102.

[80] Fayek S A, Fouad S S, Balboul M R and El-Bana M S 2007 *Physica B* 388 230-236.

[81] Deepika, Jain P K, Rathore K S and Saxena N S 2009 *J Non-Cryst Solids* 355 1274.

[82] Singh A K and Singh K 2009 *Phil. Mag.* 89 1457.

[83] Prashanth S B B and Asokan S 2009 *J Non-Cryst Solids* 355 164.

[84] Dahshan A, Aly K A and Dessouky M T *Phil. Mag.* 88 2399.

[85] Shaaban E R, Kansal I and Shapaan M and Ferreira Jose´ M F 2009 *J Therm. Anal.* 98 347.

[86] Aly K A, Othman A A and Abousehly A M 2009 *J Alloys Compd.* 467 417.

[87] Kumar S, Singh K and Mehta N 2010 *Phil. Mag. Lett.* 90 547.

[88] J. Tauc 1970 *The Optical Properties of Solids* (North-Holland: Amsterdam).

[89] Hughes M, Rutt H and Hewak D 2007 *Appl Phys Lett.* 90 031108.

[90] Klocek P, Roth M and Rock R D 1987 *Opt Eng.* 26 88.

[91] Kotkata M F, Abdel-Wahab F A and Al-Kotb M S 2009 *Appl. Surf. Sci.* 255 9071.

[92] Ammar A H, Abde-Moneim N M, Farag A A M and El-Sayed M F 2012 *Physica B* 407 356.

[93] Aly K A 2010 *Appl. Phys.* A 99 913.

[94] Sharma A and Barman P B 2009 *Appl. Phys. B* 97 835.

[95] El-Gendy Y A 2009 *J Phys D: Appl Phys.* 42 115408.

[96] Sharma P and Katyal S C 2007 *Thin Solid Films* 515 7966.

[97] Fouad S S, El-Shazly E A A, Balboul M R, Fayek S A, M.S. El-Bana 2006 *J Mater.Sci: Mater Electron.* 17 193.

[98] Al-Ghamdi A A 2006 *Vacuum* 80 400.

[99] Kumar K, Purohit L P, Kumar R and Mehra R M 2009 *J. Phys. D: Appl. Phys.* 42 115108.

[100] Dahshan A, Ammer H H and Aly K A 2008 *J Phys. D: Appl.Phys.* 41 215401.

[101] Marquez E, Gonzalez-Leal J M, Bernal-Oliva A M, Jimenez-Garay R and Wagner T 2008 *J Non-Cryst. Solids* 354 503.

[102] Todorov R, Tsankov D, Pirov J and Petkov K 2011 *J. Phys. D: Appl. Phys.* 44 305401.

[103] http://en.wikipedia.org/wiki/Phase-change_memory#cite_note-32

[104] Sevik C and Cagin T 2011 *J. Appl. Phys.* 109 123712.

[105] Kolobov A V and Tominaga J, *Chalcogenides*, Springer Series in Materials Science 164.

[106] Zhang H, Liu C X, Qi X L, Dai X, Fang Z and Zhang S C 2009 *Nature Phys.* 5 438.

[107] Wang G, Zhu X, Wen J, Chen X, He K, Wang L, Ma X, Liu Y, Dai X, Fang Z, Jia J and Xue Q 2010 *Nano Res.* 3 874.

[108] Hsieh D, Xia Y, Qian D, Wray L, Meier F, Dil J H, Osterwalder J, Patthey L, Fedorov A V, Lin H, Bansil A, Grauer D, Hor Y S, Cava R J and Hasan M Z 2009 *Phys. Rev. Lett.* 103 146401.

[109] Moore J 2009 *Nature Phys.* 5 378.

[110] Tao C S, Jiang J and Tao M 2011 *Sol Energ Mat Sol C* 95 3176.

[111] Goetzberger A, Hebling C and Schock H W 2003 *Mat. Sci Eng. R* 40 146.

[112] Siebentritt S and S. Schorr 2012 *Prog. Photovolt. Res. Appl.* DOI: 10.1002/pip.2156.

[113] Hsu F C, Luo J Y, The K W, Chen T K, Huang T W, Wu P M, Lee Y C, Huang Y L, Chu Y Y, Yan D C and Wu M K 2008 *Proc. Natl Acad. Sci. USA* 105 14262.

[114] Si W, Zhou J, Jie Q, Dimitrov I, Solovyov V, Johnson P D, Jaroszynski J, Matias V, Sheehan C and Li Q 2011 *Appl. Phys. Lett.*98 262509.

[115] Zheludev N I 2011 *Optics and Photonics News* 22 30.

[116] Samson Z L, MacDonald K F, Angelis F D, Gholipour B, Knight K, Huang C C, Fabrizio E D, Hewak D W and Zheludev N I 2010 *Appl. Phys. Lett.* 96 143105.

[117] Chiang Y S, Ing Jr. S W, 1969 13 883.

[118] Tanaka K 1989 *Phys Rev B* 39 1270.

[119] Kasap S, Frey J B, Belev G, Tousignant O, Mani H, Laperriere L, Reznik A and Rowlands J A 2009 *Phys Status Solidi* 246 1794.

[120] Belev G and Kasap S O 2004 *J Non-Cryst Solids* 345-346 484.

[121] Chen Z, Dong M, Li C, Shao S, Hu T and Kang D 2013 *Phys Status Solidi A* 210 580.

[122] El-Korashy A, El Zahed H, Zayed H A and Kenawy M A 1995 *Solid Stat Commun.* 95 335.

[123] Aly K A, Dahshan A and Abousehly A M 2008 *Phil. Mag.* 88 47.

[124] Holubova J, Cernosek Z and Cernoskova E 2007 *J Optoelectron. Adv. Mater.* 9 1979.

[125] K. Petkov, R. Todorov, J. Tasseva and D. Tsankov 2009 J Optoelectron. Adv. Mater. 11 2093.

[126] Goel S, Tripathi S K and Kumar A 1990 *Revue Phys. Appl.* 25 333.

[127] Kumar A, Goel S and Tripathi S K 1988 *Phys. Rev. B* 38 432.

[128] Sharma P, Sharma I and Katyal S C 2009 *J Appl. Phys.* 105 053509.

[129] Kushwaha N, Singh S, Shukla R K and Kumar A 2008 *J Alloys Compd.* 456 46.

[130] Kang M J, Park T J, Wamwangi D, Wang K, Steimer C, Choi S Ya and Wuttig M 2007 *Microsyst Technol* 13 153.

[131] Yoon S M, Lee N Y, Ryu S O, Choi K J, Park Y S, Lee S Y, Yu B G, Kang M J, Choi S Y and Wuttig M 2006 *IEEE Electron Device Lett.* 27 445.

[132] Shaaban E R, Abdel-Rahman M, Yousef E S and Dessouky M T 2007 *Thin Solid Films* 515 3810.

[133] Kostadinova O and Yannopoulos S N 2009 *J Non-Cryst. Solids* 355 2040.

[134] Holubova J, Cernosek Z and Cernoskova E 2009 *J Non-Cryst. Solids* 355 2050.

[135] Mehta N, Tiwari R S and Kumar A 2006 *Mater. Res. Bull.* 41 1664.

[136] Saleh S A, Al-Hajry A and Ali H M 2011 *Phys. Scr.* 84 015604.

[137] Bindra K S, Suri N, Kumar P and Thangaraj R 2007 *Solid Stat Commun.* 144 83.

[138] Sakrani S, Adam A B and Wahab Y 2002 *Solid Stat Sci. Technol.* 10 60.

[139] Haisty R W and Krebs H 1969 *J Non-Cryst. Solids* 128 399.

[140] Kumar K, Purohit L P, Kumar R and Mehra R M 2009 *J. Phys. D: Appl. Phys.* 42 115108.

[141] Dahshan A, Amer H H and Aly K A 2008 *J. Phys. D: Appl. Phys.* 41 215401.

[142] Mainika, Sharma P, Katyal S C and Thakur N 2008 *J. Phys. D: Appl. Phys.* 41 235301.

[143] Wakkad M M 2001 *J Therm. Anal. Calorim.* 63 533.

[144] Adam A B, Sakrani S and Wahab Y 2005 *J Mater. Sci.* 40 1571.

[145] Ma H L, Guimond Y, Zhang X H and Lucas J 1999 *J Non-Cryst. Solids* 256-257 165.

[146] Vassilev V, Tomova K, Parvanova V and Parvanov S 2007 *Mater. Chem. Phys.* 103 312.

[147] Mehra A M, Ganjoo A and Thakur P C 1994 *J Appl. Phys.* 75 7334.

[148] Sharma V, Thakur A, Goyal N, Saini G S S and Tripathi S K 2005 *Semicond. Sci. Technol.*20 103.

[149] Maan A S and Goyal D R 2007 *J Ovonic Res.* 3 45.

[150] Al-Ghamdi A A, Khan S A, Al-Heniti S, Al-Agel F A and Zulfequar M 2011 *Curr. Appl. Phys.* 11 315.

[151] Petrov V, Yelliseyev A, Isaenko L, Lobanov S, Titov A and Zondy J –J 2004 *Appl. Phys. B* 78 543.

[152] Kissinger H E 1956 *J Res Bur Stand.* 57 217.

[153] Kissinger H E 1957 *Anal Chem.* 29 1702.

[154] Colemenero J and Barandiaran J M 1978 *J Non-Cryst Solids* 30 263.

[155] Kasap SO and Yannacopoulos S 1990 *Phys Chem Glasses* 31 71.

[156] Moynihan C T, Easteal A J, Wilder J and Tucker J 1974 *J Phys Chem* 78 2673.

[157] Mahadevan S, Giridhar A and Singh A K 1986 *J Non-Cryst Solids* 88 11.

[158] Augis J A and Benett J E 1978 *J Thermal Anal.* 13 283.

[159] Abkowitz M, Foley G M T, Markovics J M and Palumbo A C 1984 *Optical Effects in amorphous Semiconductors* (*AIP Conf. Proc.* vol 120) ed. Taylor P C and Bishop S G (New York: American Institute for Physics) pp 117.

[160] Marquez E, Ramirez-Malo J, Villares P, Jimenez-Garay R, Ewen P J S and Owen A E 1992 *J Phys D: Appl Phys.* 25 535.

[161] Swanepoel R 1983 *J. Phys. E: Sci. Instrum.*16 1214.

[162] Wemple S H and DiDomenico M 1971 *Phys. Rev. B* 3 1338.

[163] Pankove J I *Optical Processes in Semiconductors* (Dover Publications Inc.: New York) pp. 91.

[164] Ta'eed V, Baker N J, Fu L, Finsterbisch F, Lamont M R E, Moss D J, Nguyen H C,. Eggleton B J, Choi D Y, Madden S and Davis B L 2007 *Opt. Express* 15 9205.

[165] Yang Z, Fah M K, Reynolds K A, Sexton J D, Riley M R, Anne M L, Bureau B and Lucas P 2010 *Opt. Express* 18 26754.

[166] Beneventi G B, Calderoni A, Fantini P, Larcher L and Pavan P (2009) *J. Appl. Phys.* 106 054506.

[167] Coulombier Q, Brilland L, Houizot P, Chartier T, N'Guyen T N, Smektala F, Renversez G, Monteville A, Mechin D, Pain T, Orain H, Sangleboeuf J C and Troles, 2010 *Opt. Express* 18 9107.

[168] Flore C, Sanghera J S, Shaw L B, Nguyen V Q and Aggarwal I D, 2007 *Mater. Lett.* 61 1271.

[169] Ho N, Phillips M C, Qiao H, Allen P J, Krishnaswami K, Riley B J, Myers T L and Anheier N C 2006 *Opt. Lett.* 31 1860.

[170] Prakash S, Asokan S and Ghare D B 1994 *Semicond. Sci. Technol.* 9 1484.

[171] Lucovsky G, Galeener F L, Keezer R C, Geils R H and Six H A 1974 *Phys. Rev. B* 10 5134.

[172] Kumar A, Malhotra L K and Chopra K L 1989 *J. Appl. Phys.* 65 1671.

[173] Ambika and Barman P B 2007 *J Ovonic Res.* 3 21.

[174] George A, Sushamma D and Predeep P 2006 *Chalcogenide Lett.* 3 33.

[175] El-Sayed S M 2003 *Semicond. Sci. Technol.* 18 337.

[176] Boolchand P and Thorpe M F 1994 *Phys. Rev. B.* 50 10366.

[177] Boolchand P, Georgiev D G and Goodmana B 2001 *J. Optelecron. Adv. Mater.* 3 703.

[178] Sharma A and Barman P B 2009 *J. Therm. Anal Calorim.* 96 413.

[179] Tichy L, Ticha H 1994 *Mater. Lett.* 21 313.

[180] Vlcek M and Frumar M 1987 *J. Non-Cryst. Solids* 97-98 1223.

[181] Skordeva E R and Arsova D D 1995 *J. Non-Cryst. Solids* 192-193, 665.

[182] Giridhar A, Narasimham P S L and Mahadevan S 1980 *J. Non-Crystalline Solids* 37 165.

[183] Bicerano J and Ovshinsky S R 1985 *J. Non-Cryst. Solids* 75 169.

[184] Pauling L, 1976 *The Chemical Bonds* (New York: Cornell University).

[185] Sadagopan V and Gatos H C 1965 *Solid State Electron.* 8 529.

[186] Yamaguchi M 1985 *Phil. Mag. B* 51 651.

[187] Sanderson R T 1971 *Inorganic Chemistry* (New Delhi: East-West Press PUT).

[188] Rao C N R, George M V, Mahanty J and Narasimhan P T 1970 *Handbook of Chemistry and Physics* (New Delhi: East–West Press).

[189] Fouad S S, Fayek S A and Ali M H 1998 *Vacuum* 49 25.

[190] Kerner R and Micoulaut M 1997 *J. Mol. Liq.* 71 175.

[191] Pamukchieva V, Szekeres A, Todorova K, Fabian M, Svab E, Revay Z and Szentmiklosi L 2009 *J. Non-Cryst. Solids* 355 2485.

[192] Sharma P, Rangra V S, Sharma P and Katyal S C 2009 *J. Alloy Compd.* 480 934.

[193] Pauling L, Ticha H, Pacesova A and Petzlt J 1991 *J. Non-Cryst. Solids* 128 191.

[194] Somayajulu G R, 1958 *J. Chem. Phys.* 28 814.

[195] Ball G J and Chamberlain J M 1978 *J. Non-Cryst. Solids* 29 239.

[196] Ohsaka T 1976 *J. Non-Cryst. Solids* 22 359.

[197] Kato M, Onari S and Arai T 1983 *Jap. J. Appl. Phys.* 22 1382.

[198] Rechtin M D, Hilton A R and Hayes D J 1975 *J. Electron. Mater.* 4 347.

[199] Sharma A K, Bhatia K L, Bhatnagar V K, Malik S K and Kratschmer W 1989 *J. Non-Cryst. Solids* 108 309.

[200] Corredor C, Quiroga I, Vazquez J, Galdon J, Villares P and Garay R J 2000 Mater. Lett. 42 229.

[201] Quiroga I, Corredor C, Bellido F, Vazquez J, Villares P and Garay R J 1996 *J. Non-Cryst. Solids* 196 183.

[202] Goyal D R and Maan A S 1995 *J. Non-Cryst. Soilds* 183 182.

[203] Izvekov V P, Koos M and Somogyi I K 1983 *J. Non-Cryst. Solids* 59-60 1011.

[204] Fukunga T, Tanaka Y and Murase K 1982 *Solid State Commun.* 42 513.

[205] Weszka J, Daniel Ph., Burian A, Burian A M and Nguyen A T 2000 *J. Non-Cryst. Solids* 265 98-104.

[206] Wakkad M M, Shokr E K, Abd El Ghani H A and Awad M A 2007 *J Phys D: Appl Phys.* 40 7572.

[207] Imran M M A, Bhandari D and Saxena N S 2001 *J Therm. Anal. Calorim.* 65 257.

[208] Zhimei S, Zhou J, Blomqvist A, Johansson B and Ahuja R 2008 *Appl Phys. Lett.* 93 061913.

[209] Chatterjee R, Asokan S, Titus S S K 1994 *J Phy D: Appl Phys.* 27 2624.

[210] Abu El–Oyoun M 2000 *J Phys D: Appl. Phys.* 33 2211.

[211] Soltan A S 2001 *Physica B* 307 78.

[212] Kaur G, Komatsu G and Thangaraj R J 2000 *Mater. Sci.* 35 903.

[213] Turnbull D 1969 *Contemp Phys.* 10 473.

[214] Abd Elnaeim A M, Aly K A, Afify N and Abousehly A M 2010 *J Alloy Compd.* 491 85.

[215] El-Kabany N, Chalcog. Lett. 7 (2010) 351.

[216] Savage J A 1985 *Infrared optical Materials and Their Antireflection Coatings* (Adam Hilger: Bristol).

[217] Houizot P, Boussard-Pledel C, Faber A J, Cheng L K, Bureau B, Van Nijnatten P A, Gielesen W L M, do Carmo J P and Lucas J 2007 *Opt. Express* 15 12529.

[218] Rojas J L, Dominguez M, Villares P and Jimenez-Garay R 1996 *Mater. Chem. Phys.* 45 75.

[219] Pelusi M D, Ta'eed V G, Fu L, Magi E, Lamont M R E, Madden S, Choi D Y, Bulla D A P, Davies B L and Eggleton B J 2008 *IEEE J. Quatum Electron* 14 529.

[220] Duffy J A 2001 *Phys. Chem. Glasses* 42 151.

[221] Gonzalez-Leal J M, Prieto-Alcon R, Angel J A, Marquez E 2003 *J. Non Cryst. Solids* 315 134.

[222] Tanaka K 1980 *Thin Solid Films* 66 271.

[223] Majeed Khan M A, Kumar S, Husain M and Zulfequar M 2009 *J. Non-Oxide Glasses* 1 71.

[224] Ticha H and Tichy L 2002 *J. Opt. Adv. Mater.* 4 381.

[225] Fournier J and Snitzer E 1974 *IEEE J. Quantum Electron.* 10 473.

[226] Marquez E, Wagner T, Gonzalez – Leal J M, Bernal-Oliva A M, Prieto-Alcon R, Jimenez-Garay R and Ewen P J S 2000 *J. Non-Cryst. Solids* 274 62.

[227] Moss T S 1985 *Phys. Stat. Sol. (b)* 131 415.